Multi-Wavelength Studies Of Novae

Thesis submitted
for the degree of

DOCTOR OF PHILOSOPHY (SCIENCE)
in PHYSICS (EXPERIMENTAL)

by

ANINDITA MONDAL

Department of Physics
University of Calcutta

Kolkata 700001, West Bengal, India

2019

Multi-Wavelength Studies Of Novae

by

ANINDITA MONDAL

This thesis is submitted in partial fulfillment of the requirements for the award of the degree of Doctor of Philosophy (Science) in Physics (Experimental) of University of Calcutta

Department of Physics
University of Calcutta

Kolkata 700001, West Bengal, India

2019

To

My parents

Mrs. Parbati Mondal & Mr. Anandamoy Mondal

dear brother

Arindam

and

my beloved husband

Tanmoy

"Imagination is more important than knowledge. For knowledge is limited, whereas imagination embraces the entire world, stimulating progress, giving birth to evolution."

— Albert Einstein

Contents

List of Figures iv

List of Tables viii

Abstract xi

Dissemination xv

Acknowledgment xvii

1 Novae: A Brief Introduction 1

1.1 Nova and its Physical Structure 1

1.1.1 Outburst Mechanism 2

1.1.2 Post-outburst Phases 4

1.2 Classification of Novae 6

1.3 Properties of Novae 7

1.3.1 Light Curves: Characteristic Times & Speed Classes 7

1.3.2 Light Curves: Evolution 8

1.3.3 Evolution of Spectra 10

1.3.4 Modern Spectral Classification 14

1.3.5 Maximum Magnitude Vs. Rate of Decline (MMRD) Relation . . . 16

1.4 Physical Parameters of Novae 17

1.4.1 Bolometric Luminosity 18

1.4.2 Mass and orbital period . . . 19
1.4.3 Expansion Velocity and Geometry of the ejecta . . . 19
1.4.4 Mass of the ejected gas . . . 20
1.4.5 Ejecta abundances . . . 21
1.5 Multiwavelength Aspects of Novae . . . 22
1.6 Importance of Novae in Astronomical Context . . . 25
1.7 Motivation for Present Work . . . 26

2 Methodology **29**
2.1 Dataset . . . 29
2.1.1 Observational Data . . . 29
2.1.2 Data reduction . . . 32
2.1.3 Observations of optical spectra of RS Oph (2006 outburst) . . . 37
2.1.4 Published Data . . . 41
2.2 Photoionization model . . . 41

3 Study of the Recurrent Nova RS Ophiuchi **47**
3.1 Observational data . . . 51
3.1.1 Evolution of the spectrum . . . 52
3.1.2 Description of some emission lines . . . 58
3.2 Published Optical and NIR data . . . 72
3.3 Modelling Procedure . . . 74
3.4 Results . . . 77
3.4.1 Early Phase: 2006 February – May . . . 77
3.4.2 Calculation of Ejected Mass . . . 86
3.5 Discussion . . . 88
3.6 Summary . . . 95

4 Photoionization model grid of novae: estimation of physical parameters **97**

4.1 Introduction . . . 97

4.2 Novae Grid Calculation . . . 100

4.3 Results . . . 108

4.4 Summary & Discussions . . . 122

5 Study of Quiescence Phase Spectra of Novae **127**

5.1 Introduction . . . 127

5.2 Dataset . . . 128

5.3 Results . . . 131

5.3.1 Description of Observed data . . . 131

5.3.2 Modelling of spectra . . . 140

5.4 Summary & Discussions . . . 152

6 Summary and Scope for Future Work **155**

Bibliography **159**

List of Figures

1.1 Schematic diagram of nova 2

1.2 Bi-CNO cycle 4

1.3 Typical light curve of novae 9

1.4 The evolutionary sequence of nova V1494 Aql 12

1.5 MMRD relationship for novae 18

2.1 HCT observatory and the telescope 31

2.2 HFOSC and TIRSPEC instruments 33

3.1 Optical spectra of RS Oph during 2006 February-1 51

3.2 Optical spectra of RS Oph during 2006 February-2 52

3.3 The Hα line in RS Oph spectra 53

3.4 Optical spectra of RS Oph during 2006 March 55

3.5 Optical spectra of RS Oph during 2006 April – June 56

3.6 Spectra of RS Oph during 2006 July – October 58

3.7 Velocities in the RS Oph spectra 59

3.8 Evolution of the O I 7774 Å line 60

3.9 Evolution of the O I 8446 Å line 61

3.10 Evolution of the [O III] 4363 Å line 62

3.11 Evolution of the [O III] 4959 and 5007 Å lines 63

3.12 Evolution of the He I 7065 Å line 64

3.13 Evolution of the He II 4686 Å line 65

3.14 Evolution of the [N II] 5680 and 5755 Å lines 67
3.15 Evolution of the [Fe XIV] 5303 Å line 68
3.16 Evolution of the [Fe X] 6374 Å line 69
3.17 Evolution of the Raman scattered 6830 Å line 70
3.18 Best-fit CLOUDY model spectra plotted over the observed optical and NIR JHK spectra of RS Oph observed on epochs D31 and D49 76
3.19 Best-fit CLOUDY model spectrum plotted over the observed spectrum of RS Oph observed on 2006 February 21 78
3.20 Best-fit CLOUDY model spectrum plotted over the observed spectrum of RS Oph observed on 2006 February 24 79
3.21 Best-fit CLOUDY model spectrum plotted over the observed spectrum of RS Oph observed on 2006 March 12 79
3.22 Best-fit CLOUDY model spectrum plotted over the observed spectrum of RS Oph observed on 2006 April 3 80
3.23 Best-fit CLOUDY model spectrum plotted over the observed spectrum of RS Oph observed on 2006 May 26 80
3.24 Best-fit CLOUDY model spectrum plotted over the observed spectrum of RS Oph observed on 2006 July 19 82
3.25 Best-fit CLOUDY model spectrum plotted over the observed spectrum of RS Oph observed on 2006 August 18 85
3.26 Best-fit CLOUDY model spectrum plotted over the observed spectrum of RS Oph observed on 2006 October 17 85

4.1 Schematic diagram of the structure of datasets of novae grid models . . . 104
4.2 Contour plot of Hα line flux ratio w.r.t. Hβ 109
4.3 Plots of different extracted contour lines for nova RS Oph 112
4.4 Comparison of observed and CLOUDY generated spectra of nova RS Oph 113
4.5 Plots of different extracted contour lines of nova KT Eri 115

4.6 Plots of different extracted contour lines of nova V5558 Sgr 116
4.7 Plots of different extracted contour lines of nova U Sco 118
4.8 Plots of different extracted contour lines of nova V339 Del 119
4.9 Plots of different extracted contour lines of nova 2015 of dwarf galaxy IC1613 120
4.10 Plot of different extracted contour lines of nova V5558 Sgr incorporating 5% error 124

5.1 Quiscence phase spectrum of nova T CrB, observed on March 17, 2016 . 132
5.2 Quiscence phase spectrum of nova GK Per, observed on January 31, 2016 133
5.3 Quiscence phase spectra of nova RS Oph, observed on April 26, 2007 and January 31, 2016 135
5.4 Quiscence phase spectrum of symbiotic nova BX Mon observed on May 13, 2016 136
5.5 Best-fit CLOUDY modelled spectrum matched with the quiscence phase spectrum of T CrB 142
5.6 Best-fit CLOUDY modelled spectrum matched with the quiscence phase spectrum of GK Per 143
5.7 Best-fit CLOUDY modelled spectra matched with the quiscence phase spectra of RS Oph 146
5.8 Best-fit CLOUDY modelled spectrum matched with the quiscence phase spectrum of BX Mon 147
5.9 Best-fit CLOUDY modelled spectrum matched with the quiscence phase spectrum of V3890 Sgr 148
5.10 Best-fit CLOUDY modelled spectrum matched with the quiscence phase spectrum of V745 Sco 150

List of Tables

1.1 Speed class of novae. 8

1.2 Typical values of MMRD constants. 17

1.3 Deduction from optical observations of novae. 21

2.1 Specifications of HCT instruments. 34

2.2 Observational Log of HCT. 38

2.3 Journal of observations of RS Oph during 2006 outbursts. 39

2.4 A log of the published spectroscopic data used for the study. 40

3.1 Log of observations of RS Oph during 2006 outburst. 50

3.2 A log of the published spectroscopic data of RS Oph (2006) taken for study. 73

3.3 Best-fit CLOUDY model parameters of RS Oph (using published data). . 83

3.4 Best-fit CLOUDY model parameters of RS Oph during early phase (2006). 84

3.5 Best-fit CLOUDY model parameters of RS Oph during nebular phase (2006). 87

3.6 Observed and best-fit CLOUDY model line fluxes (using published data). 89

3.7 Observed and best-fit CLOUDY model line fluxes during early phase. . . 92

3.8 Observed and best-fit CLOUDY model line fluxes during nebular phase. . 94

4.1 List of the parameters and range of their values considered for the grid model. 102

4.2 Normalized fluxes of hydrogen and helium emission lines w.r.t. Hβ 105

4.3 Comparison of estimated parameter values of few novae obtained from grid model with previously calculated results. 110
4.4 Estimated parameter values of few novae obtained from CLOUDY grid model. 121

5.1 Log of HCT observations. 129
5.2 Brief description of the objects for quiescence study. 130
5.3 Observed and best-fit CLOUDY model line fluxes. 138
5.4 Observed and best-fit CLOUDY model line fluxes. 139
5.5 Best-fit CLOUDY model parameters. 151

Abstract

In the last few decades, significant progress has been made in understanding novae outburst due to improved techniques in observational as well as in theoretical sciences. In spite of that, there are still many unsolved problems that make our understanding of the nova theory incomplete. In this dissertation, I have tried to understand few observational properties of novae outburst. The primary goal is to understand novae spectra and using photoionization models to study the physical properties and other characteristics of the system. The contents of the thesis have been divided into six chapters as follows.

Chapter 1: Novae: A Brief Introduction

Chapter 1 contains a general introductory review of novae and the outline of the dissertation. General properties and characteristics, classifications, physical processes responsible for the nova outburst are explained. The astronomical significance and relevance of multiwavelength studies are discussed and the aims and scope of the thesis are indicated.

Chapter 2: Methodology

Chapter 2 describes the observation techniques and instruments that were used for the observations presented in the thesis. This is followed by discussions on data reduction procedure and analysis techniques. Details of the photoionization code CLOUDY and modelling of spectra varying the input parameters as well as estimation of the parameter values through best-fit models are discussed.

Chapter 3: Study of the Recurrent Nova RS Ophiuchi

Chapter 3 deals with the observation and modelling of multiwave-length spectroscopic data of recurrent nova RS Ophiuchi during its 2006 outburst. The optical data were taken in 2m HCT, IIA and NIR data were taken in 1.2m Mt. Abu Telescope, PRL, as well as archival data are also used. These data are then analysed and modelled using CLOUDY code to estimate the physical properties and elemental abundances of RS Oph.

Chapter 4: Photoionization model grid of novae: estimation of physical parameters

In this chapter, a grid model for novae using photoionization code CLOUDY is described. The models are generated by varying various parameter values for each grid point. The results are then matched with previous observations for validation. Using this grid method, physical parameters of other galactic and extra-galactic novae are also estimated.

Chapter 5: Study of Quiescence Phase Spectra of Novae

In Chapter 5, observation and modelling of quiescence phase spectra of various novae have been described in details. The observational data are taken at 2m HCT, IIA and then reduced and modelled. Results reveal the physical structure and type of secondary of the systems. Estimated values of physical parameters and elemental abundances are also determined from the best-fit model spectra.

Chapter 6: Summary and Scope for Future Work

Finally, all the results of the above mentioned works are summarized in Chapter 6 followed by a discussion on the future possibilities of further observations and research works on the astrophysical object novae.

The tables, figures and equations are numbered sequentially in each section, with the chapter and section numbers indicated by suffixes.

Some of the results presented in the above chapters have been published in peer-reviewed journals and rest has been communicated and expected to be published soon. They have been mentioned in the dissemination section. A list of references used in this thesis is presented at the end.

Dissemination

The work described in this thesis was undertaken while the author was a research student under the supervision of Dr. Ramkrishna Das and Dr. Soumen Mondal in the Department of Astrophysics & Cosmology, S. N. Bose National Centre for Basic Sciences (SNBNCBS), affiliated to University of Calcutta.

Portions of this work have appeared in the following papers:

1. **Mondal A.**, Das R. K., Shaw G., and Mondal S., *Photoionization model grid of novae: estimation of physical parameters*, Monthly Notices of the Royal Astronomical Society (2019), 483, 4884.
   DOI: 10.1093/mnras/sty3361

2. **Mondal A.**, Anupama G. C., Kamath U. S., Das R. K., Selvakumar G., and Mondal S., *Optical Spectroscopy of the recurrent nova RS Ophiuchi - from the outburst of 2006 to quiescence*, Monthly Notices of the Royal Astronomical Society (2018), 474, 4211.
   DOI: 10.1093/mnras/stx2988

3. Das R. K. and **Mondal A.**, *Abundance analysis of the recurrent nova RS Ophiuchi (2006 outburst)*, New Astronomy (2015), 39, 19.
   DOI: 10.1016/j.newast.2015.02.004

Besides, the following paper based on this work has been communicated:

1. **Mondal A.**, Das R. K., Anupama G. C., and Mondal S., *Photoionization modelling of quiescence phase spectra of novae & symbiotic stars.*

Apart from the research works, the author was involved in the following discovery:

1. Mondal S., Das R. K., Ashok N. M., Banerjee D. P. K., Dutta S., Ghosh S., **Mondal A.**, and Nandi A., *Near Infrared photometric and spectroscopic observations of the bright optical transient J212444.87+321738.3*, The Astronomer's Telegram (2013) # 4931.

All the figures presented in this thesis have been produced by the author using xmgrace and sigmaplot software.

The manuscript of this thesis has been checked several times with extreme care to free it from all discrepancies and typos. Even then the vigilant readers may find mistakes and several portions of this thesis may seem unwarranted, mistaken, and/or incorrect. The author takes the sole responsibility for these unwanted errors which have resulted from her inadequate knowledge in the subject or incomplete digestion of the relevant concepts or escaped her notice.

Acknowledgment

Joining S N Bose National Cantre for Basic Sciences, Kolkata, for the Ph.D. programme has been a truly life-changing experience for me and this thesis is the outcome of the six years of research that has been carried out here. This would not have been even possible without the support and guidance received from the people around me.

I would begin by offering my heartfelt thanks and warmest regards to my supervisor Dr. Ramkrishna Das without whose guidance, support, patience and encouragement this Ph.D. thesis would not have been possible. He introduced me to the astonishing universe of the observational astronomy, its amazing history and encouraged me to explore all the opportunities. I have enjoyed my time here and never felt overburdened by the work pressure as he has always been very helpful discussing the slightest bit of confusion concerning the research work. Being his first research student has been a privilege which enabled spending times sharing not only scientific knowledge but also having long discussions regarding literature, politics and social problems that helped me shape my mind to become the person I am today. I am extremely lucky to have a supervisor who cared so much about my professional life as well as my personal well-being. I could not have been imagined of having a better mentor. I express my deepest gratitude to my joint-supervisor Dr. Soumen Mondal for all the knowledge that I have gained from him during the course of this work. I have learnt a lot from his guidance and his advice and suggestions helped me to improve the quality of my research. It has been an honour for me to work under his supervision.

I would like to thank the Department of Science & Technology (DST Fellowship Scheme), Govt. of India, for the financial support during my research period, and all academic and non-academic staffs of the S N Bose National Centre for Basic Sciences (SNBNCBS), for their sincere help during the work. The residential campus of the centre provided me with a friendly environment to carry on with my research peacefully. I also express profound gratitude to all the faculties and members of the Department of Astrophysics and Cosmology for the several fruitful discussions we had during this period. I would also like to express my heartfelt gratitude to Prof. Sandip Kumar Chakrabarti and Prof. Biswajit Chakraborty for several useful comments, suggestions as members of my thesis committee. I thank them for the insightful discussions, encouragement as well as the critical questions that incented me to widen my research from various perspective.

I would also take this opportunity to express my gratitude to my collaborators Prof. G. C. Anupama of Indian Institute of Astrophysics (IIA), Bangalore, and Dr. Gargi Shaw of Tata Institute of Fundamental Research (TIFR), Mumbai, for the opportunities they provided to work with them and learn from their knowledge and research expertise. I acknowledge HTAC (HCT Time Allocation Committee) members for allocation of the observing nights at 2m Himalayan Chandra Telescope (HCT) and I express my heartfelt thanks to the observatory technicians of Centre For Research & Education in Science & Technology (CREST), IIA, - Pramod, Gauri, Kiran, Laxmi, & Prabhu for their sincere support and help during the observations. The long nights of capturing observational data would have been difficult to go through without your humour and banter alongside the sincere work.

My fellow colleagues Alik, Dhrimadri, Rahul, Ruchi, Samrat and Somnath have been very supportive throughout my research time and I am really thankful to

them for the numerous personal and scholarly interactions we had and their valuable suggestions in countless occasions. I want to make a special mention of Samrat for not only being a wonderful junior, but also a friend in need. Thank you for providing me with moral support and helping me out in many different situations. I would also like to thank all my SNB friends (there are so many and you know who you are) for their continuous encouragement, help, support, and all the fun we had during my stay at the centre.

I also take this opportunity to convey my heartiest thanks to my most beloved and most precious friends Arpita, Debalaya, Diya, Durba, Payel, Sumana, Wahida and Subhajit for their love and well wishes. I would like to thank *Sensei* Partha Da, Supriya, Tiyash and all other members of JUKC (Jadavpur University Karate Club) and 360^0 Sports for imparting sportsman spirit into me and for keeping me physically and mentally fit. Thank you Kingshuk for introducing me to the adventure sports and the joy of trekking which has helped me to push my physical and mental limits. All of you have gifted me the happiest and the most memorable years of my life during my under-graduate and post-graduate days at Jadavpur University and beyond. I consider myself extremely fortunate for having such valuable friends.

It is a great honour for me to express my indebtedness to my high school science tutors Mr. Gautam Basu, Mr. Ashok Ghosh, Mr. Kalyan Chakrobarty and Mr. Debashish Moulick for their tremendous encouragement during my days in school which inspired me to pursue knowledge in the world of science. It is to their immense credit that they did such a great job the whole time they were there. Thanks to all the teachers of Indian Girls' High School (IGHS) and Railway Mixed Primary (RMP) School, Kanchrapara, where I spent the most exciting fourteen years of my life. And I thank all my childhood friends for making my life all the more enjoyable.

I must also thank my *didi* (sister) Arunima, *jamaibabu* (brother-in-law) Swapan Da

and nephew Rupan for their unconditional love, encouragement, well wishes, and deep concern for my well-being. I am grateful to my *didi* for her expert culinary skills for the delicious meals I had over the time during my stay at Kolkata. Above all, I express my deepest gratitude and indebtedness to my parents, my brother, my beloved husband and my in-laws for their sacrifices, well wishes, encouragement, mental support, and utmost love and care. Whatever little I have been able to achieve in my life is because of them. No word is enough to express my gratitude to my *maa-baba* for believing in me and keeping faith in me. I love you so much. Also, my dream of completing Ph.D. would not have been possible without their patience and support during the challenging phases of my academic career. And Tanmoy, my best friend, my love, my partner-in-crime, without you it was not even possible to make this far. Thank you for understanding me, being there for me no matter what, overcoming all the troughs and crests together, for all the support and love and care. You are the only person who can appreciate my quirkiness and sense of humour. There are no words to convey how much I love you.

Last, but not the least, I would like to thank everyone who has been an important part of my life and wishes for my success and well-being. I sincerely apologize to them as I could not mention them individually.

Anindita Mondal

Department of Astrophysics & Cosmology,

S. N. Bose National Centre for Basic Sciences.

Chapter 1

Novae: A Brief Introduction

Throughout my research period, I have studied the incredible object called novae. I tried to understand the system, its physical nature and characteristics, its behaviour and the evolution of novae spectra through its various phases. In this chapter, I would try to describe this astonishing astrophysical object as per my realization during the course of my research life.

1.1 Nova and its Physical Structure

Novae ("nova" in singular) have been classified as close binary systems with short orbital periods, typically hours ((Walker 1956) and the spectroscopic studies by Kraft (1964)). The separation of the stars is generally $\sim 10^{11}$ cm. There are three main components of a nova system — a primary star, a secondary star, and an accretion disk. The primary star is a white dwarf (WD) can be classified of either carbon & oxygen (CO type) or oxygen & neon (ONe type) type. A wide range of masses, upto the Chandrasekhar limit ($1.4\ M_{\odot},\ M_{\odot}$ = solar mass), is possible for the WD. The secondary is generally a K-M type main sequence star or giant which fills its Roche lobe. Hydrogen rich material from the secondary is accreted onto the surface of the primary through the inner Lagrangian point ($L1$). Having high specific angular momentum, the matter follows an elliptical orbit and does not fall on the primary directly. A redistribution of angular momentum

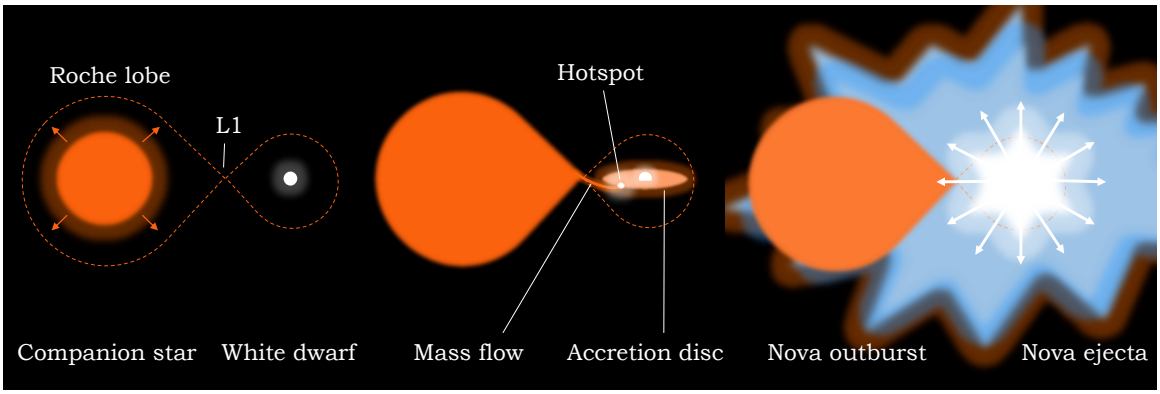

Figure 1.1: Schematic diagram of nova during its various phases. Please see section 1.1 for details.

in the stream leads to the formation of an accretion disk around the primary WD. The gas stream from the $L1$ point hits the accretion disk and generates a hot-spot. Gradual accretion of matter onto the WD surface increases the temperature of the disk resulting in a much hotter and brighter system than the central WD. In the following two subsections, we study the outburst mechanism and post-outburst phases of a nova-system. The physical structure of nova at various stages in shown in Fig. 1.1.

1.1.1 Outburst Mechanism

It is well-known that a nova explosion occurs due to a tremendous thermonuclear explosion on the WD surface. The continuous accumulation of hydrogen-rich matter over a long period, increases the pressure of the inner region (closer to WD surface) of the accretion disk. The bottom of the accreted layer is thus compressed and heated by the strong surface gravity of the WD. Finally, the critical pressure (P_{crit}) is reached which is governed by the following equation (Gerhz et al. 1998):

$$P_{crit} = \frac{GM_{WD}M_{envl}}{4\pi R_{WD}^4}, \tag{1.1}$$

where, M_{WD} and R_{WD} are the mass and radius of white dwarf and M_{envl} is the mass

of the envelope and G is the gravitational constant. For a critical value of the accreted envelope mass of $M_{envl} = 10^4 - 10^5 M_\odot$, $P_{crit} = 2 \times 10^{19}$ dynes cm^{-2}, which is consistent with the hydrostatic models of nova explosion. With pressure, the temperature at the bottom of the accreted layer also increases and when it reaches $\sim 10^6$ K, H-burning starts through $p - p$ chain reactions:

$$\begin{aligned} {}^1\mathrm{H}_1 \ + \ {}^1\mathrm{H}_1 \ &\rightarrow \ {}^2\mathrm{H}_1 \ + \ e^+ \ + \ \nu_e \\ {}^2\mathrm{H}_1 \ + \ {}^1\mathrm{H}_1 \ &\rightarrow \ {}^3\mathrm{He}_2 \ + \ \gamma \\ {}^3\mathrm{He}_2 \ + \ {}^3\mathrm{He}_2 \ &\rightarrow \ {}^4\mathrm{He}_2 \ + \ 2{}^1\mathrm{H}_1 \end{aligned} \tag{1.2}$$

The energy increases slowly initially because the energy generation rate of $p - p$ chain is proportional to $T^4 - T^6$. The temperature gradually increases to $\sim 10^7$ K due to the continuous accretion process. At this point, the CNO reactions take over. These reactions generate a tremendous amount of energy in a very short period of time that results in a thermonuclear runaway (TNR). This explosive H-burning through TNR is commonly known as nova explosion. The $p - p$ chain is relevant in the initial phase of the TNR, while the CNO cycle reactions are important in the final stages. The envelope becomes convective because radiation alone cannot carry out the tremendous amount of energy generated. At $T = 8 \times 10^7$ K, the envelope becomes fully convective. Convection transfers fresh CNO into the high temperature region as well as a significant number of β^+ unstable nuclei to the surface before they decay. There is an increase in the abundance of β^+ unstable nuclei at a temperature of 10^8 K. Huge amount of energy is generated due to the decay of these nuclei. Consequently, the thermal pressure superceeds the electron degeneracy pressure and the envelope expands to counter the excess pressure. The thermonuclear runaway reactions and the nova outburst models are described in detail in many references (for example, Starrfield, Iliadis & Hix in the book *Classical Novae* (eds. Bode & Evans 2008)). The CNO cycle reactions are shown

in Fig. 1.2.

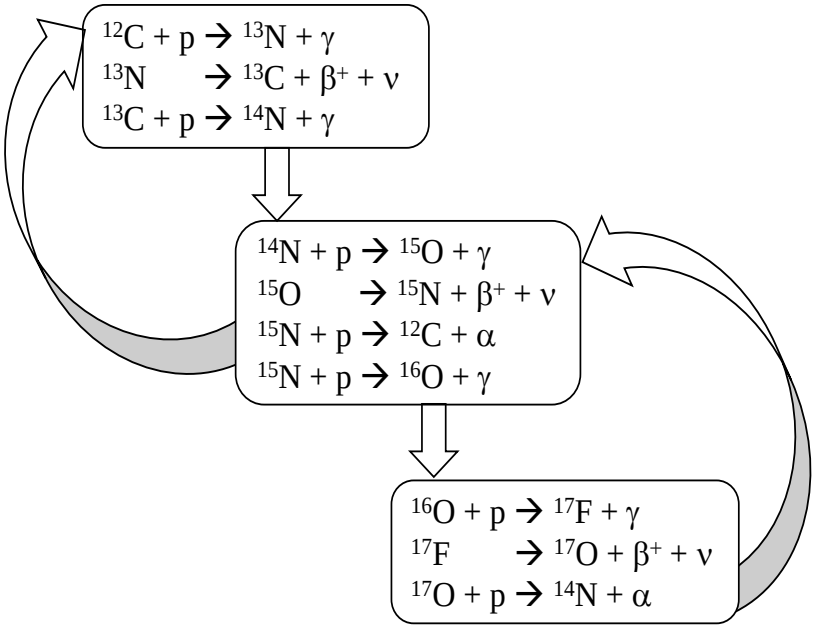

Figure 1.2: Bi-CNO cycle. Please see section 1.1.1 for details.

1.1.2 Post-outburst Phases

In this subsection, we discuss the post-outburst phases, i.e., the different stages through which a nova system passes after its eruption.

- **Fireball Phase:** This phase occurs during the initial expansion when the ejecta is very thick and behaves like a fireball that acts as a hot blackbody and radiates at a temperature of 6,000 - 10,000 K. The pseudo photosphere of the expanding fireball gives rise to the observed light and the nova spectra resemble an A - F spectral type. This phase generally lasts for a few days and ends at a time close

to the point of maximum brightness.

- **Optically thin expansion phase:** As the nova ejecta continues to expand, its density gradually decreases and the shell becomes transparent. This marks the beginning of the optically thin expansion phase. The primary, swollen by hydrostatic burning, now appears as a blue horizontal-branch object. Sometimes, the WD envelope may burn irregularly, resulting in substantial fluctuations in brightness. This phase lasts for a few months.

- **Dust formation phase:** When the temperature of the expanding ejecta reduces to about 2000 K, dust formation occurs due to condensation of C and other elements. The visible light from the nova is diminished by an optically thick shell as the central WD gets completely hidden by the thick envelope of dust. The dust grains absorb the visible light from the WD and re-emits it at IR wavelengths as a 2000 K blackbody. Dust formation mostly occurs in CO type novae. On the contrary, the novae which do not exhibit dust formation, the optically thin ejecta is ionized and excited by the hot central remnant and shows nebular and coronal lines.

The remaining accreted mass on the WD steadily decreases due to the continuous loss of mass through a wind. Consequently, the hydrostatic burning is hindered and the WD begins to cool. Eventually, the binary system returns to its quiescent phase and the accretion process is re-established and it prepares for the next outburst. The recurrence is expected after a time:

$$T_R = M_{crit} / < \dot{M}_{accr} > \tag{1.3}$$

As an example, for the accretion rate $\dot{M}_{accr}$ to be 10^{-8} to 10^{-9} $M_{\odot}$ yr^{-1} , it will take some 10^4 to 10^5 years to build up another surface layer of critical mass $M_{crit} = 10^{-4}$ $M_{\odot}$.

1.2 Classification of Novae

Depending on the mechanism of outburst, novae are classified into several types, namely,

• Classical Novae: Classical novae (CNe) have single observed eruption in a human life-time. They show high-amplitude[1] outbursts ranging from 6 to > 19 magnitudes and the outburst amplitude is strongly associated with the rate of mass transfer from the secondary star onto the WD. The outbursts in classical novae are a result of TNR on the WD surface.

• Recurrent Novae: Unlike CNe, recurrent novae (RNe) show repeated outbursts with recurrence occurring every $\sim 10 - 80$ years. As in the previous case, eruptions in recurrent novae are also caused by TNR on the WD surface. Ten galactic recurrent novae have been identified so far.

• Dwarf Novae: Dwarf novae (DNe) erupt more frequently, ~ 10 d to tens of years, with a well defined time-scale for each nova. They show low-amplitude outbursts, typically of $2 - 5$ magnitudes and reaches upto 8 magnitudes in rare cases. The outbursts in DNe occur as a consequence of the release of gravitational energy caused by large increase in the rate of mass transfer through the accretion disk.

[1]The amplitude of the outburst refers to the difference in the magnitudes before and after eruption.

• Novae Like Variables: Other cataclysmic variables (CVs)[2] such as pre-nova, post-nova, and Z Cam stars fall under this category. Most of these objects show emission line spectra, with certain exceptions, for example, UX UMa stars, which show additional absorption features.

Apart from the above classification, there exists another class of novae called *symbiotic novae*. They are understood as slowly eruptive systems with wide binary systems having separation $\sim 10^{14} - 10^{15}$ cm and long orbital period in the range $200 \leq P_{orb} \leq 1000$ days with certain exceptions. The spectra of symbiotic novae show the absorption lines of a late-type giant together with emission features of H I, He I and other ions of high ionization potential ($\geq$ 20 eV). The spectra during eruption are either characterized by A or F type continuum with additional H I and He I absorption lines or evolves to purely nebular spectra (Warner 1995 and references therein). Ten symbiotic novae have been identified till date. It is presumed that WDs in symbiotic nova systems sometimes accrete matter directly from the wind ejected by the secondary without the formation of an accretion disk.

1.3 Properties of Novae

1.3.1 Light Curves: Characteristic Times & Speed Classes

The modern understanding of novae light curves is credited to McLaughlin. He established (McLaughlin 1939, 1960) that the light curves of almost all novae bear striking similarity if their time scales are optimized properly. These light curves are similar to the extent that they show a rapid rise ($\sim 1 - 3$ d) to maximum magnitude followed by a decline to post-outburst magnitude. However, different novae indeed display very

[2]Novae belong to a broader classification of stellar objects known as cataclysmic variables, which are also binary stars consisting of two components; a white dwarf primary, and a mass transferring secondary. The brightness irregularly increases by a large factor, then drops back down to a quiescent state.

Table 1.1: Speed class of novae.

Author	Speed class	t_2 (in days)	t_3 (in days)
McLaughlin (1945)	Very fast	7	15
	Fast	8-24	15-45
	Average	25-49	50-84
	Slow	50-250	85-449
	RT Ser	> 570	> 1000
Payne-Gaposchkin (1957)	Very fast	<10	<20
	Fast	11-25	21-49
	Moderately fast	26-80	50-140
	Slow	81-150	141-264
	Very slow	151-250	265-440

different rates of decline. In order to have a clear picture, two *characterstic time scales* has to be endefined, *viz.*, t_2 & t_3 which are the time taken to decline, respectively, 2 and 3 magnitudes from the visual maximum. The observed values of these time scales are quite different for different novae. Warner (1995) found a relation between t_2 & t_3 which is given by $t_3 = 2.75{t_2}^{0.88}$. Another important observational property of novae is the *speed class* which is defined as the rate at which the visual light curve decays after the maximum magnitude is reached. McLaughlin (1945) was the first to classify novae on the basis of their speed classes derived from the values of t_2 & t_3. Payne-Gaposchkin (1957) later classified them on the basis of their t_2 times. Classification of novae based on t_2 & t_3 values by McLaughlin (1945) and Payne-Gaposchkin (1957) are shown in Table 1.1.

1.3.2 Light Curves: Evolution

The evolution of a nova light curve generally encounters the following stages. The brightness starts showing weak variations during the *pre-nova* stage and it gradually peaks towards maximum during the *initial rise*, after the eruption occurs. Following

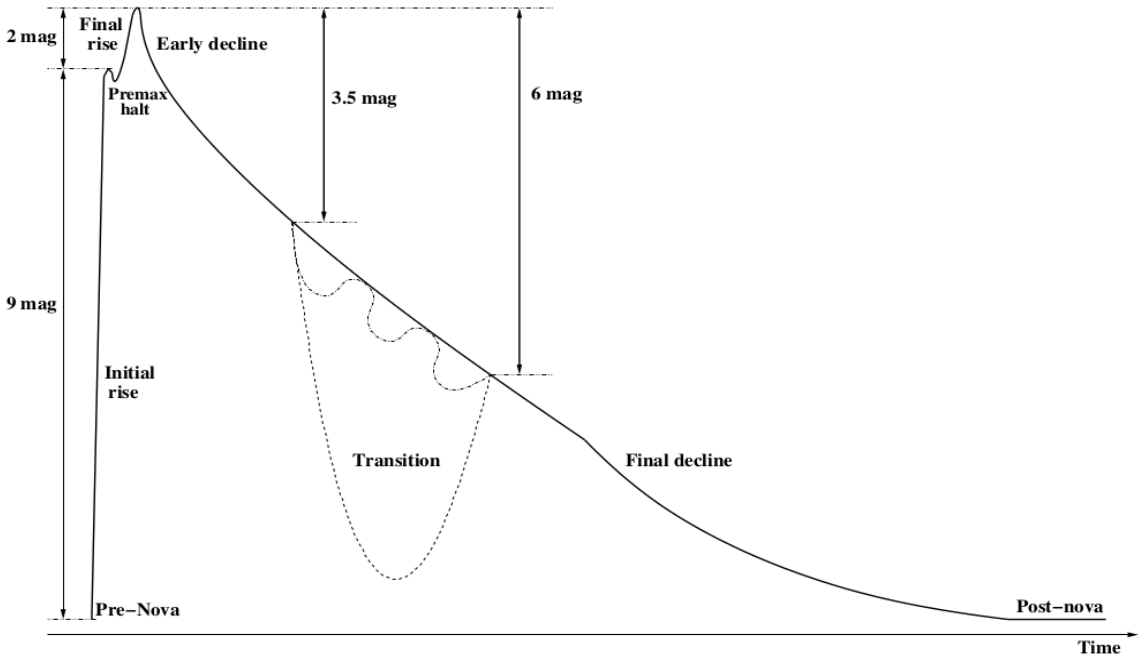

Figure 1.3: Typical light curve of novae (taken from Bode & Evans 2008). The evolution of stages has been mentioned. More description is given in section 1.3.2.

the observations of various novae such as V1500 Cyg and PW Vul (Gerhz 1988 and references therein), nova LMC 1991 (Della Valle 1991), it was found that this phase generally lasts for a week or less. However, it should be mentioned that some novae show a *pre-maximum halt* at about 2 magnitude below maximum which lasts for a few hours in fast novae and a few days in slow novae. The nova then enters the *final rise* phase when it reaches the maximum magnitude. This phase usually lasts for $\sim 1-2$ days for fast novae and several weeks for slow novae. The *principal maximum* phase is relatively short-lived, ranging from a few hours for fast novae to a few days for slow novae. This phase is followed by the *early decline* phase which is usually smooth, except for slow novae, which have brightness variations on time-scales of $\sim 1-20$ days with amplitudes upto ~ 2 mag. At $\sim 3-4$ magnitudes below maximum, the novae enter the *transition phase* when the light curve shows either of the following three distinct possibilities:

• The formation of dust in the ejected gas may lead to a steep decrease in visual brightness, about $7-10$ mag below maximum. This may last for months or even a few years, after which the nova recovers and follow the extrapolated decline.

• There may be large amplitude oscillations with quasi-periods of about $5-15$ days and amplitudes of up to 1.5 mag.

• The light curve follows a smooth decline without any noticeable peculiarities. About one-third of the fast and very-fast novae, as well as a few slower ones, pass through this transition region.

It then slowly goes through *final decline* and enters the *post-nova* or *quiescence* phase. A typical lightcurve during different phases of novae is shown in Fig. 1.3.

1.3.3 Evolution of Spectra

This subsection deals with the evolution of various stages of the novae spectra — the pre-maximum spectrum, the principal spectrum, the diffused enhanced spectrum, the orion spectrum, the nebular spectrum, and the post-nova or the quiescence spectrum.

- **The Pre-Maximum Spectrum:** This is the first stage of the expansion in which the spectrum is dominated by strong continuum and blue-shifted absorption lines (known as P-Cygni profile), similar to those of early type stars. The broad lines are signatures of a high expansion velocity. The spectrum in this phase is characterized by a uniformly expanding optically thick, cooling ejecta.

- **The Principal Spectrum:** This phase occurs at about 0.6 mag below maximum. The spectrum is characterized by strong absorption lines and resembles A to F supergiants with enhanced CNO lines. The spectrum is dominated by low-ionization species such as, H (strongest), O, C and singly ionized and neutral iron peak species (such as Fe I, Fe II and Ti II). Some novae show neutral He absorption lines at this stage and also P-Cygni profile for the optical Na I lines. P-Cygni structure is present for Mg II 2880 Å line in UV. The velocities of ejecta are larger as compared to those seen during the pre-maximum phase. O I 5577 Å, 6300 Å and 6364 Å are the strongest emission lines observed, which indicates the presence of a neutral zone.

  As the nova declines from maximum, the absorption features weaken, giving way to a pure emission spectrum by the end of the early decline. This phase is characterized but the appearance of [O I] and [N II] emission lines, followed by [O II]. The emission line profiles are signatures of non-uniform ejection of gas. In the UV region, emission lines of He II; Mg II; Al II - III; Si II - III; N III - V; O III - V and C II - IV appear. Strong emission lines of H I, He I, C I, O I and Na I appear in the IR region.

- **The Diffused Enhanced Spectrum:** This phase appears mostly in CO type novae with broad diffused absorption lines similar to those observed in the principal spectrum but with velocities almost twice as large. Similar to the principal spectrum, P-Cygni profile appears with broad emission of the diffused enhanced system and it reaches a maximum at 2 mag below maximum. Later, these absorption lines often split into finer structures.

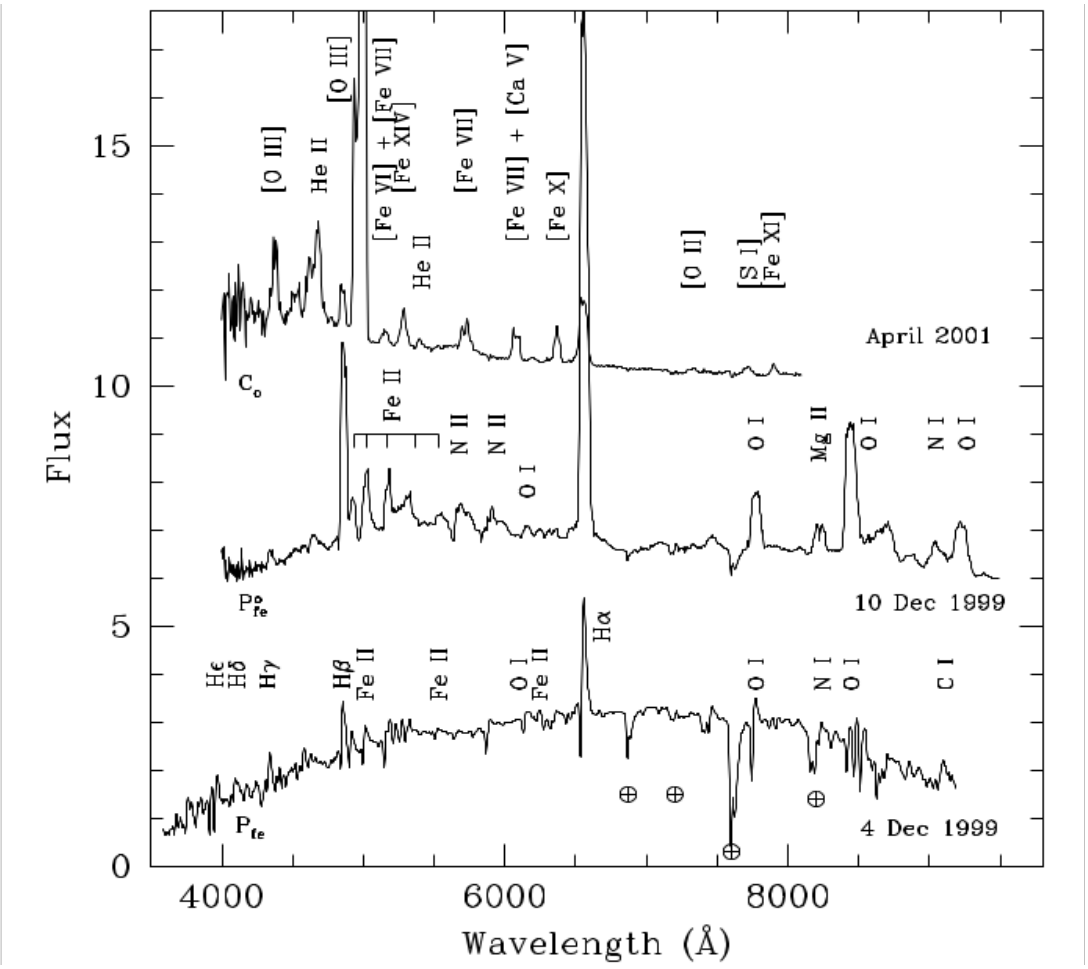

Figure 1.4: The evolutionary sequence of nova V1494 Aql showing the change from a permitted to coronal spectrum as labelled on the left side of each spectrum. Dates of observations are labelled on the right side of each spectrum. More descriptions are given in section 1.3.3.

- **The Orion Spectrum:** The Orion spectrum generally appears after the novae decline by $1-2$ mag from the maximum. This phase derives its name from its similarity to the stellar wind absorption lines in luminous OB stars. Prominent emission features are from He I, C II, N II and O II initially and N III and N V later. The absorption lines in this stage are usually single, diffused with velocities that are at least as much as the diffused enhanced system. The absorption features are most enhanced at 2.7 mag below maximum when it is accompanied by the emergence of N III absorption lines. This features dissappear at 3.2 mag

below maximum when the novae enter the transition phase. The disappearance of the absorption component is followed by the increase in intensity of emission line component. Particular species of both absorption and emission components may become very strong occasionally. A typical example is the nitrogen flaring, which occurs at about 3 mag below maximum due to blending of the N III multiplet lines at 4640 Å, and other N II and N III lines. Later, the spectrum shows forbidden lines of Fe II in emission along with the occurrence of He II 4686 Å emission line. The emission line spectrum in the UV remains similar throughout the principal, diffused enhanced and orion stages. The prominent change is an increase in equivalent widths with the decay in continuum (Williams et al. 1985).

- **The Nebular Spectrum:** This is an emission spectrum, initially dominated by [O I] and [N II] components of principal spectrum, followed by the emergence of [O III] and [Ne III]. The spectrum gradually becomes similar to that of a planetary nebula. When the ionizing radiation reaches a temperature over 10^6 K, coronal lines along with lines from sucessive ionization states from [Fe II] through [Fe XIV] and other higher ionization lines of abundant elements such as [Ca V, XV], [Ni XII] develop. Strong lines of Ne, especially [Ne III] and [Ne V] are shown by some novae which have been designated as *Neon novae*. In the UV, lines of [Ne III, IV, V], [Na V, VI], [Mg V, VII], [Al VI, VIII], [Si VII, IX] are seen (Williams et al. 1985). [Mg VIII], [Si IX], [Al IX] lines appear in the IR and Mg I, Na I, C I, [Mn XIV], [Si VI], [Al IX] lines appear in the NIR (Ashok & Banerjee, 2003).

- **The Post-nova or Quiescence Spectrum:** The ejected shell may become spatially resolvable after some years. Consequently, spectra of individual components of the ejecta can be obtained. The emission spectra of these shells are generally dominated by permitted recombination lines of H, He, C, N and O, with the ad-

dition of [N III] and strong Balmer continuum emission.

As an example, the evolutionary spectral sequence of nova V1494 Aql is shown in Fig. 1.4 where the change of spectrum from permitted to coronal phase is observed. The nova reached at a maximum brightness of visual magnitude of 4.0 on Dec 3.4, 1999, followed by a rapid decline making this a fast nova. Dates of the observations taken are mentioned beside each spectrum, representing the various phases of spectral evolution: fireball phase (Dec 4, 1999), early-decline phase (Dec 10, 1999), and nebular phase (April, 2001) (Kamath et al. 2005)

1.3.4 Modern Spectral Classification

Modern spectral classification is based on the understanding of permitted lines generated by the photoionization of the expanded ejecta by hard radiation from the central source (Williams 1990, 1992). Depending on the spectral features, novae are classified into three categories:

- **Fe II type:** This class of novae comprise about 60% of the total and exhibit low ionization lines with the strongest non-Balmer lines being the Fe II lines. The later originate from the optically thick wind surrounding the WD. Their spectra develope slowly and generally show P-Cygni type absorption features. Low ionization lines of Na I, Mg I, Ca II etc. are observed in the early spectrum. The expansion velocity ranges between 1000 km/s and 3500 km/s.

- **He/N type:** The strongest non-Balmer lines such as He I, He II/N II, N III dominate the spectrum of He/N novae. These lines are formed in the discrete shell of the ejected gas. The emission lines have higher excitation levels, are broader and fast evolving as compared to the Fe II type of novae. The expansion velocity is generally greater than 2500 km/s. He/N type novae evolve into either Neon novae or into the coronal class.

- **Hybrid Novae:** The hybrid novae, also known as Fe II*b*, are those novae systems whose spectral class undergoes a transition from Fe II to He/N during the permitted lines phase, before the appearance of the forbidden lines. In contrast to the Fe II class, a higher expansion velocity is indicated by the line-widths. The line-profiles also show evidence for shell ejection as well as ejection of matter through a weak wind. The novae V5114 Sgr, a moderately fast nova with a smooth decline, is a particular example of hybrid nova.

In addition to the different spectral classes of novae discussed above, a new species of nova has also been discovered which are characterized by their hydrogen deficiency. The first such nova to be discovered was V445 Pup in 2000 whose early spectra did not have any hydrogen lines. Instead, it was dominated by numerous emission lines of Fe II, Na I, C II and He I . Several lines of N I, C I and Mg II were also observed.

Based on IR observation and depending on the type of WD novae can be classified into two groups:

- **CO Novae:** They are characterized by the explosions occurring on the CO WDs

which have low masses ($M_{WD} < 1.2\ M_{\odot}$). They evolve slowly with a low expansion velocity. These novae form abundant dust, either optically thin or thick. The spectrum shows enhanced CNO lines, while the He/H ratio is near the solar abundance.

- **ONe Novae:** These are characterized by the explosions occurring on the ONe WDs which are massive ($M_{WD} > 1.2\ M_{\odot}$) as compared to CO WDs. They are fast evolving with high expansion velocities and are generally dust-free. They are particularly distinguished by the strong, early emission line of [Ne II] 12.8 μm, which has led to their characterization as 'Neon novae'. The spectrum generally shows evidence of carbon reduction relative to solar, with associated enhancements of oxygen and neon.

1.3.5 Maximum Magnitude Vs. Rate of Decline (MMRD) Relation

Nova explosions occur frequently and are known to radiate almost at constant bolometric luminosity[3] during their outburst. These properties make novae potential extra-galactic distance indicators. Hubble first noticed that the brightest nova in M31 declined fastest (Hubble 1929). Several years later, McLaughlin finally established a relationship between the luminosity of a nova and its rate of decline (McLaughlin 1945), which is known as the maximum magnitude vs rate of decline (MMRD) relation. The observational results regarding the MMRD relations were first given by Della Vale & Livio (Della Vale & Livio 1995). The MMRD relation relates the absolute magnitude (M)

[3]Luminosity is the amount of electromagnetic energy that a body radiates per unit of time and bolometric luminosity is the luminosity of an object measured over all wavelengths.

Table 1.2: Typical values of MMRD constants.

M	n	a_n	b_n	References
pg	3	-11.3	2.4	de Vaucouleurs (1978)
B	3	-10.67 ($\pm$ 0.30)	1.80 ($\pm$ 0.20)	Pfau (1976)
V	2	-10.70 ($\pm$ 0.30)	2.41 ($\pm$ 0.23)	Cohen (1985)
V	2	-11.32 ($\pm$ 0.44)	2.55 ($\pm$ 0.32)	Downes & Duerbeck (2000)
V	3	-11.99 ($\pm$ 0.56)	2.54 ($\pm$ 0.35)	Downes & Duerbeck (2000)

and $log(t_n)$ by a linear relationship as follows:

$$M = b_n log(t_n) - a_n \tag{1.4}$$

where, t_n is the characteristic time in days and a_n & b_n are the parameters' values. Typical values of a_n & b_n are given in Table 1.2

The linear MMRD relations provide satisfactory fits for galactic novae; however, in recent years, more complicated emperical relationships have been proposed which improve the fit when extra-galactic data are included. An example of such relation for novae in M31 and the LMC as given by Della Vale & Livio (1995) is:

$$M_V = -7.92 - 0.81 arctan \frac{1.32 - logt_2}{0.23} \tag{1.5}$$

and is shown graphically in Fig. 1.5

1.4 Physical Parameters of Novae

In the following subsections, we discuss several physical parameters of novae which play crucial roles in studying and understanding the nova-system in details.

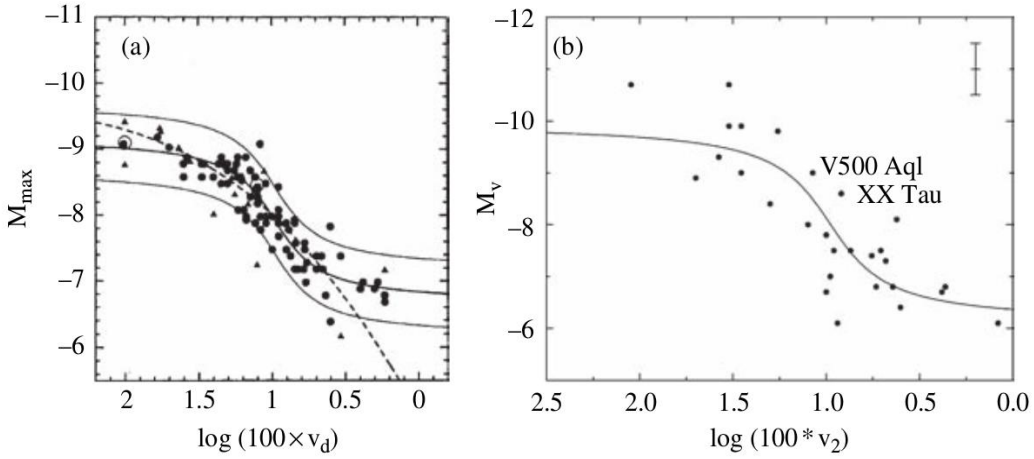

Figure 1.5: MMRD relationship for novae in M31 galaxy (left panel, from Della Valle & Livio 1995) and for Galactic novae (right panel, from Downes & Duerbeck 2000). The 'S-shaped curves are empirical fits of the form given in Equation 1.5. The dashed line represents the theoretical relation from Livio 1992; (taken from Bode & Evans 2008). More description is given in section 1.3.5.

1.4.1 Bolometric Luminosity

Modern observations suggest that nova eruption have bolometric luminosities that are all at or somewhat above the Eddington luminosity. The latter is defined as the maximum luminosity which a star of a given mass can have before the outward radiation pressure exceeds the inward gravitational force. Mathematically, it is represented by the equation:

$$L_{Edd} = \frac{4\pi G c M_{WD}}{\kappa_T} \tag{1.6}$$

where velocity of light, $c = 2.9979 \times 10^{10}$ cm s^{-1} and κ_T is the Thomson opacity for scattering by free electrons, whose value is equal to 0.3975 cm^2 g^{-1} for hydrogen (Gerhz et al. 1998).

The continuum of the spectra reveals the effective temperature as well as the luminosity of the object. By fitting of blackbody radiation curves, we can determine the

temperature of the system. Luminosity can also be calculated from the total flux of the emission spectra.

1.4.2 Mass and orbital period

The orbital period (P_{orb}) and the mass of the components define the dimension of a binary system. For a binary system consisting of a Roche-lobe-filling main sequence secondary, the relation between mass of the components and P_{orb} is given by the generalized equation of Newton, derived from Kepler's third law:

$$P_{orb}^2 = \frac{4\pi^2 a^3}{G[M_{WD}] + M_{sec}} \tag{1.7}$$

where, M_{WD} and M_{sec} are the mass of the WD and secondary component respectively and a is the separation between them. The orbital period of a cataclysmic variable is its most precisely known parameter.

P_{orb} lies between several minutes to several hours. From observational studies of several CVs, it has been found that for about 66% CVs, 3 hr $< P_{orb} <$ 14 hr and for about 33% CVs, 80 min $< P_{orb} <$ 2 hr. And there present an almost total deficiency of CVs for 2 hr $< P_{orb} <$ 3 hr, which is commonly referred to as *period-gap*.

1.4.3 Expansion Velocity and Geometry of the ejecta

Using the Doppler shift relation, the expansion velocity of the ejecta (v_{ej}) can be measured from the spectral line-width:

$$\frac{v_{ej}}{c} = \frac{FWHM}{\lambda}, \tag{1.8}$$

where, c, the velocity of light, $= 2.9979 \times 10^{10}$ cm s^{-1} and $FWHM$ is the full width at half maxima of the spectral line at wavelength λ.

The structure of individual emission line profiles during the optically thin phase contains the signature of geometry of the ejecta. The profiles of the emission peaks reveal the velocity and also direction of the wind. Also, long before the emission lines appear, the absorption line features during the Fe-curtain phase exhibit the geometrical structure of the system.

1.4.4 Mass of the ejected gas

Mass of the ejected gas is a crucial parameter for understanding nova systems. It helps to construct the TNR models more accurately and also to determine the elemental abundances in the ejecta. From models generated using photoionization code CLOUDY (details in Chapter 2), mass of the ejected gas can be estimated. Mass of hydrogen in each shell can be added up and multiplied by the covering factor (f) to estimate the total ejected mass of hydrogen in the nova ejecta (Schwarz et al. 2001; Schwarz 2002) using the following equation:

$$M_{ej} = f \times n(r_0) f(r_0) \int_{R_{in}}^{R_{out}} (r/r_0)^{\alpha+\beta} 4\pi r^2 dr, \tag{1.9}$$

where R_{in}, R_{out} are the inner and outer radii of the ejecta, α & β are exponents of power laws, $n(r_0)$ is the hydrogen density at the inner radius and $f(r_0)$ is filling factor at the inner radius.

Table 1.3: Deduction from optical observations of novae.

Parameter	Estimates
He I 5876/4471	E_{B-V}
Balmer and Paschen series	E_{B-V}
Colour index and MMRD relation	E_{B-V}
[O I] 5577/6300	Temperature of neutral zone
Hα, Hβ fluxes and velocity	Ejecta mass (hydrogen)
He I 4471, 5876, 6678 and He II 4686 fluxes	Helium abundance
Hydrogen and He I line ratios	Zanstra temperature of the central source
[O I] 6300, 6363	Neutral Oxygen mass
[O III] Nebular line ratio	Temperature of ionized zone
Velocity and line profile evolution	Geometry of the ejecta, interaction with environment
Light curve shape and spectral evolution	Mode of ejection of matter, WD mass and type

1.4.5 Ejecta abundances

It is well-known that nova ejecta is rich in metal, about 10 - 100 times the cosmic abundances (José & Hernanz 1998). Study of chemical abundance of nova helps us to understand the chemical evolution of galaxy. There exist different techniques of abundance analysis of novae ejecta during different stages of outburst (Boyarchuk & Antipova 1990; Snijders 1990). Compositions and physical conditions of the nova ejecta can be derived from the modelling of spectral lines using various computational codes, *viz.*, CLOUDY, PHOENIX etc. In the present work, I have used CLOUDY photoionization code (details in Chapter 2) to determine the elemental abundances of the ejecta by matching the emission line flux ratios of various elements of modelled spectra with the observed one.

1.5 Multiwavelength Aspects of Novae

To understand nova phenomenon properly, emissions from novae should be studied at all wavelengths since they emit their energy over the entire electromagnetic spectrum. At early times, only optical observations were possible due to lack of sophisticated instruments and non-uniformity of atmospheric transformations. With the advent of modern digital detectors, both on the ground as well as on the satellites into space, it has been possible to observe novae at multiple wavelengths. A detailed study of such multiwavelenth observations are discussed below.

γ-rays :

Clayton & Hoyle (1974) were the first to point out that novae could be considered as potential γ-ray emitters. They stated that γ-rays in novae arise due to electron-positron annihilation, with positrons from decay of ^{13}N, ^{14}O, ^{15}O and ^{22}Na as well as due to the decay of ^{14}O and ^{22}Na to excited states of ^{14}N and ^{22}Ne nuclei. The launch of the INTEGRAL (INTEnational Gamma-Ray Astrophysics Laboratory) satellite in 2002 by the European Space Agency facilitated the detection of γ-rays due to nuclear radioactivity in astrophysical objects like novae. Novae emit γ-rays because some of the radioactive nuclei synthesized during the thermonuclear runaway, either experience electron capture or are β^+ unstable (thus emitting positrons). They decay in some cases to nuclei in excited states which de-excite to their ground states by emitting photons at particular energies in the γ-ray range. The positrons annihilate with electrons and therefore also produce γ-ray emission (Leising & Clayton 1987). So, γ-rays provide a clear picture of the nucleosynthesis occurring during nova-explosions and also of the physical parameters such as the density, temperature, chemical composition and velocity profile of the ejecta.

X-rays :

The X-ray emissions are best suited to study the hot phases in a nova outburst. No-

vae may emit X-rays due to four different mechanisms (Krautter 2008 and references therein):

1. Thermal emission from the hot WD remnant during the initial as well as later phases of the outburst.

2. Interaction between the nova ejecta and the surrounding medium of the nova system.

3. Restart of an accretion through an accretion disk or magnetic accretion.

4. Hard X-rays resulting from Compton downgradation of γ-rays produced by the radioactive decay of ^{22}Na (Livio & Truran 1992). However, emission of X-rays by this process is yet to be observed.

The advancement of X-ray observations was aided by the launch of several satellites, particularly, UHURU in 1970 and the High Energy Astrophysical Observatory B ('Einstein') in 1978 and ROSAT in 1990, Chandra and XMM-Newton in 1999 and SWIFT in 2004.

Ultra-Violet (UV) rays :

Nebular emission and emission from the pseudo photosphere together generate UV radiation from novae. The chemical abundances in the ejecta are accurately determined with the help of the UV data (Stickland et al. 1981; Williams et al. 1985; Snijders et al. 1987). Also, the nature of the WD components can be determined by analysing the UV spectrum. Most importantly, the UV observations enable us to determine strength of the 2200 Å dust profile accurately which in turn helps to evaluate the energy-budget of novae and the temperature of the remnants. It is worthwhile to mention that the IUE (International Ultraviolet Explorer), launched in 1978, provided the largest source of UV observations.

Optical rays :

Information about many physical parameters such as temperature, density and optical depth conditions in the ejecta, as well as the temperature of the central WD can be directly obtained from the optical spectrum i.e., from the lines of various species and ionization levels, and their relative fluxes. The geometry of the ejecta can be understood by the evolution of the line-profiles (Shore 2012; Anupama & Kamath 2012). The information about the nebular phase is obtained from the line ratios of [O III] (4959+5007)/4363 Å; [O III] (4959+5007)/[Ne III] 3869 Å and [O III] (4959+5007)/He I 5876 Å (Starrfield 1988). Table 1.3 provides a few examples of the parameters which could be deduced from optical observations (Anupama & Kamath 2012).

Infra-Red (IR) rays :

During the various stages of evolution of novae, they release a significant amount of energy at IR wavelength. IR observations have contributed substantially to our understanding of how classical novae participate in the chemical evolution of the galaxy. They have also led to the classification of novae into CO and ONe types (Gehrz et al. 1993; Gehrz et al. 1998; Gehrz 2002). IR emissions are generally seen in the optically thick ejecta during the fireball phase, thermal Bremstrahlung during the free-expansion phase, dust formation in the ejecta, from X-ray heated grains etc. The IR observations are also useful to determine the abundances of different metals present in the ejecta.

Radio waves :

The primary cause of radio emission from novae is thermal Bremsstrahlung. Radio observations are particularly useful to estimate the optically thick radio surface brightness and hence the electron temperature. Distances to nova can be estimated by comparing the absorption line velocities with the angular expansion rates obtained from radio observations. They can also be used to probe the large scale structure of the binaries on the scale of $\gtrsim 10^{11}$ cm. The three-element interferometer at Green Bank, West Virginia, the

Westerbork Synthesis Radio Telescope (WSRT), the Very Large Array (VLA) in New Mexico, and the MERLIN network of telescopes (Seaquist & Bode 2008) have made the most radio observations till date. The first classical novae detected in radio wavelengths were HR Del and FH Ser by Hjellming & Wade (1970).

1.6 Importance of Novae in Astronomical Context

New observational data collected with several sofisticated telescopes and satellites during the past few decades have helped us in a better understanding of novae systems. They have been proved to be important sources to understand the physics of observational properties which are found in other exciting areas of astrophysics. For example, it is well established that accretion disks are formed in novae systems and thus observational studies of the accretion process can be carried out more effectively in this binary-systems, particularly those which are closer to us. Metal abundances in the galactic environment is enriched by the novae ejecta due to high abundance of metals in the ejecta. A significant amount of dust and molecules such as CO, H, PAH are formed in novae systems which eventually integrate with the interstellar medium. Although CVs share only about 0.1% of the total dust formation in the galaxy, nevertheless, they allow direct observation of the evolution of circumstellar grain formation events on a frequent basis. Novae explosions also allow the synthesis of several radioactive nuclei like ^{26}Al, ^{22}Na, ^{7}Li which contribute significantly to the galactic budget of these elements. High abundances of C, N, O, Ne, Mg, Al & Si in some novae seem to suggest that novae systems contribute to potential chemical anomalies on local and galactic scales.

It is also worthwhile to note that RNe are believed to be the progenitors of type Ia supernovae. So, RNe provide the opportunity to study the physics of type Ia super-

novae. It is well-known that the absolute magnitude of novae ranges between -9 and -7 which means that novae are some of the most luminous sources in the sky. This property of novae helps in measuring intergalactic distances. Thus, in view of the above significances, it is clear that observational studies of novae provide testing grounds for theoretical concepts which may then be applied to understand various astrophysical events.

1.7 Motivation for Present Work

In the last few decades, significant progress has been made in understanding novae outburst due to improved techniques in observational as well as in theoretical sciences. In spite of that, there are still many unsolved problems that make our understanding of the nova theory incomplete. Therefore, to understand them properly we need long time observations over wide wavelength range, analysis and proper interpretation of data to understand the phenomena. For example, the physical conditions in the nova ejecta can be understood by a rigorous study of the spectroscopic evolution of the nova as it passes through various phases. The temperature, density, and the optical depth conditions in the ejecta, as well as the temperature and brightness of the central white dwarf are directly related to the emergence of the lines of various species and ionization levels, and their relative fluxes. The physical conditions in the ejecta and the geometry of the ejecta can be determined from the emission line fluxes and the line profiles. Early phase spectra generally show the signatures of optically thick ejecta. At this stage, the ejecta should be investigated utilizing model environments containing model atmospheres including the appropriate physics like non-local thermodynamic equilibrium and spherical geometry. The density drops as the nova shell expands and the nebular emission lines begin to appear as the ejecta become optically thin. At this stage, the shell should be modelled utilizing standard nebular techniques. As the nova goes into the quiescence

or post nova phase, the emission lines from higher ionization disappears and absorption features from the secondary dominates. Combination of modelled spectra can be used to understand these spectra.

The prime objective for present investigation is to study the spectroscopic behaviour of novae through various phases. In the present thesis, I have attempted to understand few of such aspects through study of 2006 outburst of the recurrent nova RS Ophiuchi (RS Oph), calculation of hydrogen line fluxes under different physical conditions in nova atmosphere, and study of novae in quiescence period. For these studies, I have taken observations of spectroscopic data of various novae in the multiwavelength regions and reduced and analysed those data. I have used CLOUDY photoionization code to model those data to infer the physical parameters of the systems. The methodology and results obtained so far are described in the following chapters.

This thesis is organized as follows; the methodology including observational dataset and modelling procedure are discussed in details in Chapter 2, study of RS Oph is discussed in Chapter 3, a grid model of novae generated using photoionization code CLOUDY is described in Chapter 4, analysis and modelling of quiescence phase spectra of several novae and their comparative study is discussed in Chapter 5, and finallly the works are summarized and conclusions and scope for future study are given in Chapter 6.

Chapter 2

Methodology

For the present work, I have used observational and published spectroscopic data of several novae and modelled them using photoionization code. In the following sections, description of observation, data reduction and the modelling procedure are discussed.

2.1 Dataset

2.1.1 Observational Data

I have taken observations at 2m Himalaya Chandra Telescope (HCT), situated at Hanle, Ladakh, India. The observing nights were achieved through submission of observation proposal titled "Optical and Near Infrared (NIR) observations of Classical, Recurrent and Symbiotic Novae" and I have been alloted 19 nights for observations during April, 2015 - December, 2016. During this time period I have spectroscopically observed 14 old and new novae in optical (3400 - 9200Å) and near-infrared (1.02 - 2.35 μm) region. Out of these, I have completely analyzed, modelled and interpreted data of four novae (T CrB, GK Per, RS Oph and BX Mon). The results are discussed in Chapter 5. The log of observations is presented in Table 2.2.

Telescope

The 2.01m aperture optical-infrared Himalayan Chandran Telescope (HCT - *https://www.iiap.res.in/telescope_iao*) is installed at the Indian Astronomical Observatory (IAO - *https://www.iiap.res.in/centres_iao.htm*), situated at the Hanley valley of Changthang (Latitude: 32° 46′ 46″ N; Longitude: 78° 57′ 51″ E), Ladakh, at an altitude of $\sim$ 4500 meters (Fig. 2.1). The telescope is remotely operated via a dedicated INSAT-3B satellite link from Centre for Research & Education in Science & Technology (CREST), Hosakote, under Indian Institute of Astrophysics (IIA), Bangalore. HCT is named after Nobel laureate Subrahmanyam Chandrashekhar. It is a modified Ritchey-Chrétien type Cassegrain system with an altitude over azimuth mount. The telescope contains a $f/1.75$ primary and infrared-optimizde secondary. The Cassegrain focal ratio of $f/9$ provides an image scale of 11.5 arcsec/mm (Prabhu 2014).

Detectors

Detectors are used at the primary focus of the telescope to capture light/photons from the astronomical objects and converts it to digital data. The quality of an image depends on the resolution of the sensor. A typical CCD (charged coupled device) camera, used with an optical/NIR telescope, consists of a thin silicon (semi-conducting material) wafer divided in an array of thousands (or millions) of tiny light sensitive square (pixel) or photosites. Each pixel (typically a few microns in size) has a tiny capacitor that holds charge. These charged capacitors attract electrons and when the light enters the array, it liberates the electron from Si atom. Thus, CCDs operate on the principle of photoelectric effect. CCDs are exposed for a few seconds (integration time) to capture sufficient electrons and each individual pixel collects the produced electrons at the end of integration time. From the readings of individual pixels, a digital image of the celestial object is produced in the computer. CCDs are usually cooled down ($\sim$ -120° C using

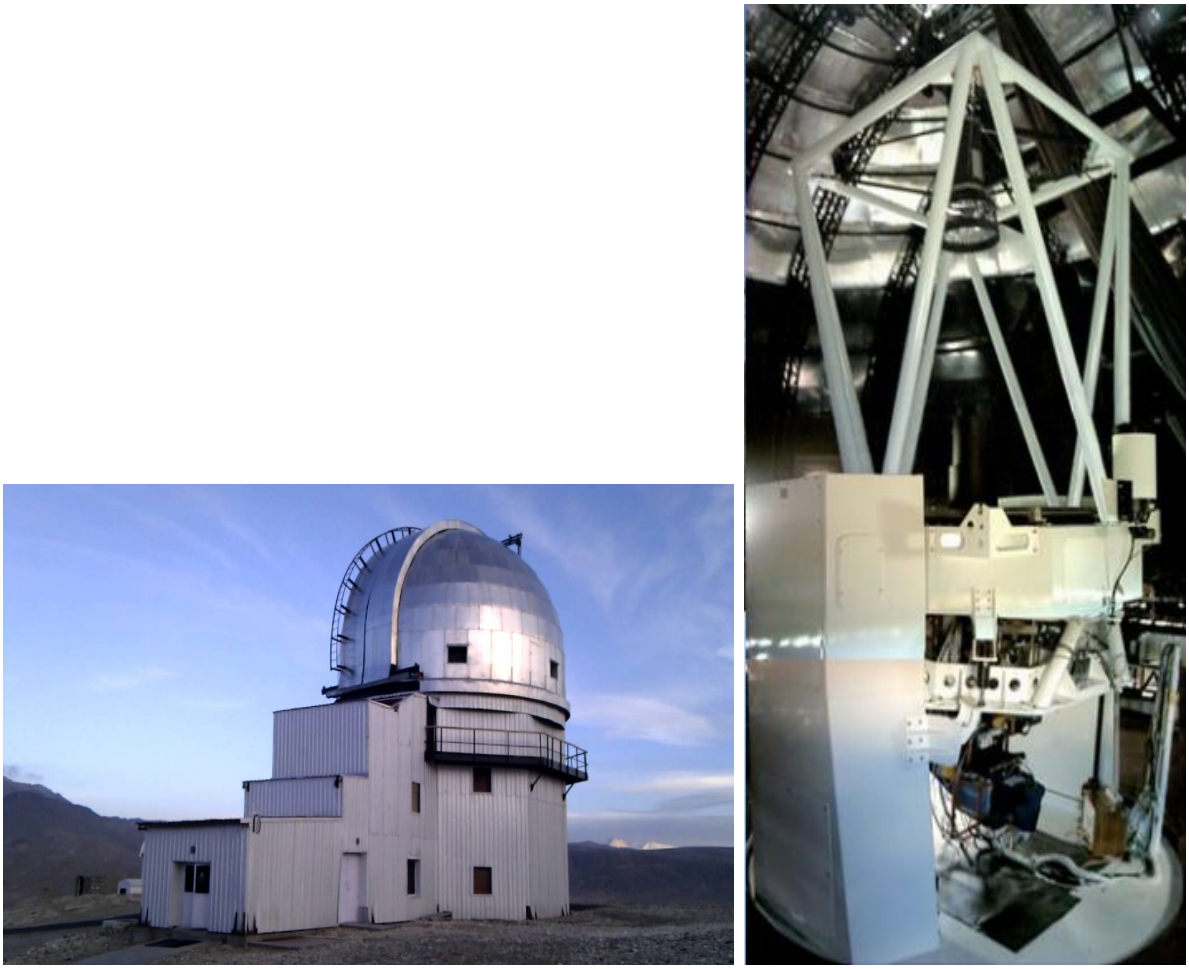

Figure 2.1: HCT observatory (left) and the telescope (right). More descriptions are given in section 2.1.

liquid nitrogen) to minimize the effect of thermal noise.

Instruments

HFOSC : The Himalaya Faint Object Spectrograph Camera (HFOSC - *https://www.iiap.res.in/iao_2m_hfosc*) is an optical imager cum spectrograph, mounted on the axial port of HCT (Fig. 2.2). It was designed and fabricated in collaboration with the Copenhagen University Observatory and is used for optical imaging and spectroscopy. The instrument is a focal reducer type instrument and allows low and

medium resolution grism spectroscopy. HFOSC is operated in the wavelength range of 3500 - 9000 Å using a 2048 × 4096 pixels CCD detector with pixel size of 15 × 15 microns. HFOSC offers spectral resolution ranging from $R \sim 150$ to 4500 using a set of 11 grisms. Imaging field of view is 10 × 10 arcmin^2 (unvignetted) onto 2K × 2K part of CCD camera. HFOSC uses Bessell U (3727 Å), B (4861 Å), V (5007 Å), R (6563 Å), and I (6724 Å) filters with a signal to noise ratio of S/N = 22 for 20 min exposer time.

TIRSPEC : TIFR Near Infrared Spectrometer and Imager (TIRSPEC - https://web.tifr.res.in/∼daa/tirspec/) is used for NIR medium resolution spectroscopy as well as imaging (Fig. 2.2). TIRSPEC was developed by the Infrared Astronomy Group of Tata Institute of Fundamental Research, Mumbai, in collaboration with Mauna Kea Infrared (MKIR), Hawaii. TIRSPEC is operated in the wavelength range of 1.02 - 2.35 μm using a 1K × 1K Hawaii-1 array CCD detector with 18 micron pixel size. Field of view is 307 × 307 arcsec^2 and spectral resolution is $R \sim 1200$. TIRSPEC uses the filters: Methane off (1.584 μm); [Fe II] (1.645 μm); Methane on (1.654 μm); H2 (1-0) (2.1239 μm); Br Gamma (2.166 μm); K-Cont (2.273 μm) and CO (2-0) (2.287 μm). The signal to noise ratio is calculated using gain ($\sim$ 5 e/ADU), readout noise (4.3 ADU), and number of non-destructive readouts in the exposure using the error propagation formula. In the J-band, for a 16 mag object, S/N = 125 for 7.5 min exposer time for 1 $FWHM$ (Ninan et al. 2014).

Specifications of the instruments are summarized in Table 2.1.

2.1.2 Data reduction

The ground based telescopes suffer from atmospheric extinction from night to night, which can severely affect the image quality. In addition to registering signals from the

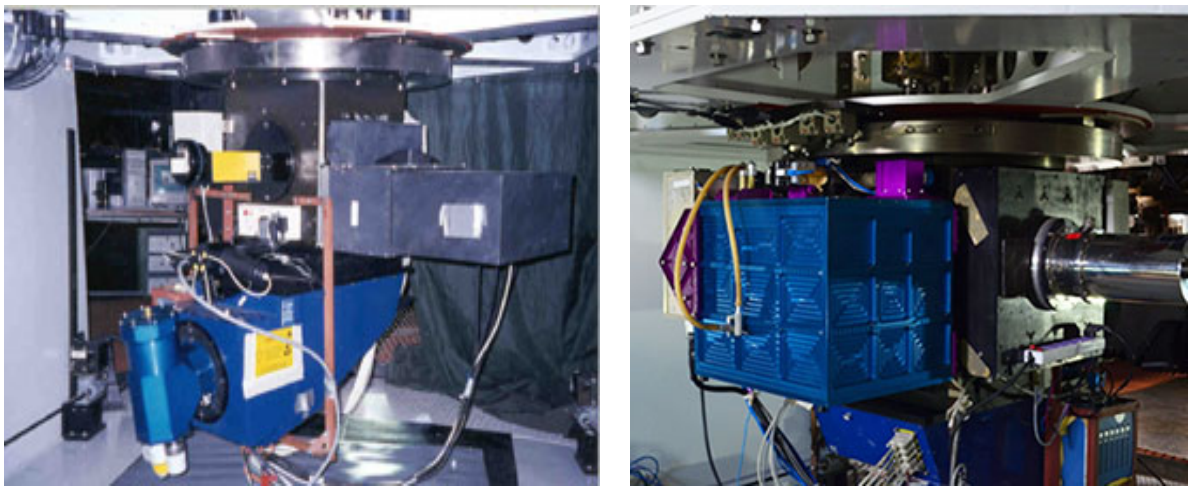

Figure 2.2: HFOSC (left) and TIRSPEC (right) instruments attached with the telescope. More descriptions are given in section 2.1.

source image, the raw observed image also contains unwanted background emission from the telescope and the atmosphere, and a number of instrumental effects (e.g., geometrical distortion; bad, hot & cold pixels; electronics associated with the CCDs; different kinds of noises; effects of cosmic rays etc). All these effects are removed from the raw CCD frames to get the proper spectrum of the source. In order to achieve this, data have been reduced folllowing standard precedures. I have used IRAF (Image Reduction and Analysis Facility) package (*https://iraf.noao.edu*) for optical region and TIRSPEC pipeline (*https://github.com/indiajoe/TIRSPEC/wiki*) for NIR region.

Optical data reduction procedure:

IRAF is a collection of softwares geared towards the reduction of astronomical images in pixel array form. It is distributed by the National Optical Astronomy Observatories, Arizona which are operated by the Association of Universities for Research in Astronomy, Inc., under co-operative agreement with the National Science Foundation. The HCT optical spectra were obtained using HFOSC through Grism #7 (Resolution $\sim$ 1500) and Grism #8 ($R \sim 2200$) covering the wavelength ranges of 3400 - 8000 Å and

Table 2.1: Specifications of HCT instruments.

	HFOSC	TIRSPEC
Wavelength range	3500 - 9000 Å	1 - 2.5 μm
Detector	2048 × 4096 pixels CCD with pixel size 15 × 15 microns (0.3×0.3 arcsec^2 in the image plane)	18 micron pixel, 1024 × 1024 format Hawaii-1 array
Field of view	10 × 10 arcmin^2 (unvignetted)	307 × 307 arcsec^2
Resolution	$R \sim$ 150 - 4500 using a set of 11 grisms	$R \sim$ 1200

5200 - 9200 Å respectively. The spectrum extraction procedure is discribed below.

At first, the raw image files are converted to `*.fits` file for easy operation. Then the images are cropped a bit in both dimensions to remove the geometrical distortion, using task IMCOPY.

Bias-subtraction: The bias frames (zero second exposure), taken with the shutter of the CCD closed, consists of only CCD readout. Thus pixel to pixel information about the noise level due to the CCD electronics are obtained from the bias frames. Using task ZEROCOMBINE, a number of bias frames (3 - 4 bias frames are sufficiant for significant sampling of the electronics noise) are median combined to obtain a master-bias. This master-bias is then subtracted from all the raw images using task IMARITH to remove the offset noise.

Cosmic-ray correction: Cosmic rays are removed from the bias subtracted

frames using task LACOS_SPEC. The bad-pixels are also removed from the file by this task. Now the frames are ready for further processing.

Aperture selection & extraction of spectrum: The one dimensional spectra are extracted using the optimal extraction method in APALL task by selecting the correct apertures and backgrounds. This task eliminates the sky noise, delivers maximum possible signal-to-noise ratio and takes care of the effects of moderate geometric distortion. The extracted one dimensional spectrum is in the form of number of counts versus pixel number.

Wavelength calibration: In order to calibrate the pixel number in terms of wavelength, spectra of laboratory standard sources (Iron-Argon (FeAr) for Grism# 7, Iron-Neon (FeNe) for Grism# 8 arc lamps) are taken, where the spectral emission features are known. The tasks IDENTIFY and REFSPECTRA are applied to these extracted spectra for wavelength calibration. Dispersion correction is done using DISPCOR task.

Flux-calibration: The flux calibration is done using the sensitivity function, calculated from the spectroscopic data of standard stars (Feige 34, O type subdwarf; Feige 110, OB type subdwarf etc.), observed on same night. The tasks involed are STANDARD that uses magnitude of standard star and atmospheric extinction, and SENSFUNC which fit a polynomial to the observed magnitude as a function of wavelength.

Combinig spectra: The extracted one-dimensional spectra for Grism#7 & Grism#8 are then combined using the task SCOMBINE by matching the common region be-

tween them to get the full optical range spectrum.

Reddening correction: These spectra are then dereddened for their inter-stellar extinction correction using the task DEREDDEN by giving the $E(B-V)$ or $A(V)$ values.

Converting to ASCI: Finally, task WSPECTEXT is used to convert the wavelength and flux calibrated spectrum into *.dat files.

NIR data reduction procedure:

TIRSPEC data analysis pipeline (Ninan et al. 2014) is used for NIR medium resolution ($R \sim 1200$, Y band (1.02 - 1.20 μm), J band (1.21 - 1.48 μm), H band (1.49 - 1.78 μm), K band (2.04 - 2.35 μm)) spectroscopy. During the data reduction procedure, flat-field correction, apperture selection, wavelength calibration are done to extract the one-dimensional spectra. For NIR observations, spectra are taken at two dithered positions and they are subtracted to remove the background sky. Spectrum of an argon lamp is also taken immediately after taking the object spectrum for wavelength calibration. For telluric line correction, spectrum of a bright spectroscopic NIR standard star is taken within the nearby airmass immediately before or after the target observation.

Using the pipeline, the spectra are then traced, one-dimensionally extracted, and automatically wavelength calibrated by using the Argon arc-lamp reading. This part is done in interactive mode to identify the good frames. After the wavelength calibration, Telluric Correction Tool, a fully interactive graphical software, is used to remove the telluric absorption lines from the spectra. The spectra of NIR standard stars are used to remove the telluric lines. This step also removes the instrument response by applying

a black body temperature correction and outputs a continuum-corrected spectrum. Also the fringes generated in the K-band spectra due to the detector array used in TIRSPEC, are removed in this step. Finally, the flux-calibrated spectrum is obtained by scaling this continuum-corrected spectrum to the magnitude of the source star.

All the spectra are then dereddened for the inter-stellar extinction correction and are used for analysis and modelling.

2.1.3 Observations of optical spectra of RS Oph (2006 outburst)

During the 2006 outburst of recurrent nova RS Oph, observations were taken earlier through 2m HCT and 2.3m Vainu Bappu Telescope (VBT), Kavalur, operated by IIA, Bangalore, India, by G. C. Anupama & U. S. Kamath (Mondal et al. 2018). The observations began on 2006 February 13, one day after the outburst discovery and continued well after the nova had reached quiescence (14 months). Low resolution optical spectra were obtained using the HCT and occasionally with the VBT, while high resolution (R$\sim$ 30,000) spectra were obtained with the VBT in the immediate post-maximum phase (14 and 19 February 2006). The HCT spectra were obtained using the HFOSC through Grism #7 ($R \sim 1500$) and Grism #8 ($R \sim 2200$), covering the wavelength ranges of 3400-8000 Å and 5200-9200 Å respectively. The high resolution VBT spectra were obtained covering the wavelength ranges of 4000 - 8000 Å using the fiber-fed Echelle spectrograph. Table 2.3 gives the dates of observations. We adopt the date of maximum as 2006 February 12.83 (JD 2453779.330).

All spectra were reduced using various tasks under the IRAF package following the standard procedure. The VBT Echelle spectra were wavelength calibrated using

Table 2.2: Observational Log of HCT.

Date	Object name	V Magnitude	Exposer time(s)	Wavelength region
April 28, 2015	T CrB	10	360	Optical & NIR
	V5668 Sgr	10	5	Optical & NIR
May 25, 2015	RS Oph	12	900	Optical & NIR
June 24, 2015	V5668 Sgr	10	5	Optical & NIR
July 23-24, 2015	RS Oph	12	900	Optical & NIR
	CI Aql	18	3600	Optical
	V5668 Sgr	10	5	Optical & NIR
	N Cep 2013	16	2700	Optical & NIR
August 24, 2015	V458 Vul	12	600	Optical & NIR
	N Cep 2014	16	2700	Optical
October 22 2015	KT Eri	15.5	1800	Optical & NIR
November 4, 2015	KT Eri	15.5	1800	Optica & NIR
December 30, 2015	T Pyx	14.5	2700	Optical
January 31, 2016	GK Per	13.5	1800	Optical
	T Pyx	14.5	2700	Optical
	RS Oph	12	900	Optical & NIR
March 17, 2016	T CrB	10	360	Optical & NIR
April 28-29, 2016	T CrB	10	360	Optical & NIR
	U Sco	17	1800	Optical
	RS Oph	12	900	Optical & NIR
May 13, 2016	BX Mon	12	480	Optical
	T CrB	10	360	Optical & NIR
	U Sco	17	1800	Optical
	V3890 Sgr	16	2700	Optical
June 9, 2016	BX Mon	12	480	Optical
August 6, 2016	V5668 Sgr	10	5	Optical
September 5, 2016	T CrB	10	360	Optical & NIR
	V339 Del	16	3600	Optical
	GK Per	13.5	1800	Optical & NIR
November 1, 2016	BX Mon	12	480	Optical & NIR
	V339 Del	16	3600	Optical
	N Cep 2014	16	2700	Optical
	KT Eri	15.5	1800	Optical
December 31, 2016	BX Mon	12	480	Optical & NIR
	GK Per	13.5	1800	Optical & NIR
	T CrB	10	360	Optical & NIR

Table 2.3: Journal of observations of RS Oph during 2006 outbursts.

Date	Telescope	Instrument
13 Feb, 2006	HCT	HFOSC
14 Feb, 2006	VBT	Echelle
15 Feb, 2006	HCT	HFOSC
16 Feb, 2006	HCT	HFOSC
17 Feb, 2006	HCT	HFOSC
18 Feb, 2006	HCT	HFOSC
19 Feb, 2006	VBT	Echelle
20 Feb, 2006	HCT	HFOSC
21 Feb, 2006	HCT	HFOSC
24 Feb, 2006	HCT	HFOSC
26 Feb, 2006	HCT	HFOSC
27 Feb, 2006	HCT	HFOSC
28 Feb, 2006	HCT	HFOSC
2 Mar, 2006	HCT	HFOSC
10 Mar, 2006	HCT	HFOSC
12 Mar, 2006	HCT	HFOSC
14 Mar, 2006	HCT	HFOSC
16 Mar, 2006	HCT	HFOSC
21 Mar, 2006	HCT	HFOSC
24 Mar, 2006	HCT	HFOSC
1 Apr, 2006	HCT	HFOSC
3 Apr, 2006	HCT	HFOSC
24 Apr, 2006	HCT	HFOSC
26 Apr, 2006	HCT	HFOSC
3 May, 2006	HCT	HFOSC
26 May, 2006	HCT	HFOSC
1 Jun, 2006	HCT	HFOSC
1 Jul, 2006	HCT	HFOSC
4 Jul, 2006	HCT	HFOSC
19 Jul, 2006	HCT	HFOSC
18 Aug, 2006	HCT	HFOSC
17 Oct, 2006	HCT	HFOSC
26 April, 2007	HCT	HFOSC

Table 2.4: A log of the published spectroscopic data used for the study.

Object	Wavelength band	Date of observation	Date of outburst	Observatory/Telescope/ Instrument	Resolution	References
RS Oph	Optical	March 15, 2006	February 12.83, 2006[1]	Observatorio Astrónomico Nacional en San Pedro Mártir/ Boller & Chivens	$\sim$ 1000 - 3500	a
	NIR	March 16, 2006		Mt. Abu Telescope/ NICMOS	$\sim$ 1000	b
RS Oph	Optical	April 4, 2006		Astrophysical Observatory of Asiago/ Boller & Chivens	$\sim$ 1000	c
	NIR	April 2, 2006		Mt. Abu Telescope/ NICMOS	$\sim$ 1000	b
V3890 Sgr	Optical	March 21, 1998	April 27.72, 1990[2]	Vainu Bappu Observatory/ JBT/UAGS	$\sim$ 10 - 12 Å	d
V745 Sco	Optical	March 20, 1998	July 30.08, 1989[3]	Vainu Bappu Observatory/ JBT/UAGS	$\sim$ 10 - 12 Å	d

1 = Hirosawa 2006; 2 = Kilmartin & Gilmore 1990; 3 = Liller 1989;
a = Riberio et al. 2009; b = Das et al. 2006 & Banerjee et al. 2009; c = Iijima 2009; d = Anupama & Mikolajewska 1999.

the ThAr source.

I thank the HCT Time Allocation Committee (HTAC) for a generous allocation of ToO time. I also thank all the observers of both the HCT and the VBT, who spared part of their observing time for the nova observations, without which the dense monitoring during the early phases of the outburst would not have been possible.

2.1.4 Published Data

Besides observational data, I have also used the published optical and NIR spectroscopic data. The optical spectroscopic data were taken by Riberio et al. (2009) at Observatorio Astrónomico Nacional en San Pedro Mártir and Astrophysical Observatory of Boller & Chivens on 32^{nd} day after outburst and by Iijima (2009) at Astrophysical Observatory of Asiago and Astrophysical Observatory of Boller & Chivens on 50^{th} day after outburst. The NIR JHK spectroscopic data were taken by Das et al. (2006) & Banerjee et al. (2009) at Mt. Abu Telescope - NICMOS (Near-Infrared Camera and Multi-Object Spectrometer) instrument, on 31^{st} and 49^{th} days after ourburst. In addition to these, I have also used published spectroscopic data of two other recurrent novae, V3890 Sgr and V745 Sco (Anupama & Mikolajewska 1999). These data (CCD spectra) were obtained from the Vainu Bappu Observatory (VBO), IIA, using the 1.02m and 2.3m telescopes. A journal of these data is shown in Table 2.4.

2.2 Photoionization model

A good estimation of elemental abundance, density structure etc. of the ejecta, and the temperature and luminosity of the central source can be obtained using the photoionization method. As the nova evolves, evolution of the abundance and other physical

characteristics can be assessed through modelling of spectra. I am using CLOUDY photoionization code, versions c13.04 and c17.00 rc1 (Ferland et al. 2013, 2017) to model the observed emission line spectra of novae.

CLOUDY computes the ionization, thermal, and chemical state of a non-equilibrium spherically expanding ejecta illuminated by a central source using a set of input parameters and predicts the resulting spectra. The calculations take into account the effects of important ionization processes, e.g., photo, Auger, collisional & charge transfer and recombination process *viz.*, radiative, dielectronic, three-body recombination, and charge transfer. The basic assumption is that all processes are in steady state, so for each ion species, rate of creation is equal to the rate of destruction. The input parameters incorporate the shape and brightness of the radiation field striking the cloud, hydrogen density and composition of the gas and the thickness (defined by inner (R_{in}) and outer (R_{out}) radius), covering factor (fraction of 4π sr enclosed by the model shell) and filling factor (the fraction of the volume that contains gas) of the cloud. The shell density $n(r)$ which is set by hydrogen density, and filling factor $f(r)$ may vary with the radius as given by the following relations,

$$n(r) = n(r_0)(r/r_0)^{\alpha} cm^{-3} \qquad \& \qquad f(r) = f(r_0)(r/r_0)^{\beta}, \tag{2.1}$$

where r_0 is the inner radius, α and β are exponents of power laws. By taking α = -3, I have considered a constant mass per unit volume throughout the model shell which is a standard practice for modelling atmosphere analysis of novae (Satrrfield et al. 1992; Hauschildt et al. 1997). For novae photospheres, the value of this exponent can only be -2 or -3. A constant mass loss rate and a constant velocity for the ejecta gives rise to a value of -2. However, if a constant mass loss rate together with a velocity proportional to the radius from the source is assumed, this gives rise to a value of -3 for

the exponent, and I use this value in all the models calculated during outbursts phase. While modelling the quiescence phase spectra, I consider a thick cylinder accretion disk around the central WD, and for a constant mass per unit volume throughout the model shell gives the value of α = - 2. I have chosen the filling factor = 0.3 - 0.1 depending on the days after outburst. Initially the shell is very dense and almost filled with gas but as the shell expands the filing factor starts to decrese as well. I have kept the filling factor power-law exponent, $(\beta) = 0$, which is the typical value used in other CLOUDY studies (e.g., Schwarz 2002; Vanlandingham et al. 2005; Helton et al. 2010).

The model generated spectra are then compared with the observed one and the goodness of fit is determined by the χ^2 and reduced χ^2 (χ^2_{red}) of the model,

$$\chi^2 = \sum_{i=1}^{n} (M_i - O_i)^2/\sigma_i^2, \quad \& \quad \chi^2_{red} = \chi^2/\nu, \tag{2.2}$$

where n = number of observed lines, n_p = number of free parameters, ν = degree of freedom = $n - n_p$, M_i = the modelled ratio of line flux to hydrogen line flux, O_i = measured flux ratio, and σ_i = error in the observed flux ratio. Error is considered in the range of $10 - 30\%$, depending upon the intensity of a spectral line, possibility of blending with adjacent lines, and error in the measuring line fluxes. For a good fit, value of $\chi^2 \sim \nu$ and value of χ^2_{red} should be low (typically, $1 < \chi^2_{red} < 2$).

From the best-fit spectra, the following parameters can be estimated:

- **Physical Parameters:** Initially, a large number of parameter values are used for experimentation to guess the tentative values of the parameters that fit the observed spectra. Temperature and luminosity values effect the continuum, whereas H-density changes the fluxes of H line ratios. Again higher temperatue and lumi-

nosity generate the higher ionization lines. By fixing the temperature and luminosity obtained by matching the continuum with the observed one, value of H-density was estimated from the H line ratios. Finally, by χ^2 minimization technique, best-fit parameter values are estimated.

- **Elemetal Abundances:** After adjusting the basic parameter values, abundances of each element can be estimated from the emission lines of those elements other than H, present in the observed spectra. By varying the elemental abundances from subsolar to higher values, the observed and modelled line fluxes are matched; and from the best fit, elemental abundances are determined. In this study, the results of elemental abundances vary from 0.4 to 12.0 for different elements. Changing metallicity also changes the elemental abundances overall for all the elements present in the ejecta.

- **Ejected Mass:** Mass of the ejected gas can be calculated from the estimated H-density value. Mass of hydrogen in each shell can be added up and multiplied by the covering factor (f) to estimate the total ejected mass of hydrogen in the nova ejecta (Schwarz et al. 2001; Schwarz 2002). The equation for ejected mass is as follows:

$$M_{ej} = f \times n(r_0) f(r_0) \int_{R_{in}}^{R_{out}} (r/r_0)^{\alpha+\beta} 4\pi r^2 dr, \tag{2.3}$$

where R_{in}, R_{out} are the inner and outer radii of the ejecta, α & β are exponents of power laws, $n(r_0)$ is the hydrogen density at the inner radius and $f(r_0)$ is filling factor at the inner radius. Using this formula I have calculated the ejected mass for RS Oph (details in Chapter 3) which match well with the previously determined results.

In this way, a large number of parameter values (observables) can be obtained from the output of CLOUDY providing only a few input parameters.

Chapter 3

Study of the Recurrent Nova RS Ophiuchi

RS Ophiuchi (RS Oph) is a well-observed recurrent nova (recurrence period $\sim$ 20 years) and is one of the ten confirmed recurrent novae that belong to our galaxy (Kato & Hachisu 2012; Schaefer 2010). RS Oph system is composed of a massive ($\sim 1.35 M_{\odot}$, Kato et al. 2008) white dwarf (WD) primary accompanied by a red giant secondary of estimated spectral class around M2 III (Worters et al. 2007 and references therein). Brandi et al. (2009) estimated orbital period of 453.6 days, the red giant mass, $M_g = 0.68 - 0.80 M_{\odot}$ and the orbital inclination, $i = 49^{\circ} - 52^{\circ}$ for the system. The outburst occurs due to thermonuclear runaway (TNR), on the WD surface that accretes matter from the secondary red giant companion. The outburst causes ejection of mass $\sim 10^{-6} - 10^{-8} M_{\odot}$ at high speed of $\sim$ 4000 km s^{-1} (Buil 2006). Previous studies of outbursts indicate that the WD mass of RS Oph is possibly increasing due to accumulation of a percentage of accreted matter on its surface. Consequently, the mass of the WD in RS Oph may gradually reach the Chandrasekhar limit and explode as a Type Ia supernova - this has made RS Oph an object of immense significance to the astrophysicists. However, there has been considerable debates on this hypothesis (Starrfield et al. 2004; Wood-Vasey & Sokoloski 2006).

RS Oph was detected in outburst previously in 1898, 1933, 1958, 1967, 1985; its latest

outburst was discovered on 2006 February 12.83 UT (Narumi et al., 2006). The reason for much shorter recurrence period in RS Oph system, in comparison to classical novae (CNe), is due to combined effect of the high WD mass and a high accretion rate (Starfield et al. 1985; Yaron et al. 2005). The recent outburst of RS Oph in 2006 offered a great chance for multiwavelength observations, and has been studied in detail at several wavelength regimes; e.g., in X-rays (Bode et al. 2006; Sokoloski et al. 2006), in the optical (Buil 2006; Fujii 2006; Iijima 2006a; Skopal et al. 2008), in the infrared (IR) (Das et al. 2006; Banerjee et al. 2009; Monnier et al. 2006; Evans et al. 2007a, 2007b) and in the radio (O' Brien et al. 2006; Kantharia et al. 2007; Rupen et al. 2008). The X-ray results clearly detect an X-ray blast wave that expands into the red giant wind. The temporal evolution of the shock wave was traced from XRT observations from the Swift satellite (Bode et al. 2006) and the Rossi X-ray Timing Explorer (RXTE) observations (Sokoloski et al. 2006). A similar shock has been detected from the evolution of the line widths in the near-IR spectra of the 2006 outburst (Das et al. 2006). The 2006 outburst also showed similarity with the previous outburst, with some differences, especially in the X-rays and radio.

The early phase spectra show broad, low-ionization emission features of H, He, N, O and Fe; the nova enters quickly (about a month after outburst) to the nebular phase with the emergence of strong coronal (e. g., [Fe XIV] 5303 Å, [Ar X] 5535 Å, [Fe X] 6374 Å, [Si VI] 1.9641 μm, [Al IX] 2.0444 μm, [Mn XIV] 2.0894 μm) and nebular lines (e.g., [O III] (4363, 4959 and 5007 Å) and [N II] 5755 Å) (Iijima 2009; Banerjee et al. 2009). The nova light curves also behave similarly; they decline fast with $t_2 \sim 6$ and $t_3 \sim 17$ days (Rosino 1987; Munari et al. 2007). The key result of the 1985 and 2006 observations was detection of shock that is generated while the ejecta interacts with the surrounding wind of the red giant secondary (Bode & Kahn 1985; Das et al. 2006 and references therein) and a non-spherical bi-polar shape of the nova ejecta (Taylor et al. 1989; Chesneau et al. 2007; Bode et al. 2007). From X-ray studies, Bode et

al. 2006 estimated a gas temperature $\sim 2.2 \times 10^8$ K for a shock velocity $v_s = 4000$ km s^{-1}. Further investigations also helped to determine few important parameters *viz.*, determinations of the distance, d = 1.6 ± 0.3 kpc, interstellar hydrogen column density, N $\sim 2.4 \times 10^{21}$ cm^{-2} (Hjellming et al. 1986), interstellar reddening of $E(B-V) = 0.73$ (Snijders 1987).

However, despite a plenty of observations of RS Oph, abundance analysis of the nova ejecta has been done sparsely only, for example, from optical studies Anupama & Prabhu (1989) derived helium abundance of $n(He)/n(H) = 0.16$; from fine-structure lines, Evans et al. (2007) estimated O/Ne ratio (by number) ~ 0.6. A complete knowledge of elemental abundances in the ejecta is of crucial importance for several reasons, for example, to understand the TNR process that leads to the nova explosion, the composition of material of the WD as there is a possibility of mixing of WD material with the ejecta, contribution of novae to the chemical evolution of galaxy etc.

For this study, I have used the observational data from the 2m Himalayan Chandra Telescope (HCT), Hanle, India and the 2.3m Vainu Bappu Telescope (VBT), Kavalur, India, as well as from published optical and NIR data. The evolution of the optical spectra of RS Oph during 14 months following the 2006 outburst are discussed in section 3.1 and the details of the published optical and NIR are discussed in section 3.2. I have used the photoionization code CLOUDY (version 13.02; Ferland et al. 2013) to generate spectra, by varying the parameter values. Model generated spectra are then compared with the observed emission line spectra, the best fit model is chosen by calculating the corresponding χ^2 values. The procedure of modelling is described in section 3.3 and results obtained from the analysis is described in section 3.4.

Table 3.1: Log of observations of RS Oph during 2006 outburst.

Date	Telescope	Instrument
13 Feb	HCT	HFOSC
14 Feb	VBT	Echelle
15 Feb	HCT	HFOSC
16 Feb	HCT	HFOSC
17 Feb	HCT	HFOSC
18 Feb	HCT	HFOSC
19 Feb	VBT	Echelle
20 Feb	HCT	HFOSC
21 Feb	HCT	HFOSC
24 Feb	HCT	HFOSC
26 Feb	HCT	HFOSC
27 Feb	HCT	HFOSC
28 Feb	HCT	HFOSC
2 Mar	HCT	HFOSC
10 Mar	HCT	HFOSC
12 Mar	HCT	HFOSC
14 Mar	HCT	HFOSC
16 Mar	HCT	HFOSC
21 Mar	HCT	HFOSC
24 Mar	HCT	HFOSC
1 Apr	HCT	HFOSC
3 Apr	HCT	HFOSC
24 Apr	HCT	HFOSC
26 Apr	HCT	HFOSC
3 May	HCT	HFOSC
26 May	HCT	HFOSC
1 Jun	HCT	HFOSC
1 Jul	HCT	HFOSC
4 Jul	HCT	HFOSC
19 Jul	HCT	HFOSC
18 Aug	HCT	HFOSC
17 Oct	HCT	HFOSC

3.1 Observational data

The observations of RS Oph during 2006 outburst were carried out earlier at low resolution using 2m HCT and at high resolution using 2.3m VBT (by G. C. Anupama & U. S. Kamath, Mondal et al. 2018). The log of observation is presented in Table 3.1. The details of the instruments and data reduction procedure have been discussed in section 2.1, Chapter 2.

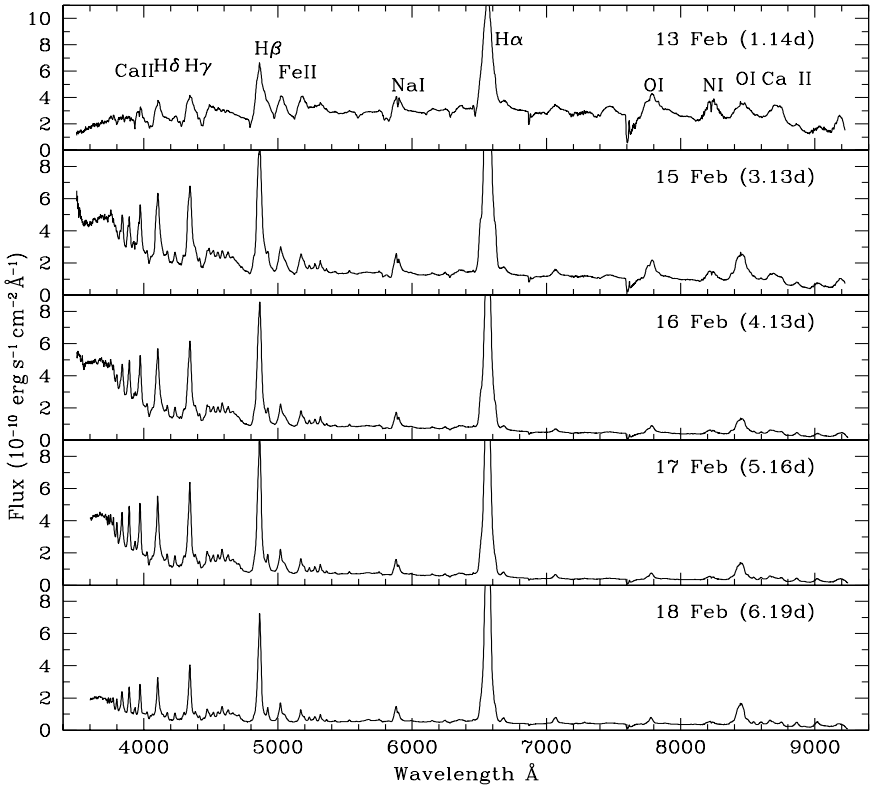

Figure 3.1: Optical spectra of RS Oph during 2006 February. The most prominent features are those due to H, Fe II and Ca II. Hα line has been truncated so that the weaker lines are seen properly.

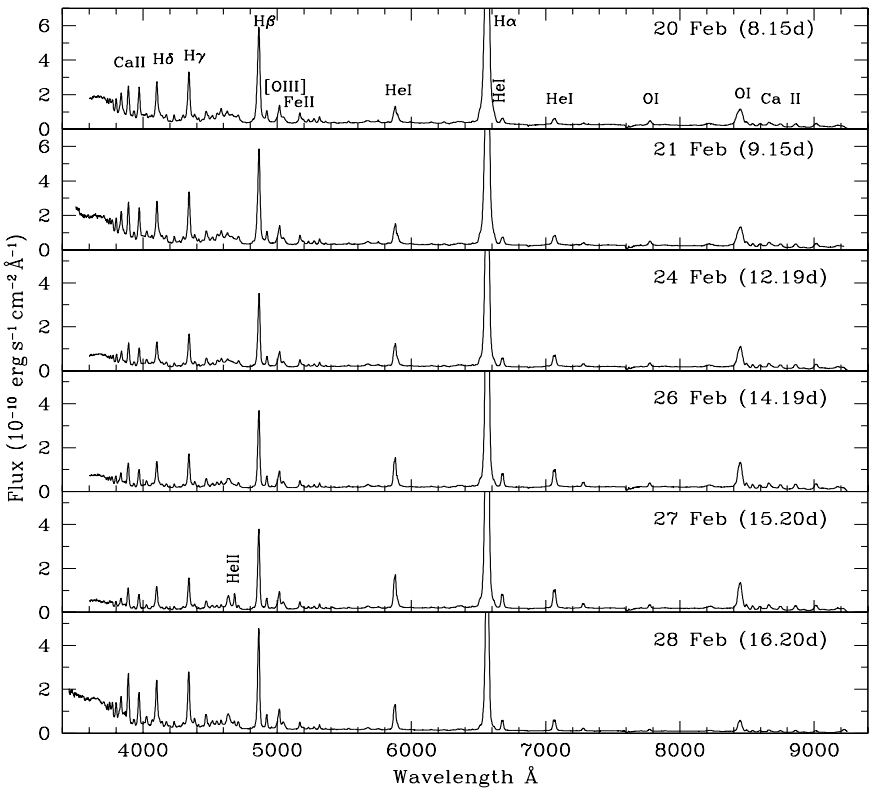

Figure 3.2: Optical spectra of RS Oph during 2006 February (continued). Note the emergence and strengthening of the He II 4684 Å line during days 8 - 15, and the sudden decline on day 16.

3.1.1 Evolution of the spectrum

The early phase : days 1 to 15

One day after the maximum, the spectrum is dominated by broad emission lines due to H, N, Ca II (IR), Na I and O I. Weak P Cygni absorption features are seen associated with the emission lines. The nova appears to be in the "fireball expansion" phase. About 5 days after maximum, P Cyg absorption features associated with the broad emission are absent and the emission line widths are narrower. The continuum appears bluer. The prominent lines are due to H and Fe II. [Ar X] 5535 Å line could be weakly present. The strength of O I 8446 Å line has increased while the strength of Ca II IR lines have decreased. [Fe X] 6374 Å begins to appear around day 8. Sharp [O III] 4959, 5007 Å,

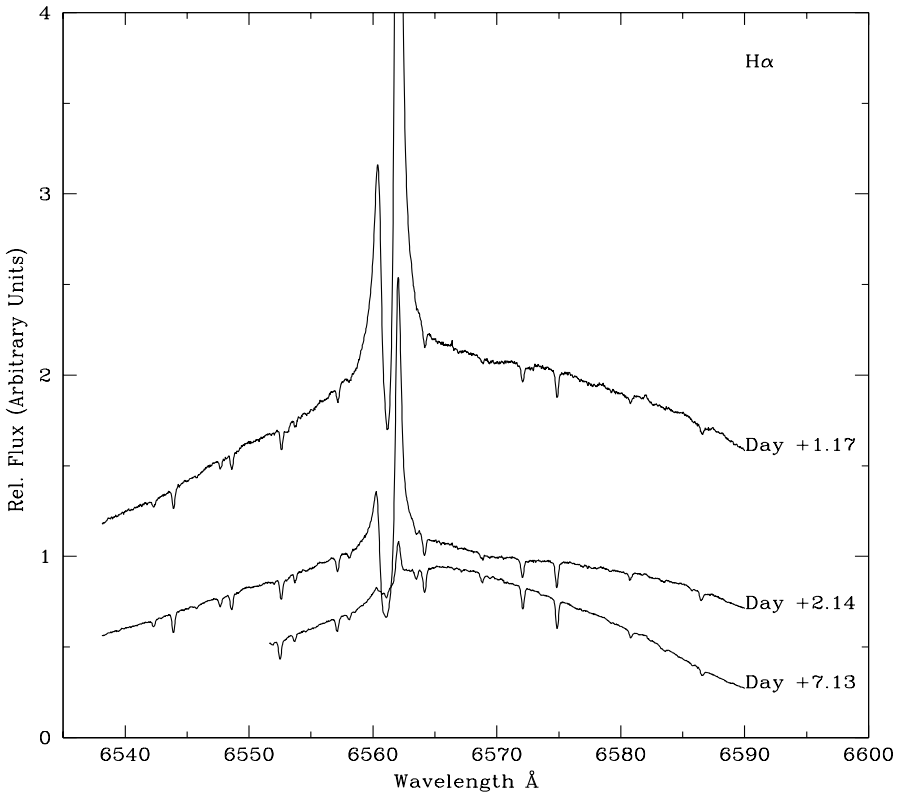

Figure 3.3: The Hα line in the high resolution spectra during days 1-7. The emission from the nova ejecta is broader than the wavelength covered by the order. The plot shows the narrow P Cygni component from the circumstellar material. Note the decrease in the strength of this component by day 7.

[N II] 5755 Å appear around day 15. [Fe XI] is probably present on day 15. These lines most probably arise from the ionised red giant wind. In the spectra of days 14-16, the He I lines show a double peaked profile. The spectra are shown in Fig. 3.1 and 3.2. RS Oph was detected in the 14 - 25 keV band of *Swift* XRT and in the 3 - 5 keV and 5 - 12 keV bands of the *RXTE* all sky monitor during $\sim 0-5$ days, with an increasing flux (Bode et al. 2006; Sokoloski et al. 2006). The presence of the coronal lines in the optical spectrum during the very early phase appears to be consistent with the hard X-ray detection. The increase in the blue continuum is also consistent with the increase in the X-ray flux.

The high resolution spectra of day 1 show sharp, narrow P Cygni emission features superimposed over the broad emission features (see Fig. 3.3). The P Cyg absorption, which originates in the circumstellar red giant wind indicates a velocity $\sim$ 20 km s^{-1}. The absorption decreased in strength around day 7, similar to the broad absorption component. The wind emission is dominated by Fe II emission lines. The spectra clearly show the Na ID interstellar absorption components as well as several diffuse interstellar bands between 5690 Å and 5870 Å, at 5705, 5778, 5780, 5797, 5844 and 5849 Å (Josafatsson & Snow 1987). Of these, the narrow bands at 5780, 5797 and 5849 Å are correlated with interstellar reddening. We have measured the equivalent width of the 5797 Å narrow band and calculated the avarage value as 0.109 ± 0.01 Å. Using that, an $E(B-V) = 0.75 \pm 0.05$ is estimated. This value was used to deredden the observed data.

The high excitation phase : days 16 to 80

This phase is marked by a decrease in the strength of the permitted lines, and the strengthening of high excitation lines. The Fe II lines fade, while the He I lines develop and strengthen with time, and by $\sim$ day 25, the spectrum is dominated by H and He (I & II) lines (Fig. 3.4). Also, O I 8446 Å becomes stronger than O I 7774 Å. The emer-

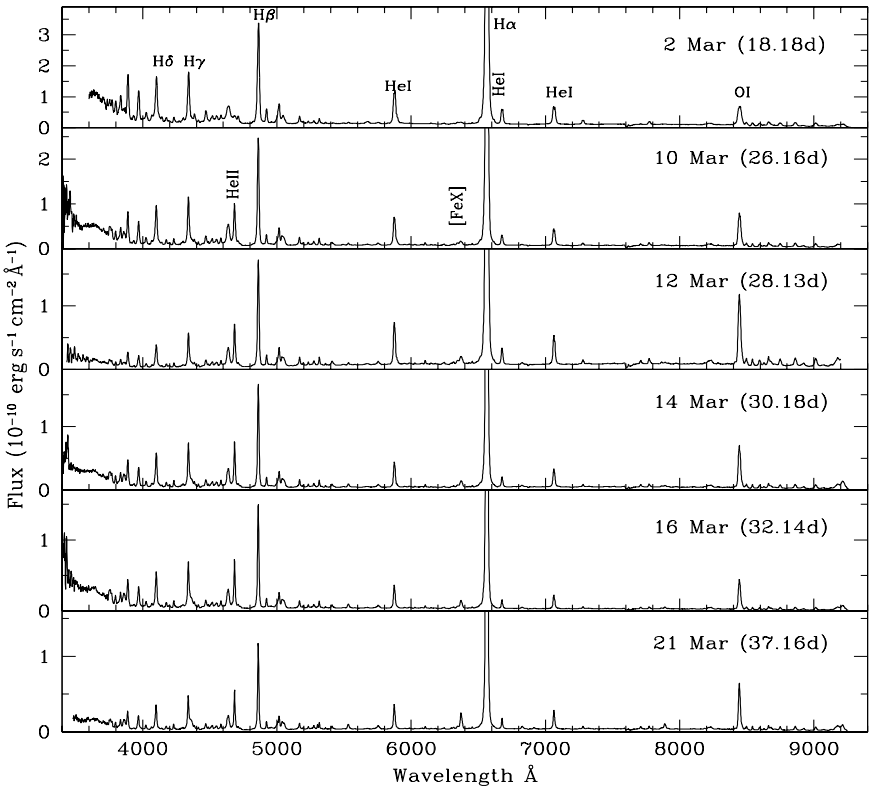

Figure 3.4: Optical spectra of RS Oph during 2006 March. Fe II lines have weakened, and the lines due to He have strengthened. Also note strengthening of coronal lines and OI 8446 Å.

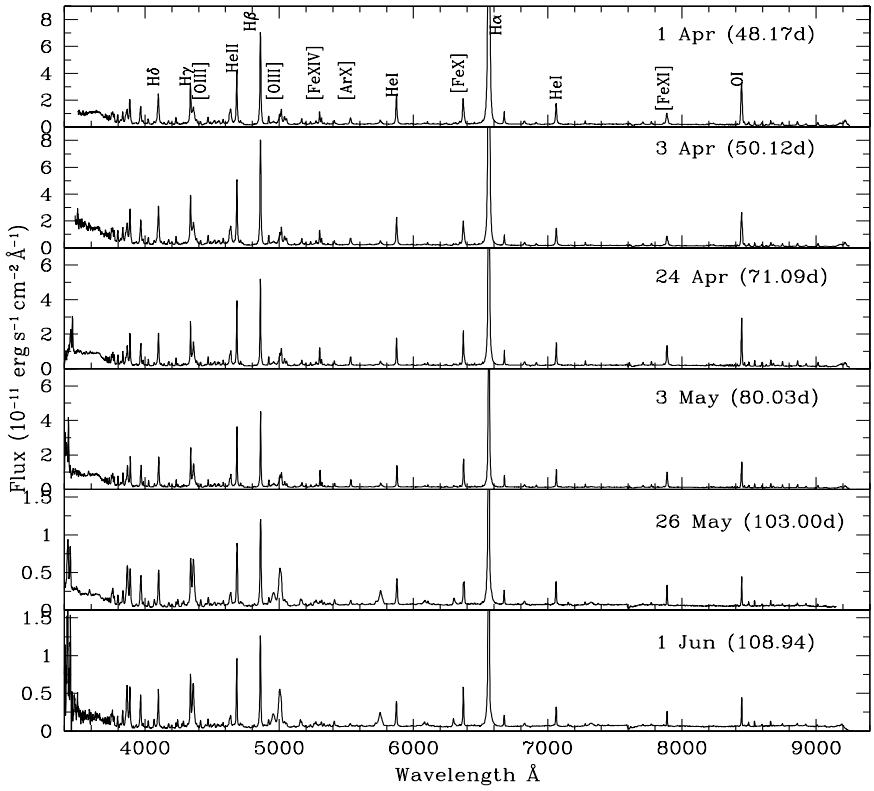

Figure 3.5: Optical spectra of RS Oph during 2006 April – June. The coronal and other high excitation lines are strong during this period.

gence of the He II lines is consistent with the onset of the supersoft X-ray phase (SSS phase) that commenced about 30 days since outburst (Osborne et al. 2011). Although a few coronal lines began developing as early as on day 8, the onset of the coronal phase appears to be around day 25, with all the coronal lines, due to [Fe X], [Fe XI] and [Fe XIV] strongly present, and strengthening with time. The coronal phase peaks around 60 - 70 days after maximum, similar to the previous outbursts (Anupama & Prabhu 1989).

The line profiles show multiple components (e.g., [O III] 4363 and 5007 Å lines, see Fig. 3.10 and Fig. 3.11) The width of the emission lines continues to decrease with time. About 70 days after the outburst, [O III] line width becomes similar to those of other lines, and the spectrum is dominated by Balmer, He II, coronal and other high excitation lines. O I 8446 Å shows a two component – a broad and a narrow component – structure. By day 80, the [O III] lines are strengthening, and the O I 8446 Å two component structure continues. The spectra are shown in Fig. 3.5.

The nebular phase : beyond day 100

The nebular phase began by day 100, and the nova was well into the nebular phase by $\sim$ 135 days. The nebular lines are broader compared to the recombination lines. Coronal lines have weakened in strength. Other nebular lines such as [Ca II] 7323 begin to appear. Fe II and N I lines are absent or very weak. The nebular lines get stronger between days 140–160 and are broader than other lines. Hα shows asymmetric broad wings, with a velocity similar to those of the nebular lines. Contribution from the giant secondary is seen by day 140, as indicated by the presence of TiO absorption bands. These spectra can be seen in Fig. 3.6.

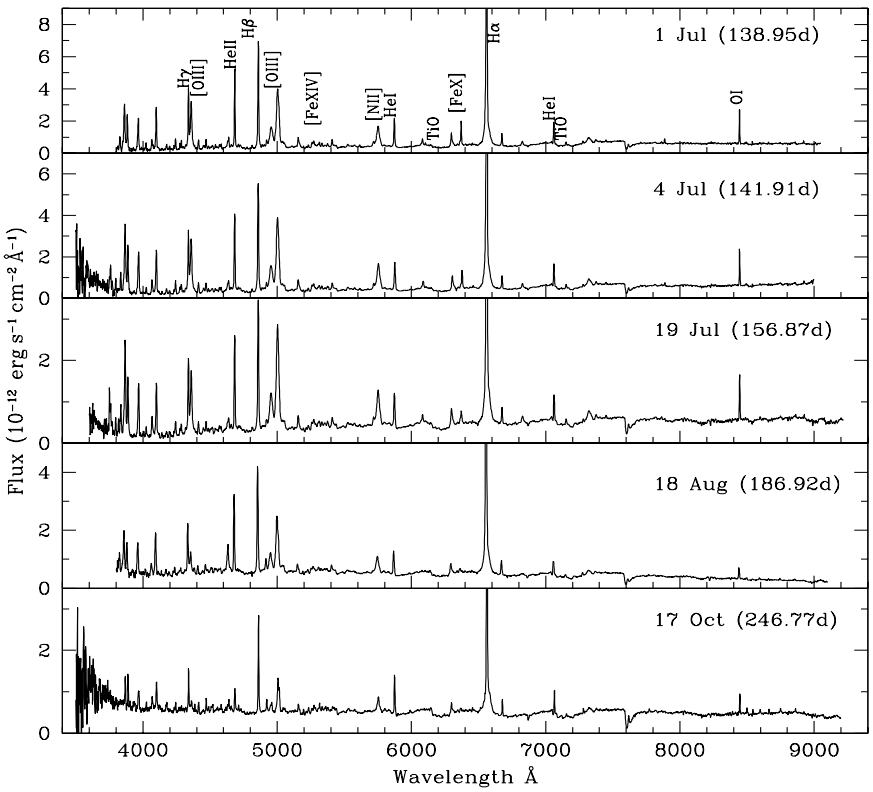

Figure 3.6: Spectra of RS Oph during 2006 July – October. The nova has reached the nebular phase during this period. TiO absorption features can be clearly seen.

3.1.2 Description of some emission lines

Emission line velocities

The emission line widths are found to narrow with time. The hydrogen Balmer lines indicate the following velocities: 4200 km s^{-1} (+1d); 3800 km s^{-1} (+3d); 2000 km s^{-1} (+5d); 1060 km s^{-1} (+18d); 740 km s^{-1} (+31d); 332 km s^{-1} (+70d). Fig. 3.7 shows the evolution of the emission line velocity. The velocities vary as $t^{-0.4}$ for $t < 5$ days and $t^{-0.66}$ during $t = 5 - 70$ days. This phenomenon is seen in the near-infrared lines as well and has been generally interpreted as free expansion of the shock front during the first four days and a deceleration phase thereafter (Das et al. 2006; Banerjee et al. 2009). These findings are also consistent with the X-ray observations (Bode et al. 2006; Sokoloski et al. 2006). A slight increase in the emission line width of the recombina-

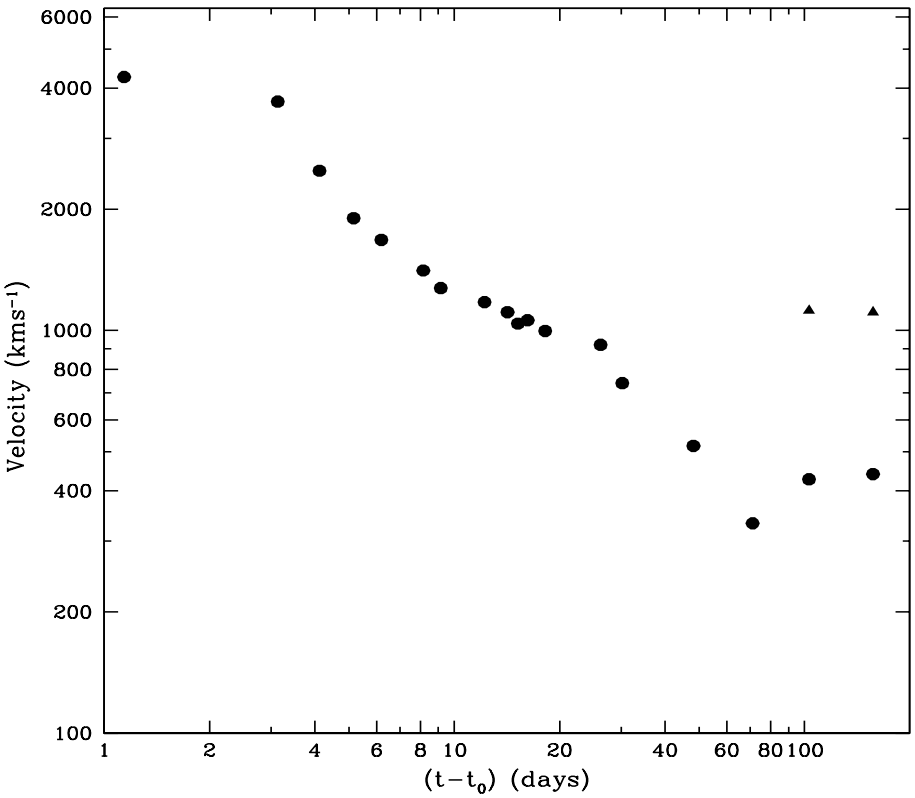

Figure 3.7: Velocities in the RS Oph spectra. It can be seen that the free expansion phase lasted only for $\sim$ 4 days. The sharp fall in velocity after that is due to the shock wave generated when the high-velocity nova ejecta interact with the slow-moving red-giant wind. Note the increase in the velocity after day 80.

tion lines is seen after day 80. The nebular lines are broader than recombination lines, with a velocity $v \sim 1500$ km s^{-1} compared to $v \sim 400$ km s^{-1} for the recombination lines.

Oxygen lines

The O I 8446 Å line is stronger than the 7774 Å line on all days implying that Lyβ fluorescence is the dominant excitation mechanism. The evolution of these two lines can be seen in Fig. 3.8 and 3.9. The [O I] 6300 Å and 6364 Å lines are best seen in spectra starting 2006 May. The O IV 6106 Å and 6182 Å lines are seen from 2006 March 10

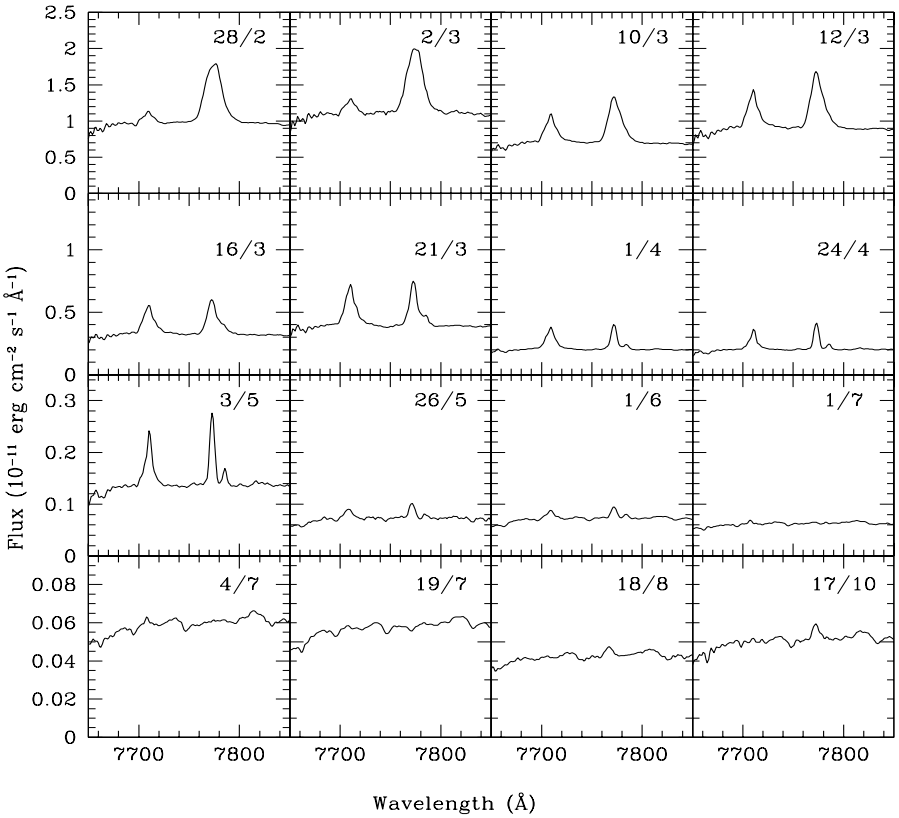

Figure 3.8: Evolution of the O I 7774 Å line. Dates are in the dd/mm format. The stronger line in the first panel (top left) is O I. On its left is the unidentified line at 7710 Å. The development of an unidentified line at 7785 Å can be seen (second panel from top). The O I line is seen to fade away in 2006 July, reappear in 2006 August and persist until 2006 October.

onwards and are clearly identifiable till 2006 July. There is a hint of the [O III] 4363 Å line in the spectra obtained from 2006 February 21 onwards. It is clearly seen on 2006 April 1. On 2006 May 26 it is seen to be as strong as Hγ. It faded thereafter but is seen till 2006 August 18. There is no sign of this line in the 2006 October 17 spectrum. The evolution of this line can be seen in Fig. 3.10. Similarly, there are indications of the [O III] 4959 Å and 5007 Å lines from 2006 February 20 onwards. These lines are clearly seen on 2006 April 1 and become extremely broad on 2006 May 26. They are very prominent on 2006 July 4 and gradually fade thereafter. The evolution of these lines can be seen in Fig. 3.11.

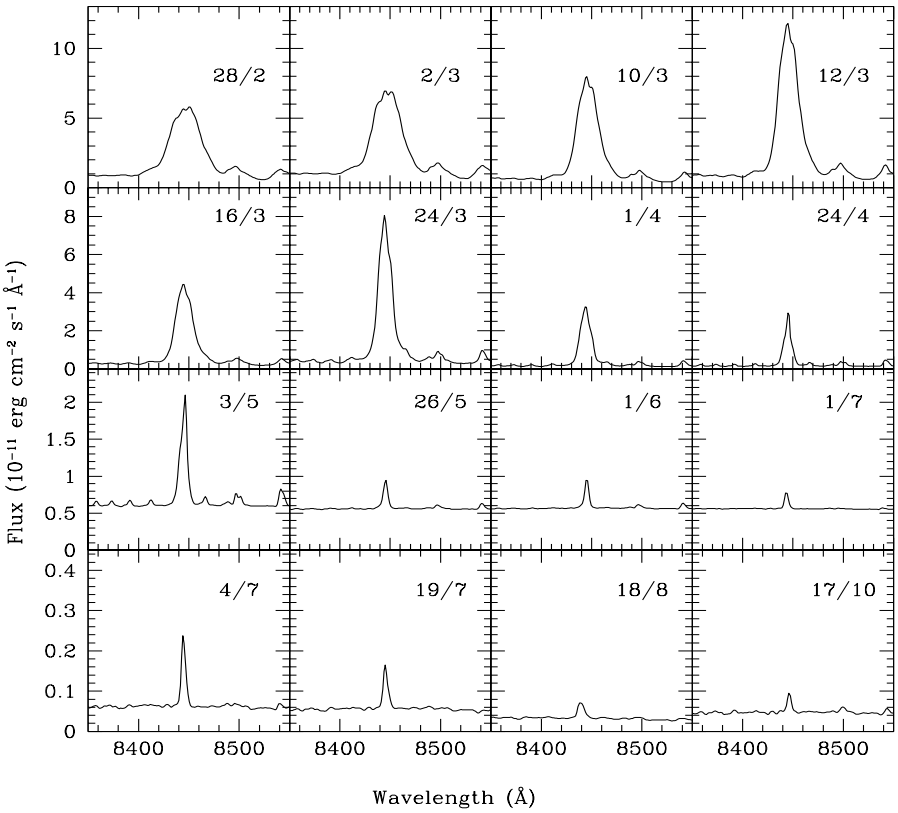

Figure 3.9: Evolution of the O I 8446 Å line. Dates are in the dd/mm format. The stronger line in all the panels is the O I line. Paschen lines can also be seen; they are narrow and clearly seen on 2006 May 3.

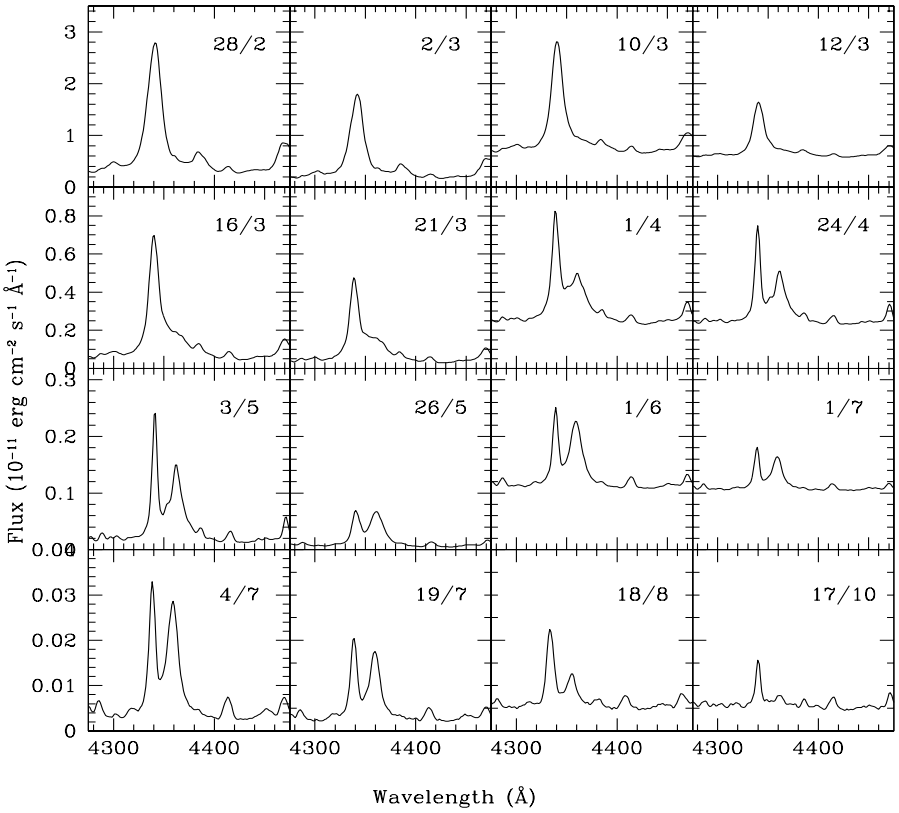

Figure 3.10: Evolution of the [O III] 4363 Å line (top to bottom, left to right). Dates are in the dd/mm format. Spectra in the last two columns in the first three rows have been scaled up for clarity. The strong line in the first panel (top left) is Hγ. The 4363 Å line starts affecting the blue wing of Hγ from 2006 March 16, and is clearly seen on 2006 April 1; it has almost disappeared by 2006 October 17.

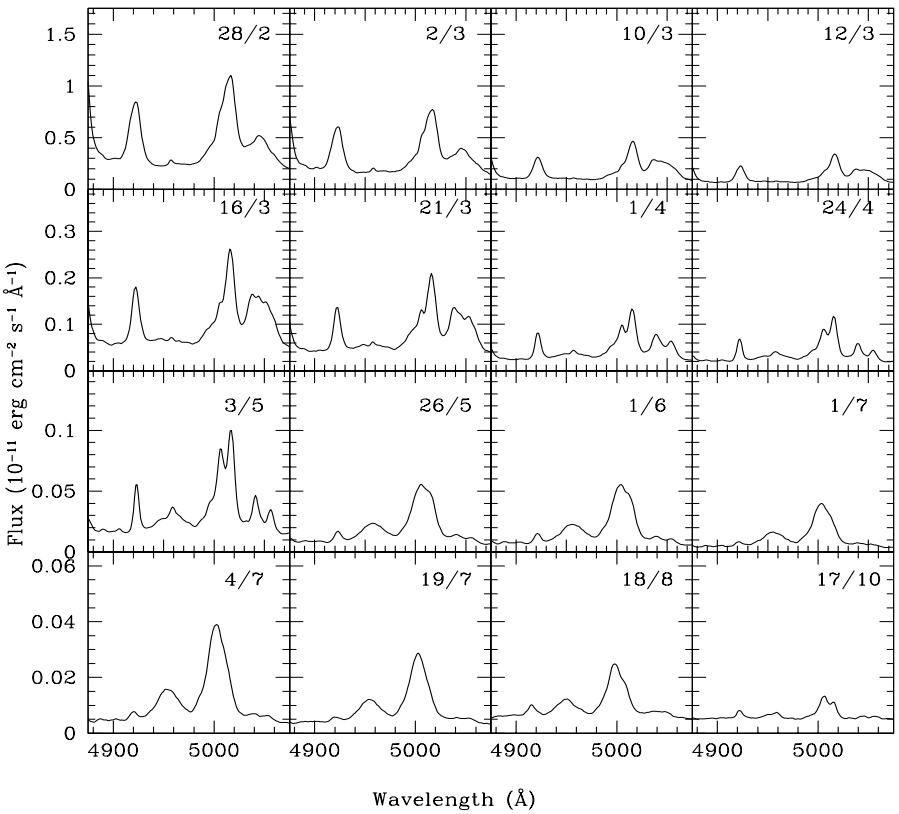

Figure 3.11: Evolution of the [O III] 4959 and 5007 Å lines. Dates are in the dd/mm format. Lines seen in the first panel (top left) belong to Fe II; lines belonging to other species at similar wavelengths strengthen with time. By 2006 March 16, He I (the first two lines) has strengthened; the third (broad) line is mostly Si II. The [O III] 5007 Å line can be seen feebly on the blueward side of the He I 5016 Å line. The [O III] 4959 Å and 5007 Å lines can be clearly seen in the spectrum obtained on 2006 May 3; they persist until 2006 October 17.

Helium lines

There is only a hint of the He I 4471 Å line on 2006 February 13; it shows up clearly two days later. The 5876 Å, line is very broad with a sharp central absorption on 2006 February 13. It has contributions from some other line on its redward side till 2006 April. On 2006 February 13, the 6678 Å line is very broad with a central absorption,

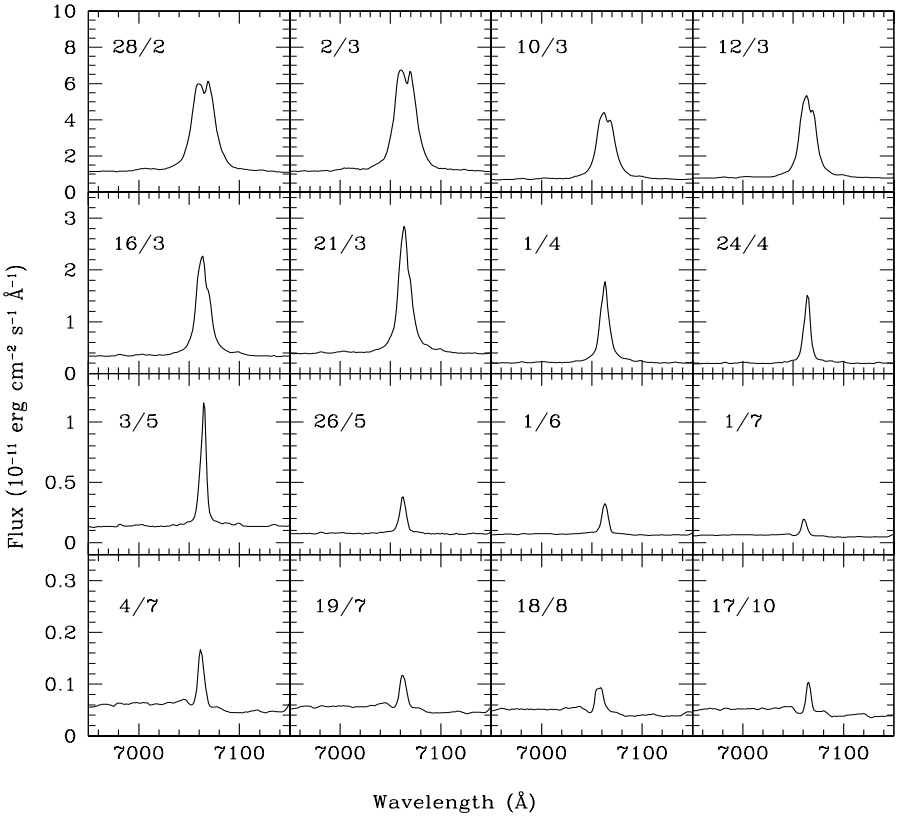

Figure 3.12: Evolution of the He I 7065 Å line. Dates are in the dd/mm format.

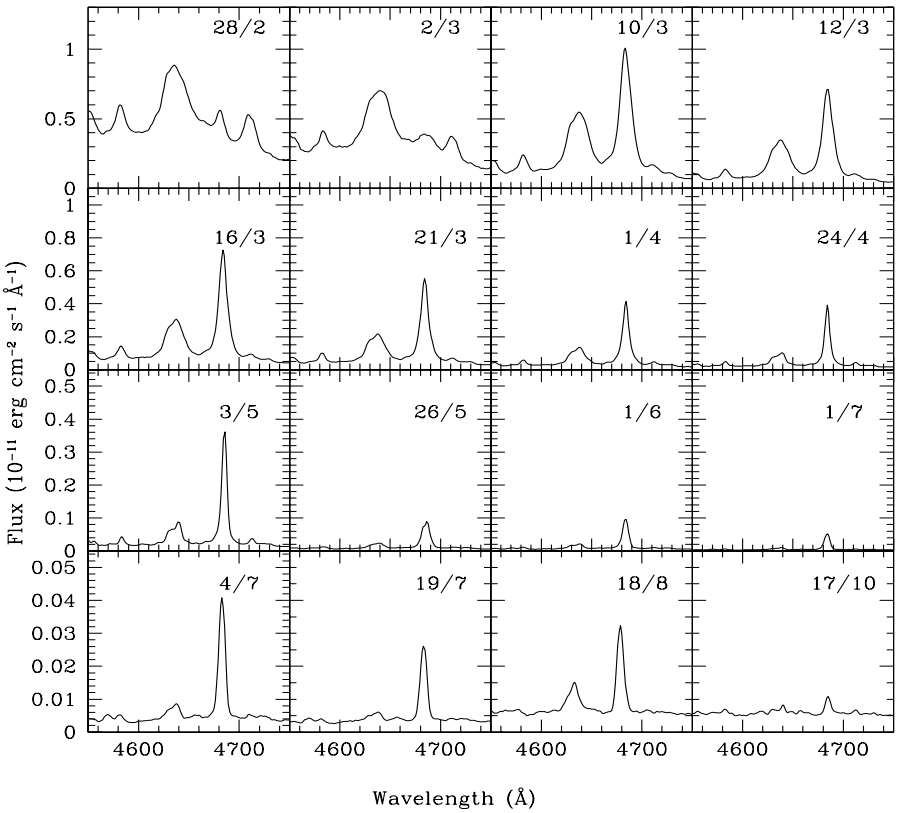

Figure 3.13: Evolution of the He II 4686 Å line. Dates are in the dd/mm format. Lines seen in the first panel (top left) belong to Fe II and N III (the strongest line). The strong, narrow He II line is clearly seen by 2006 March 10 and persists till 2006 October 17.

which persists until early 2006 March. The 7065 Å line shows a central absorption on 2006 February 13 which shifts to the redward side on subsequent days. By 2006 March 16, the line has a Gaussian-like appearance. All the He I lines persist until 2006 October 17; the 7065 Å line shows a P-Cygni profile from 2006 July onwards (see Fig.3.12). The He II 4686 Å line appears on 2006 February 27 with a narrower $FWHM$ (Full Width at Half Maxima) than Balmer lines; emission lines at this position in earlier spectra are likely to be contributions from Fe II. By 2006 March 10, its width is similar to Hβ. This line persists until 2006 October 17 (see Fig. 3.13).

Nitrogen lines

The [N II] 5755 Å line is present since 13 Feb. It is very broad initially but narrows down by 15 February. The 5660 Å appears on 16 February and is broad, blended with the 5680 Å feature. From 20 February onwards it has a narrow component on top of a broad feature. Other nitrogen lines show up after 26 February. The 5755 Å line has a triangular shape and is seen to narrow with time. It suddenly broadens on 26 May. This line persists until 2006 October 17 (See Fig. 3.14). The '4640' complex is observed from 2006 February to 2006 October (see Fig. 3.13).

Coronal lines

Coronal lines in RS Oph were first seen and identified by Adams & Joy (1933) on day 51 during the 1933 outburst. The presence of five coronal lines at 3987, 4086, 4231, 5303 and 6374 Å could be identified on their spectrograms obtained on later nights. In this outburst, coronal lines of neon ([Ne III], [Ne V]), argon ([Ar IV], [Ar X], [Ar XI], [Ar XIV]) and iron ([Fe VII], [Fe X], [Fe XI], [Fe XIV]) can be clearly seen in the spectra

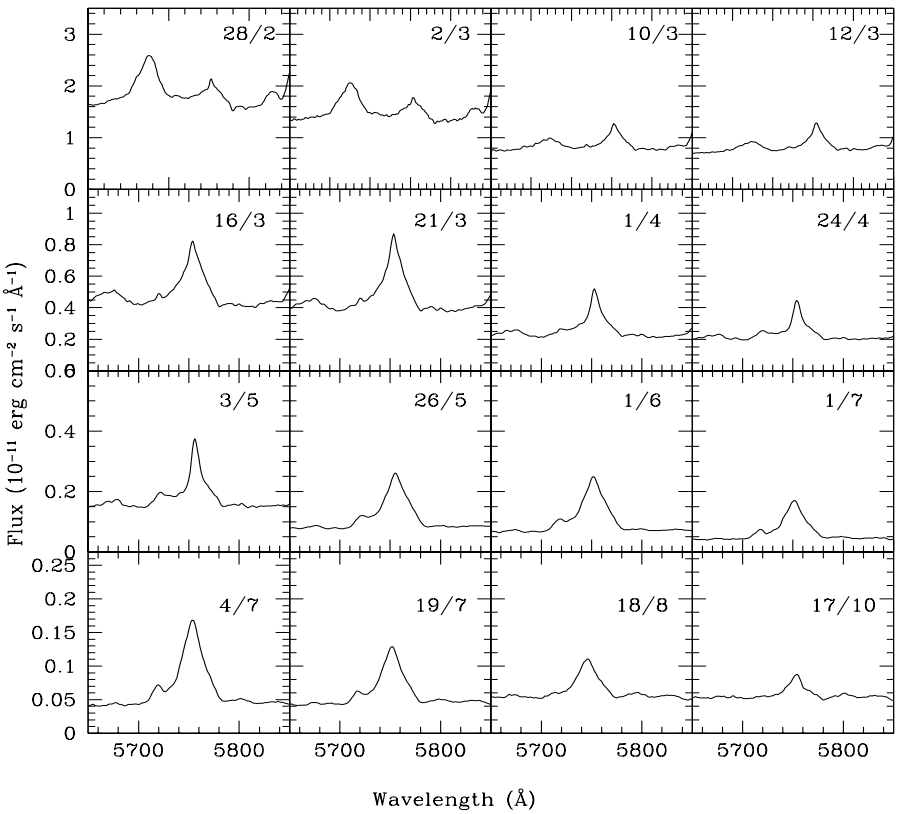

Figure 3.14: Evolution of the [N II] 5680 and 5755 Å lines. Dates are in the dd/mm format. Both the lines (5660 + 5680 Å blend and 5755 Å) are seen in the first panel. The 5660 / 5680 Å line weakens and is replaced by the [Fe VI] 5679 Å line in later spectra. The [Fe VII] 5721 Å line shows as a small kink on the redward side of 5755 Å on 2006 March 16, become stronger and fades away by 2006 August 18.

obtained during 2006 March – June. It appears that the calcium lines showed an unusual behaviour during this outburst as compared to the previous outbursts. [Ca XIII] 4086 Å was absent, [Ca XV] 5694 Å was not prominent. The temporal development of the iron green and red coronal lines are shown in Fig. 3.15 and 3.16 respectively. Many coronal lines are close in wavelength to other permitted or low ionisation lines – for example, [Ne III] 3970 Å and Hϵ, [Ni XII] 4231 Å and Fe II, [Ar XIV] 4412 Å and [Fe II], etc – and it becomes difficult to separate the contributions from the individual components from observations of emission lines. However, it is very likely that the permitted or low ionisation lines are the dominant contributors in the early outburst spectra.

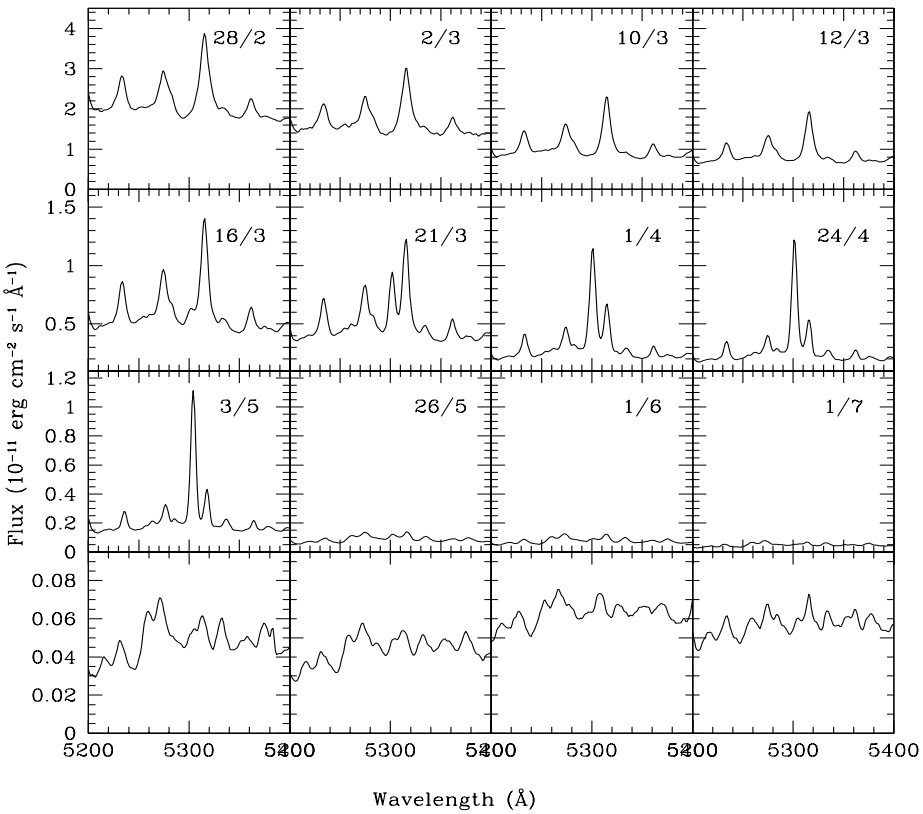

Figure 3.15: Evolution of the [Fe XIV] 5303 Å line. Dates are in the dd/mm format. Fe II lines are seen in the first panel (top left). The [Fe XIV] appears as a small kink on the redward side of the Fe II 5317 line on 2006 March 16, increasing in strength by 2006 May 3, and barely seen by 2006 June 1. The last row of spectra display just the fluctuations at the continuum level.

The Raman scattered 6830, 7088 Å lines

The strong line at 6830 Å which was first seen in the 1933 outburst was attributed to [Kr III] (Joy & Swings 1945). This line was seen in other outbursts also. We now know that this emission feature, seen in many symbiotic novae, is due to the Raman scattering of the O VI 1032 Å line by neutral hydrogen (Schmid 1989). Schmid also noted that in some symbiotic novae a fainter companion feature appears at 7088 Å. This is due

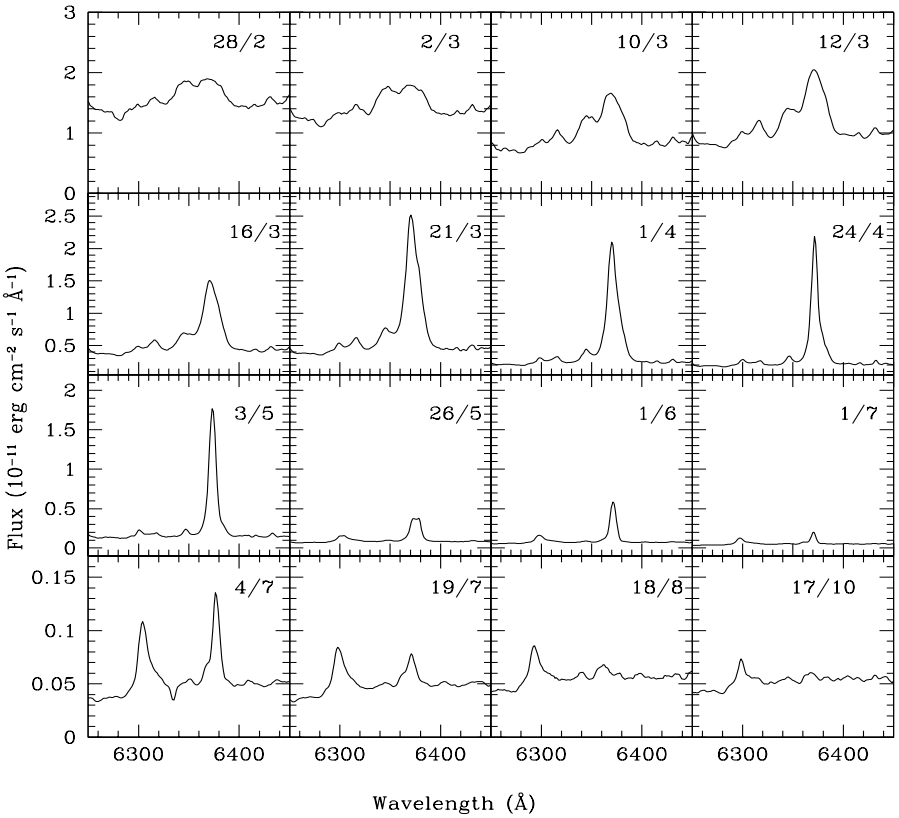

Figure 3.16: Evolution of the [Fe X] 6374 Å line. Dates are in the dd/mm format. The broad lines seen in the first panel (top left) are mostly Si II. The [Fe X] 6374 Å, [S III] + [K V] 6315 Å are seen on 2006 March 10. The [O I] 6300 Å line is also feebly seen on this day. By 2006 August 18, only the [O I] 6300 Å and 6363 Å lines are clearly seen.

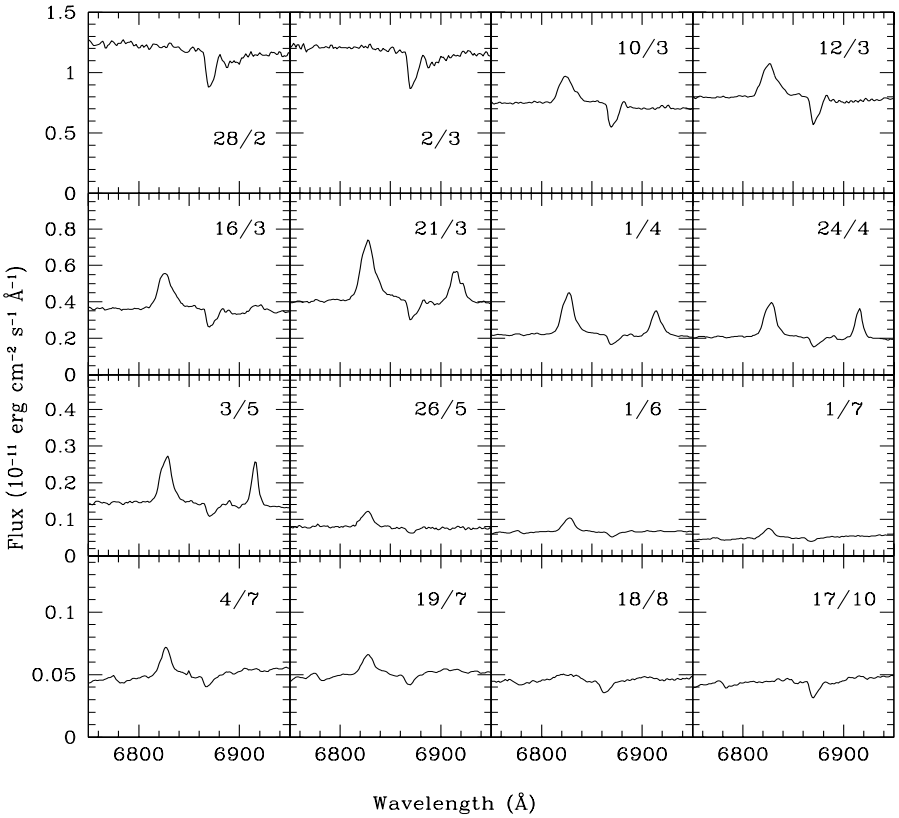

Figure 3.17: Evolution of the Raman scattered 6830 Å line. Dates are in the dd/mm format. This line appears suddenly on 2006 March 10; there is no gradual strengthening as seen for other lines. It disappears after 2006 July 19. The [Ar XI] 6919 Å line is seen during 2006 March 16 to 2006 May 3.

to the same process as for the 1038 Å line of the O VI resonance doublet. Schmid has suggested that this Raman scattering in symbiotic novae takes place in the atmosphere of the cool giant and in the inner parts of its stellar wind. The presence of the Raman scattered O VI lines implies the existence of a hot ionising source, the WD on which hydrogen is still burning after the outburst. The 2006 outburst is the first ouburst of RS Oph, since this identification was done. This line is first seen in the spectrum of 2006 March 10 and persists until 2006 August 18. In the next spectrum obtained on 2006 October 17, this line is probably not seen; other nearby lines dominate this wavelength region (see Fig. 3.17). The 7088 Å line is also feebly seen in the wings of He I 7065 Å during the same period.

Formation of the spectral lines

Swift observations have revealed the existence of a supersoft X-ray phase during days $26-90$ of the outburst which is due to slow burning of matter on the WD (Osborne et al. 2011). This source peaks at around day 50, similar to the behaviour of the coronal lines. This indicates that some of the fluxes in the coronal lines, especially during days $26-90$, must be due to photoionization. As mentioned above in 3.1.2, the behaviour of the Raman lines also corroborate this idea. The He II and O IV lines having high ionisation potentials also were strong during 2006 March – June. Similarly, multi-frequency radio data show that the spectral index is consistent with a mixed non-thermal and thermal emission during days $5-60$ (Eyres et al. 2009). Therefore, as for other novae, optical spectra should show the characteristics of photoionized ejecta. Photoionization could even be the dominant mechanism at least during days $29-90$.

3.2 Published Optical and NIR data

Besides observational data, I have also used the published optical and NIR spectroscopic data. The optical spectroscopic data were taken by Riberio et al. (2009) at Observatorio Astrónomico Nacional en San Pedro Mártir and Astrophysical Observatory of Boller & Chivens on 32^{nd} day after outburst and by Iijima (2009) at Astrophysical Observatory of Asiago and Astrophysical Observatory of Boller & Chivens on 50^{th} day after outburst. The NIR JHK spectroscopic data were taken by Das et al. (2006) & Banerjee et al. (2009) at Mt. Abu Telescope - NICMOS instrument, on 31^{st} and 49^{th} days after ourburst. The journal of data is shown in Table 3.2. Two epochs of observations have been that had nearly simultaneous optical and NIR spectra and form two data sets, represented by D31 and D49. Here, 'D' stands for days after outburst and the following numbers express the approximate number of days elapsed after outburst. D31 consists of optical and NIR spectra that is observed, respectively, on 2006 March 15 & March 16 i.e., approximately 31 days after outburst; whereas, D49 consists of optical and NIR spectra observed, respectively, on 2006 April 4 & April 2, i.e., approximately 49 days after outburst. I have marked the strong spectral lines on the figure (Fig. 3.18); a detailed observed line list is presented in Banerjee et al. (2009) and Iijima (2009). The spectra on D31 are dominated by prominent features of low ionization lines of Hϵ (3970 Å), Hδ (4103 Å), Hγ (4341 Å), He II (4686 Å), H β (4863 Å) in optical region; He I (1.0830 μm), Pa γ (1.0938 μm), O I (1.1287 μm), Pa β (1.2818 μm), Brackett series lines, Fe II (1.6872 μm), He I (1.7002 μm) in H-band; and He I (2.0581 μm), Br γ (2.1655 μm) in K-band. There are also higher ionization lines, *viz.*, [Fe VII] (3760 Å), blended feature of [O III], He I & Fe II (5017 Å), blended feature of [Fe II] & [Fe VII] (5158 Å), [Ar X] (5535 Å), [Fe X] (6374 Å) in optical; and [Si VI] (1.9641 μm), [Al IX] (2.0444 μm), [Mn XIV] (2.0894 μm) in NIR region.

Table 3.2: A log of the published spectroscopic data of RS Oph (2006) taken for study.

Epochs	Wavelength band	Date of observation	Days after outburst	Telescopes / Instruments	Resolution	References
D31	Optical	March 15	31	Observatorio Astrónomico Nacional en San Pedro Mártir/ Boller & Chivens	$\sim$ 1000 - 3500	a
	NIR	March 16	32	Mt. Abu Telescope/ NICMOS	$\sim$ 1000	b
D49	Optical	April 4	50	Astrophysical Observatory of Asiago/ Boller & Chivens	$\sim$ 1000	c
	NIR	April 2	49	Mt. Abu Telescope/ NICMOS	$\sim$ 1000	b

a = Riberio et al. 2009; b = Das et al. 2006 & Banerjee et al. 2009; c = Iijima 2009.

3.3 Modelling Procedure

I have modelled these optical and NIR JHK spectra of the 2006 outburst of RS Oph using photoionization code CLOUDY (version 13.02; Ferland et al. 2013, discussed in detail in Chapter 2). Modelling of both optical and NIR data enables to sample over a broader range of ionization and excitation levels in the emission lines and thus helps to constrain the results more accurately.

I assume a spherically symmetric expanding shell geometry of the ejecta that is illuminated by the central source. To minimize the number of free parameters, inner (R_{in}) and outer (R_{out}) radii (calculated from minimum (V_{min}) and maximum (V_{max}) expansion velocities, respectively) of the ejected shell are held constant during the iterative process of fitting the spectra. I have surveyed literature and adopt initial shell velocities as V_{min} = 3500 km s^{-1} and V_{max} = 4500 km s^{-1} during explosion based on values calculated from the optical and NIR emission lines (e.g., Das et al. 2006; Skopal et al. 2008). The velocities remain constant during the free expansion phase that lasted for first $\sim$ 3 days (taking the average of 2 and 4 days, derived by Sokoloski et al. 2006 and Das et al. 2006, respectively) and then decrease gradually with time (t) $t^{-0.40}$ for $t \leq 5$ days, and as $t^{-0.6}$ for $t = 5 - 70$ days (Das et al. 2006) due to interaction with surrounding matter from the red giant companion. Following this process, I have calculated and found $V_{min} \sim$ 1950 km s^{-1} and $V_{max} \sim$ 2500 km s^{-1} on day 5.5. These values are consistent with the interferometric results (Chesneau et al. 2007) that show the evidence of two different radial velocity fields inside the ejecta, with $V_{min} \leq$ 1800 km s^{-1} and $V_{max} \sim$ 2500 - 3000 km s^{-1}, at day 5.5. The agreement between the two results gives me confidence about the model I have adopted here. Proceeding further, I calculate velocities and expansion of the shells on each date, then add them up to calculate final values of R_{in} and R_{out}. I assume the continuum shape to be a blackbody of high temperature, $10^{5.95} \geq T_{BB} \geq 10^{4.2}$ K, as assumed in the previous investigations, to ensure that it

supplies enough amount of photons for photoionization. Several spectra are generated by varying the free parameters, one after one, *viz.*, hydrogen density, underlying luminosity, effective blackbody temperature and abundances of only those elements which showed observed lines. Abundance of other elements, which does not show any emission line, were fixed at solar values. Since, novae ejecta are not homogenous in density, I assume that the ejecta is composed of at least two different density regions - a higher density region to fit the lower ionization lines and the other lower density region to fit the higher ionization lines. To reduce the number of free parameters in the final model, each component is subjected to the same parameters except hydrogen densities at the inner radius and the covering factors assuming that the sum of the two covering factors be less than or equal to 1. Thus, the overall number of free parameters increases by 2 due to the second component's initial density and covering factor. The final model line ratios were calculated by adding each components line ratio after multiplying by its covering factor. Thus, this method is only a first-order approximation to incorporate density gradients into the photoionization analysis; there is no coupling or interaction between the components, as expected in reality. However, this procedure has been used successfully in case of other novae, e.g., QU Vul (Schwarz 2002), V1974 Cyg (Vanlandingham et al. 2005), V838 Her & V4160 Sgr (Schwarz et al. 2007a), V1186 Sco (Schwraz et al. 2007b) and V1065 Cen (Helton et al. 2010).

Based on parameter space discussed in the above, the CLOUDY output predicts the model fluxes of different emission lines, which are compared with the observed fluxes of emission lines after normalizing with respect to Hβ. The best-fit parameters are determined through chi-square minimization technique. I estimate error in the range of 10 - 30%, depending upon the strength of a spectral line relative to continuum, possibility of blending with other lines, and formal error in the measurement of line flux. A model is considered good if the value of $\chi^2 \sim \nu$ and (χ^2_{red}) value is low (typically in the range of 1 - 2).

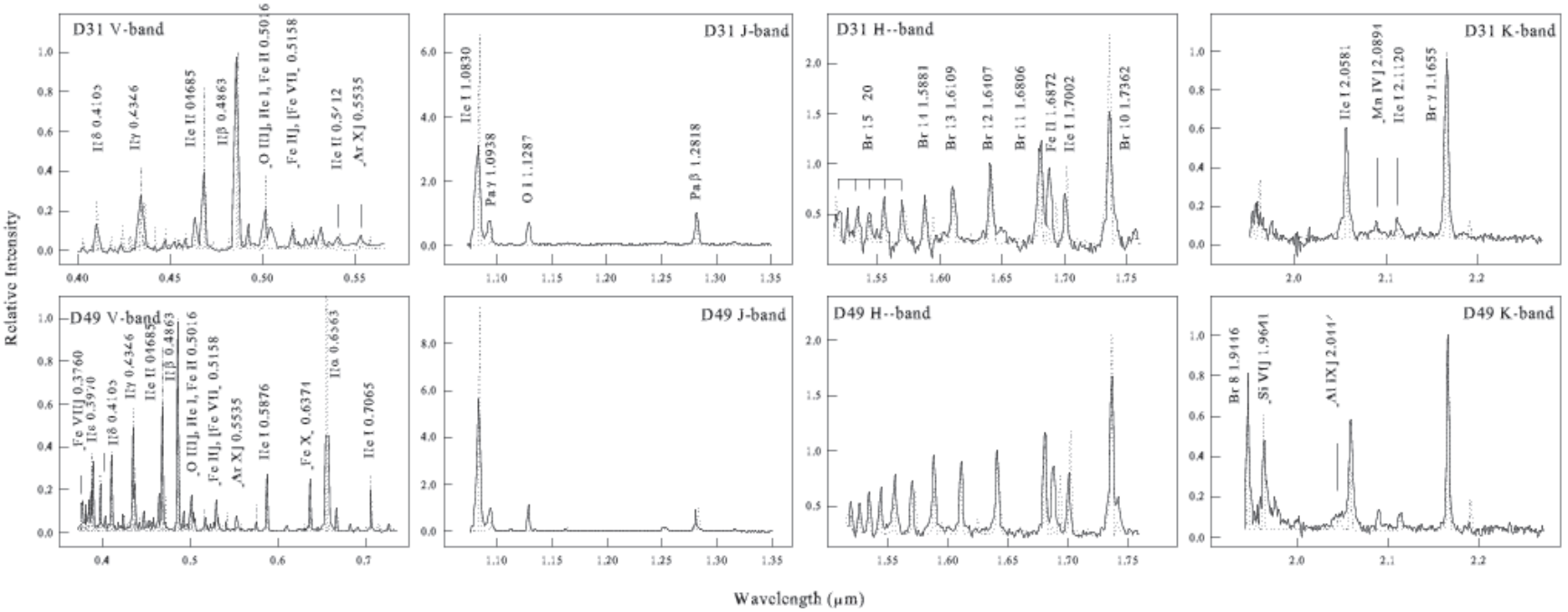

Figure 3.18: Best-fit CLOUDY model (dotted line) spectra plotted over the observed optical and NIR JHK spectra (solid lines) of RS Oph observed on the epochs D31 and D49 during the 2006 outburst. The spectra were normalized to Hβ in optical, Paβ in J band, Br12 in H band and Brγ in K band. Also few of the strong features have been marked (see text for details).

3.4 Results

The results of the analysis are presented in Table 3.3 (using published data) and Table 3.4 & 3.5 (using observed data). Table 3.6, 3.7, & 3.8 show the relative fluxes of the best-fit model predicted and observed lines along with corresponding χ^2 values. Here, I have considered only the lines which are present both in the model generated and observed spectra. To match the predicted luminosities with reddening-corrected observed flux, a distance of 1.6 kpc to RS oph is assumed. The measured line fluxes were compared to the output of each CLOUDY model to calculate χ^2 for the fitting. The line intensities are determined from direct integration of the line; for features with multiple components, the profiles were decomposed with multiple Gaussians using IRAF tasks. To minimize errors associated with flux calibration between different epochs and wavelength regions, I calculate the modelled and observed flux ratios relative to prominent hydrogen lines, which are not blended with any other features, within a given wavelength region, e.g., relative to Hβ in the optical region, relative to Paschen β in the J-band, relative to Brackett 12 in the H-band and relative to Brackett γ in the K-band.

3.4.1 Early Phase: 2006 February – May

The spectra, in the early phase, are dominated by prominent features of low ionisation lines, e.g., Hϵ (3970 Å), Hδ (4101 Å), Hγ (4340 Å), He II (4686 Å), Hβ (4863 Å) in the optical and Pa γ (1.0938 μm), Pa β (1.2818 μm), Brackett series lines, He I (1.0830, 1.7002, 2.0581 μm), O I (1.1287 μm) in the NIR JHK bands. There are also some higher ionisation lines, e.g., [Fe VII] (3760 Å), Fe II and [Ni XII] (4233 Å), He I and [Ar IV] (4713 Å), [Ar X] (5535 Å), [Fe XI] (7890 Å), [Fe X] (6374 Å), [Fe XIV] (5303 Å) etc. in optical; and [Si VI] (1.9641 μm), [Al IX] (2.0444 μm), [Mn XIV] (2.0894 μm) in NIR region, which started to appear at the end of the early phase.

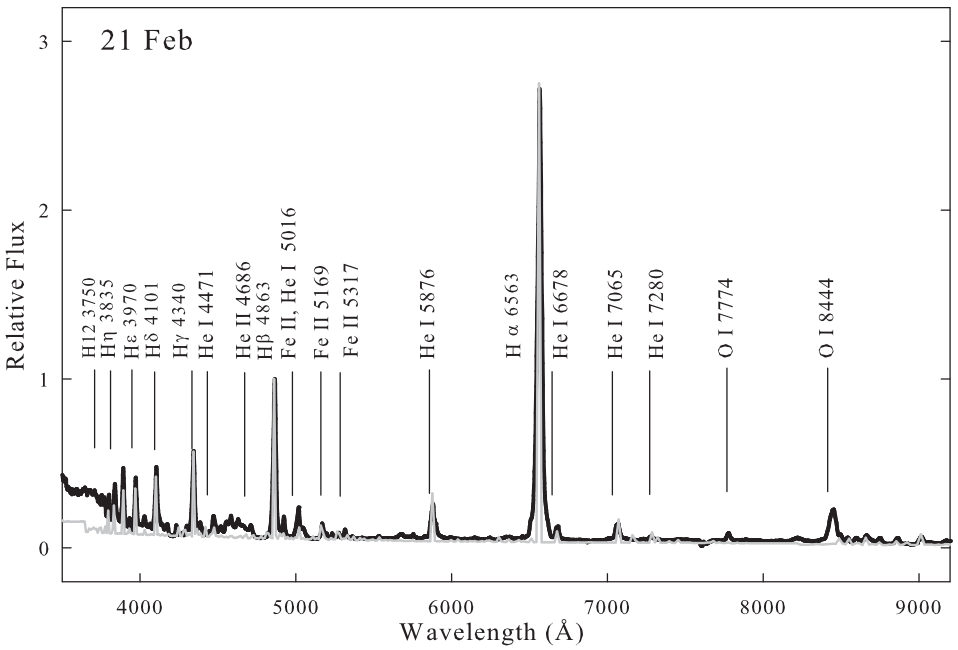

Figure 3.19: Best-fit CLOUDY model spectrum (grey line) plotted over the observed spectrum (black lines) of RS Oph observed on 2006 February 21. The spectra were normalized to Hβ. Also few of the strong features have been marked (see text for details).

Since, the gas is highly inhomogeneous at this time, a one component model was unable to fit the Hα/Hβ flux ratio properly and also a single shell of ejecta could not generate all of these lines. For example, if we consider a clumpy shell of high H-density, e.g., 10^{11} cm^{-3} only, modelled spectra fit majority of the lines in observed spectra, but systematically under represent the higher ionization lines. This one component shell also increases the strength of the K-band He I line enormously. On the other hand, only a diffuse shell of lower density can produce the higher-ionization lines successfully but can not produce He I and Fe II lines sufficiently to match the observed lines. Hence, for a better fitting of the lines, I required to consider two-component model consisting of a dense shell (hydrogen densities, by number: $10^{8.5}$ - $10^{11.0}$ cm^{-3}) and a diffuse shell ($10^{7.6}$ - $10^{10.5}$ cm^{-3}). The first component (clump) consisted of a highly dense cloud to fit the lower ionisation lines. This component was optically thick, and Case-B was taken into consideration as well. Majority of the observed lines were generated using this

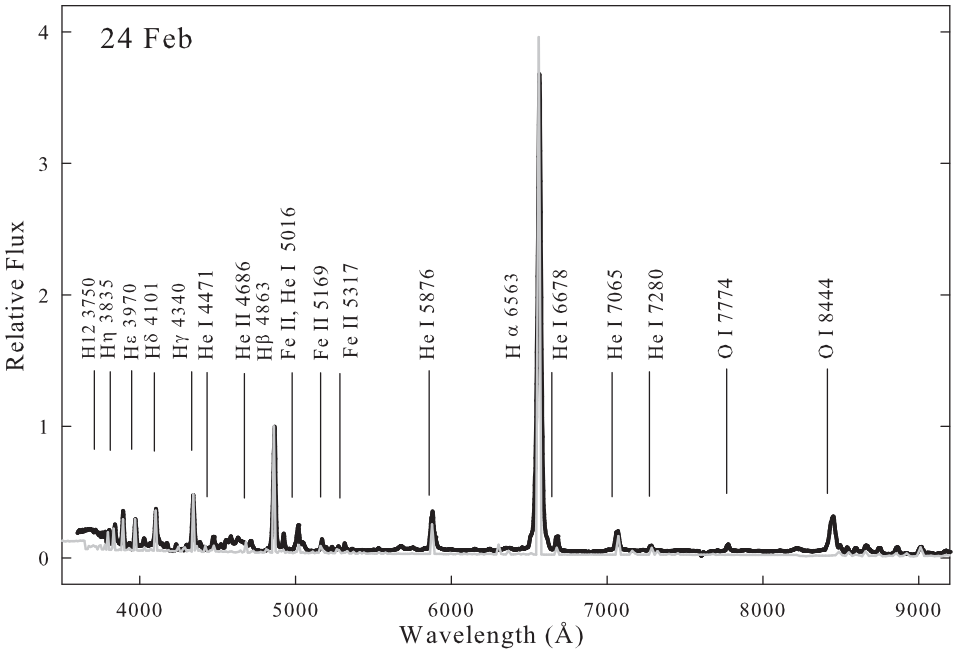

Figure 3.20: Best-fit CLOUDY model spectrum (grey line) plotted over the observed spectrum (black lines) of RS Oph observed on 2006 February 24. The spectra were normalized to Hβ. Also a few of the strong features have been marked (see text for details).

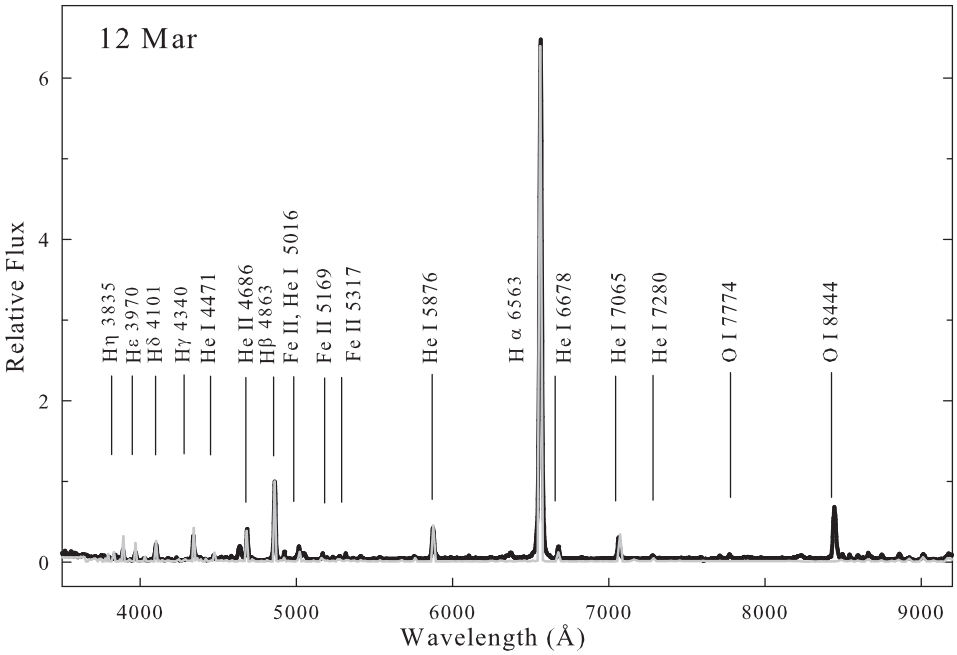

Figure 3.21: Best-fit CLOUDY model spectrum (grey line) plotted over the observed spectrum (black lines) of RS Oph observed on 2006 March 12. The spectra were normalized to Hβ. Also a few of the strong features have been marked (see text for details).

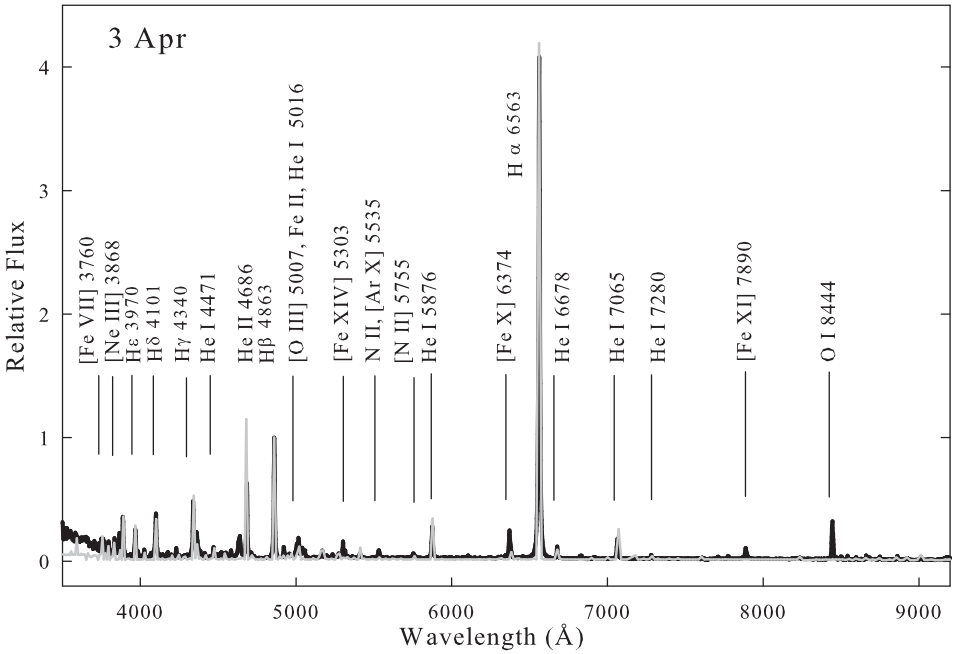

Figure 3.22: Best-fit CLOUDY model spectrum (grey line) plotted over the observed spectrum (black lines) of RS Oph observed on 2006 April 3. The spectra were normalized to Hβ. Also a few of the strong features have been marked (see text for details).

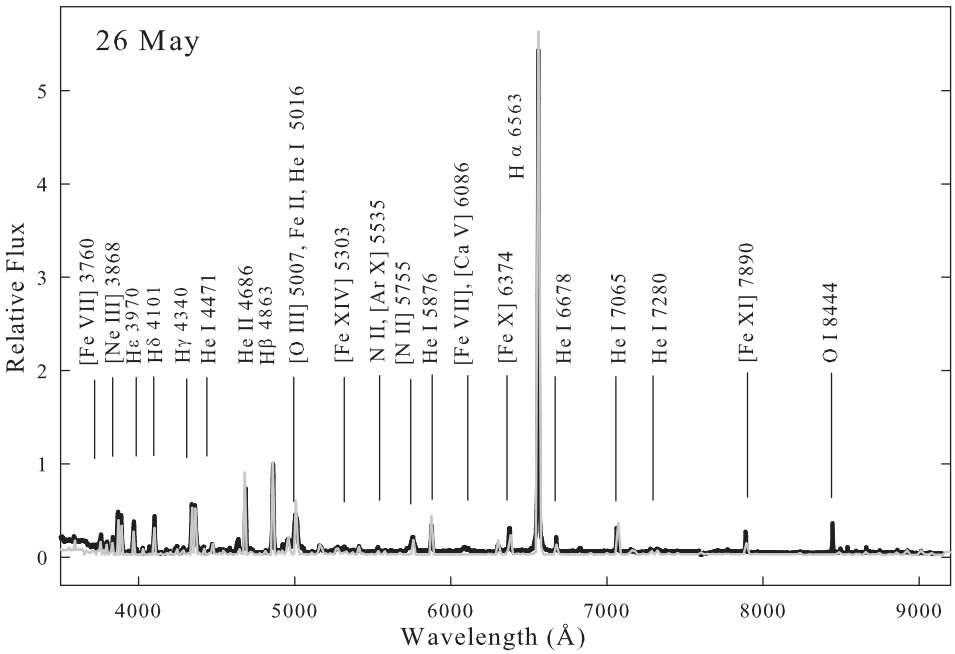

Figure 3.23: Best-fit CLOUDY model spectrum (grey line) plotted over the observed spectrum (black lines) of RS Oph observed on 2006 May 26. The spectra were normalized to Hβ. Also a few of the strong features have been marked (see text for details).

component, but it under-represents the highest ionisation lines. The second component (diffuse), with a lower density, was less $(10 - 30\%)$ in volume, but it allowed the source photon to ionise some of the species to their higher ionisation states (e.g., [Ar IV] (4713 Å), [Ar X] (5535 Å), [Al IX] (2.0444 μm), [Mn XIV] (2.0894 μm)), while not changing the clump contribution to the spectra.

Initially, in 2006 February, the ionising source was surrounded by a dense ($n_H \sim 10^{11}$ cm^{-3}) cloud. So, the effective temperature and luminosity ($T \sim 10^{4.45}$ K, $L \sim 10^{36.8}$ erg s^{-1}) of the source is relatively lower. As the ejecta expands, more energy from the central engine comes out. Therefore, while the ejecta density decreases ($n_H \sim 10^{8.41}$ cm^{-3}), the blackbody temperature (T_{BB}) and the luminosity increases to $T_{BB} \sim 10^{5.6}$ K and L $\sim 10^{37.1}$ erg s^{-1}, respectively in 2006 May to photoionize more matter. This is in agreement with the WD temperature $\sim 8 \times 10^5$ K derived from x-ray studies by Nelson et al. (2008). The estimated elemental abundances during this phase are given as logarithm of the numbers relative to hydrogen and relative to solar in Table 3.3 and 3.4.

The values show that helium, nitrogen, oxygen, neon, argon, iron and nickel abundances are all enhanced relative to solar whereas abundances of calcium and sulphur are at solar values. However, one must be cautious while considering the abundances of calcium, because calcium abundance was calculated using only the Ca V (6086 Å) line observed on 2006 May 26. This line is blended with [Fe VII]. So, first iron abundance was set using the other prominent Fe II (4180 Å, 4415 Å and 4584 Å) lines. Then, the calcium abundance was changed such that the total flux of the blended feature in the model matched the observed spectra. Similarly, nitrogen abundance on day 28 was determined using the N II (5535 Å) line blended with [Ar X]. But, on days 50 and 103, there are two other N II (4242 Å and 5755 Å) lines that helped to set the nitrogen abundance correctly. The best fit modelled spectra (dotted line) with the observed optical

and NIR spectra (solid lines) on D31 and D49, are shown in Fig. 3.18. The best fit modelled spectra (grey lines) with the observed optical spectra from HCT (black lines) during this phase are shown in Fig. 3.19 - 3.23.

Nebular Phase: 2006 July – October

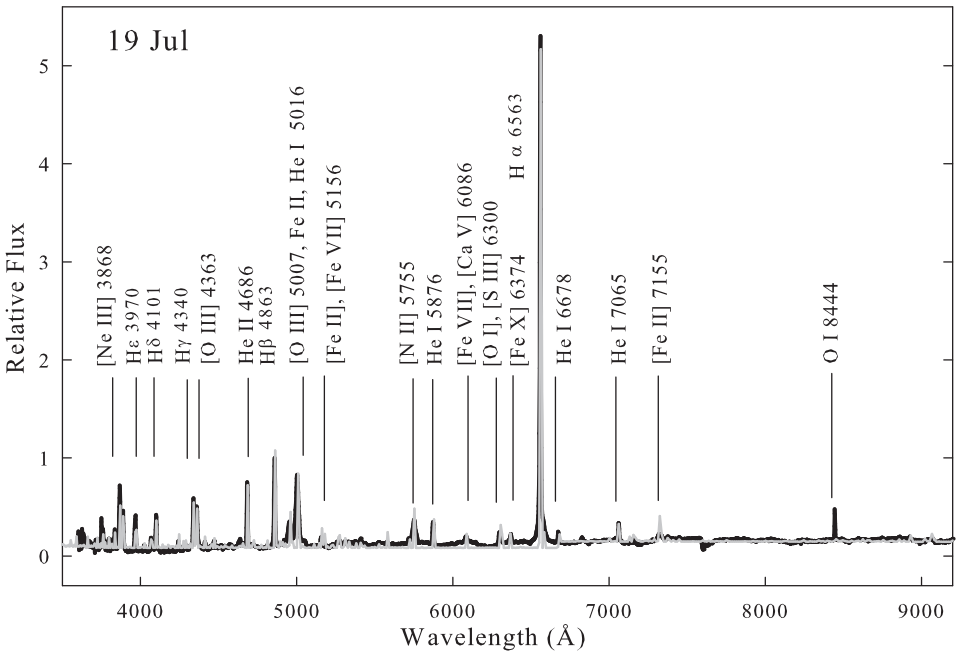

Figure 3.24: Best-fit CLOUDY model spectrum (grey line) plotted over the observed spectrum (black lines) of RS Oph observed on 2006 July 19. The spectra were normalized to Hβ. Also a few of the strong features have been marked (see text for details).

Prominent appearance of higher ionisation lines like [O III](4363, 4959, 5007 Å) and [O I] (6300 Å) in the day 103 spectrum indicates that the nova is entering the nebular phase. Due to the expansion of the shell, the cloud becomes thinner and consequently higher ionisation lines are seen in the spectra. Modelling of nebular phase was simpler as only one component of relatively lower hydrogen density was sufficient to generate the high as well as the low ionisation emission lines observed in the spectra. The line fluxes and χ^2 values are presented in Table 3.7 and the best-fit model parameters are presented in Table 3.5. During this phase, the effective temperature and luminosity were increased

Table 3.3: Best-fit CLOUDY model parameters of RS Oph (using published data).

Parameters	Mar 15 D(31)[a]	Apr 2 D(49)	Predicted Abundances
Log(T_{BB}) (K)	5.76	5.74	...
Log(L) (erg s^{-1})	36.8	36.9	...
Log(n_H)[Clump] (cm^{-3})	9.0	8.8	...
Log(n_H)[Diffuse] (cm^{-3})	8.2	8.0	...
Clump to diffuse covering factor	90/10	85/15	...
α[b]	-3	-3	...
Log(R_{in}) (cm)	14.52	14.45	...
Log(R_{out}) (cm)	14.68	14.83	...
Filling factor (f)	0.1	0.1	...
β[c]	0.0	0.0	...
He/He$_\odot$[d]	1.8(11)	1.9(16)	1.8 ± 0.1
N/N$_\odot$	...	12.0(2)	12 ± 1.0
O/O$_\odot$	1.0(1)	1.0(1)	1.0 ± 0.4
Ne/Ne$_\odot$	...	1.5(1)	1.5 ± 0.1
Si/Si$_\odot$	0.3(1)	0.5(1)	0.4 ± 0.1
Ar/Ar$_\odot$	4.9(1)	5.2(2)	5.1 ± 0.1
Fe/Fe$_\odot$	3.0(12)	3.5(11)	3.2 ± 0.2
Al/Al$_\odot$	0.9(1)	1.1(1)	1.0 ± 0.1
Ejected Mass ($\times 10^{-6}$ $M_\odot$)	3.4	4.9	...
No. of observed lines (n)	42	51	...
No. of free parameters (n_p)	11	13	...
Degrees of freedom (ν)	31	38	...
Total χ^2	38.0	69.1	...
χ^2_{red}	1.2	1.8	...

a Time elapsed after discovery (in days)
b Radial dependence of the density r^α
c Radial dependence of filling factor r^β
d Abundances are given in logarithmic scale, relative to solar abundances. All other elements which are not listed in the table were set to their solar values. The number in the parentheses represents number of lines used in determining each abundance.

Table 3.4: Best-fit CLOUDY model parameters of RS Oph during early phase (2006).

Parameters	Feb. 21 (D9)[a]	Feb. 24 (D12)	Mar. 12 (D28)	Apr. 3 (D50)	May 26 (D103)
Log(T_{BB}) (K)	4.45	4.5	5.0	5.5	5.6
Log(L) (erg s^{-1})	36.9	36.8	37	37	37.1
Log(n_H)[Clump] (cm^{-3})	11.0	10.8	9.5	8.8	8.5
Log(n_H)[Diffuse] (cm^{-3})	10.5	9.8	8.2	8.0	7.6
Clump to diffuse covering factor	70/30	70/30	80/20	85/15	90/10
α[b]	-3	-3	-3	-3	-3
Log(R_{in}) (cm)	13.94	14.01	14.28	14.45	14.71
Log(R_{out}) (cm)	14.26	14.33	14.63	14.83	15.13
Filling factor (f)	0.1	0.1	0.1	0.1	0.1
β[c]	0.0	0.0	0.0	0.0	0.0
He/He$_\odot$[d]	1.7(9)	1.75(10)	1.8(10)	1.9(11)	2.5(11)
N/N$_\odot$	...	...	11.0(1)	12(3)	10(3)
O/O$_\odot$	...	...	1.0(1)	1.0(2)	5(3)
Ne/Ne$_\odot$	1.9(1)	2.0(1)	2.0(1)	2.5(2)	5(3)
Ar/Ar$_\odot$	...	4.0(1)	4.9(2)	5.2(2)	5.5(1)
Fe/Fe$_\odot$	2.7(7)	2.8(7)	3.0(4)	3.5(9)	3.8(8)
Ca/Ca$_\odot$	...	...	...	...	1.0(1)
S/S$_\odot$	...	...	...	...	1.0(1)
Ni/Ni$_\odot$	1.5(1)	1.8(1)	2.0(1)	2.0(1)	2.0(1)
CaseB-τ-Value	4.8	4.2	...	...	...
Number of observed lines (n)	27	28	26	36	38
Number of free parameters (n_p)	9	10	12	12	14
Degrees of freedom (ν)	18	18	14	24	24
Total χ^2	21.60	20.28	17.71	30.49	32.94
χ^2_{red}	1.2	1.13	1.26	1.27	1.37

a Time elapsed after discovery (in days)
b Radial dependence of the density r^α
c Radial dependence of filling factor r^β
d Abundances are given in logarithmic scale, relative to solar abundance. All other elements which are not listed in the table were set to their solar values. The number in the parentheses represents number of lines used in determining each abundance.

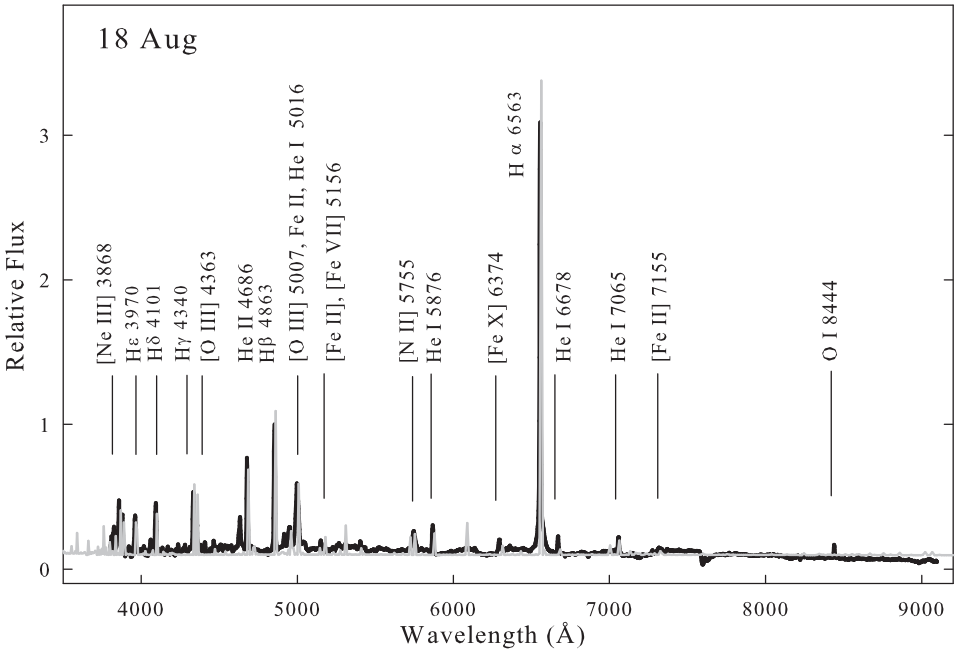

Figure 3.25: Best-fit CLOUDY model spectrum (grey line) plotted over the observed spectrum (black lines) of RS Oph observed on 2006 August 18. The spectra were normalized to Hβ. Also a few of the strong features have been marked (see text for details).

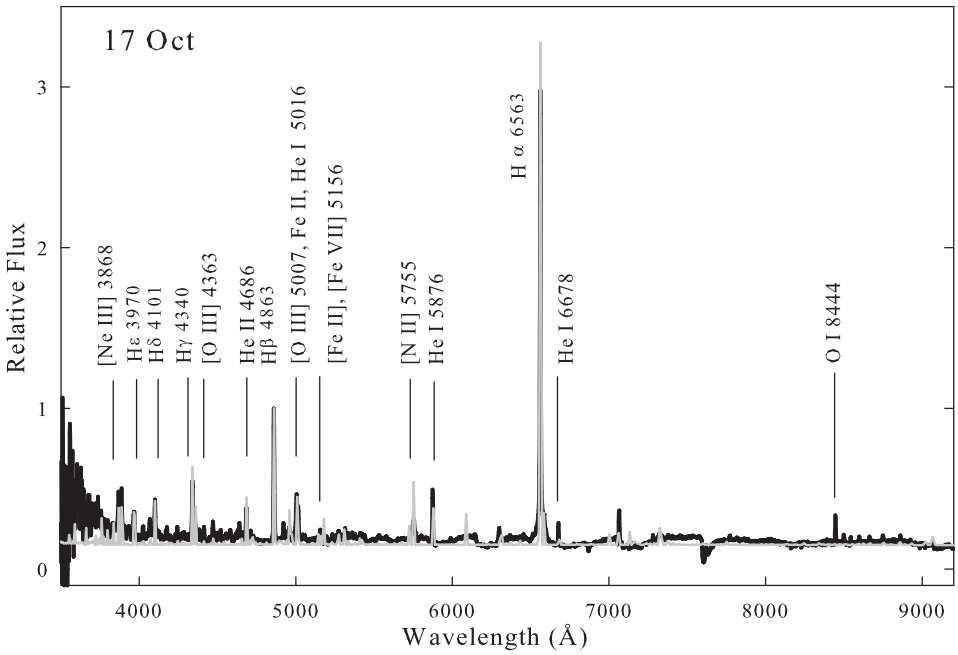

Figure 3.26: Best-fit CLOUDY model spectrum (grey line) plotted over the observed spectrum (black lines) of RS Oph observed on 2006 October 17. The spectra were normalized to Hβ. Also a few of the strong features have been marked (see text for details).

to $10^{5.95}$ K and $10^{37.5}$ ergs s^{-1}, respectively, and the hydrogen density was decreased to $10^{7.18}$ cm^{-3} to match the observed spectra. The estimated value of temperature is in agreement with the WD temperature of around 8×10^5 K derived from X-ray studies (Nelson et al. 2008). During the early phase, I have seen that the abundances of several elements were enhanced relative to solar, but as the nebular phase set in, the oxygen, neon and iron abundances become sub-solar, whereas, sulphur abundance enhanced from a solar abundance seen in the early phase. In the nebular phase also the calcium abundance, which was at solar value, was calculated using only the blended Ca V (6086 Å) line. But, the nitrogen abundance was determined correctly as the prominent [N II] (5755 Å) line is highly sensitive to the change in abundance parameter in CLOUDY. The best fit modelled spectra (grey lines) with the observed optical spectra (black lines) during this phase are shown in Fig. 3.24 - 3.26.

3.4.2 Calculation of Ejected Mass

Using the parameter values determined from the present analysis, we can estimate the hydrogen ejected mass predicted by the two component models using the following relation (e.g., Schwarz et al. 2001; Schwarz 2002),

$$M_{shell} = n(r_0) f(r_0) \int_{R_{in}}^{R_{out}} (r/r_0)^{\alpha+\beta} 4\pi r^2 dr \tag{3.1}$$

The resulting mass is then multiplied by corresponding covering factors to obtain mass of the dense and diffuse shells; final mass is calculated by adding mass of these two shells. Using this method, I find an ejected mass of 3.4×10^{-6} $M_\odot$ and 4.9×10^{-6} $M_\odot$ for D31 and D49, respectively. A similar value of $1 - 3 \times 10^{-6}$ $M_\odot$ and 3×10^{-6} $M_\odot$ were estimated from other studies of the recent outburst of RS Oph (Kato et al. 2008; Das et al. 2006). O' Brien et al. (1992) also derived an ejecta mass of 1.1×10^{-6} $M_\odot$, from X-ray studies of the 1985 outburst of RS oph. From light curve analysis, Hachisu

Table 3.5: Best-fit CLOUDY model parameters of RS Oph during nebular phase (2006).

Parameters	Jul 19 (D159)	Aug 18 (D189)	Oct. 17 (D249)
Log(T_{BB}) (K)	5.8	5.9	5.95
Log(L) (erg s^{-1})	37	37.5	37.3
Log(n_H) (cm^{-3})	7.74	7.61	7.18
α^b	-3	-3	-3
Log(R_{in}) (cm)	15.0	15.1	15.28
Log(R_{out}) (cm)	15.3	15.4	15.6
Filling factor (f)	0.1	0.1	0.1
β^c	0.0	0.0	0.0
He/He$_\odot^d$	2.0(8)	1.6(8)	1.6(6)
N/N$_\odot$	5.0(1)	8.0(1)	3.0(1)
O/O$_\odot$	0.7(5)	0.3(4)	0.3(4)
Ne/Ne$_\odot$	1.0(2)	0.7(2)	0.5(2)
Fe/Fe$_\odot$	0.5(9)	0.5(8)	0.5(6)
Ca/Ca$_\odot$	1.0(1)	...	...
S/S$_\odot$	1.5(1)	...	1.5(1)
Number of observed lines (n)	26	24	21
Number of free parameters (n_p)	11	10	10
Degrees of freedom (ν)	15	14	11
Total χ^2	19.44	14.69	15.24
χ^2_{red}	1.29	1.05	1.39

a Time elapsed after discovery (in days)
b Radial dependence of the density r^α
c Radial dependence of filling factor r^β
d Abundances are given in logarithmic scale, relative to solar abundance. All other elements which are not listed in the table were set to their solar values. The number in the parentheses represents number of lines used in determining each abundance.

& Kato (2001) estimated an ejecta mass of $\sim 2 \times 10^{-6}$ $M_{\odot}$ for WD of mass of 1.35 $M_{\odot}$. Therefore the present result also favors the possibility of high mass of ~ 1.35 $M_{\odot}$ in RS Oph system.

3.5 Discussion

Line flux ratios of observed and model generated spectra with their corresponding χ^2 values are shown in Table 3.6 (using published optical and NIR data during D31 and D49), Table 3.7 (using observed optical HCT spectra during the early phase) and Table 3.8 (using observed optical HCT spectra during the nebular phase). Low values of χ^2_{red} (between 1.05 to 1.8) indicate that the model generated spectra match well with the observed ones. However, inspite of the low χ^2_{red} values, there are a few discrepancies. An inspection of the Tables 3.6, 3.7, and 3.8 show that χ^2 values of some lines are relatively higher. For example, He II (4686 Å), blended feature of [O III], He I & Fe II (5017 Å) on D31 and Hϵ & [N III] (3970 Å), Hδ, [Fe X] (6374 Å), He I (7065 Å, 1.0830 and 2.0581 μm), Paγ, Br 16 and 17 on D49 contibute towards higher χ^2 values. The reason for this misfits is that the model could not generate the lines to the observed strengths. There is other possibility that I might have underestimated the errors for these lines in the calculation of the χ^2. Also Hα (6563 Å) on most of the epochs in the optical spectra and Hγ (4340 Å) on 2006 February 21 are the highest contributors to the χ^2 values. Hence, total χ^2 value increases when these two strong lines are considered. Also, while adding the two components, emphasis was given to minimize the total χ^2 value, which leads to difficulty in matching the line flux ratios perfectly to the observed one. This problem disappears during modelling of the nebular phase spectra where only one component of Hydrogen density was enough to fit all the lines. The other lines that contribute to higher χ^2 values are: [Fe X] (6374 Å) and He I (6678 Å) on 2006 April 3. This is not surprising since [Fe X] is a coronal line, most likely excited by the shock

Table 3.6: Observed and best-fit CLOUDY model line fluxes (using published data).

λ (Å)	Line	D31 Observed	D31 Modelled	D31 χ^2	D49 Observed	D49 Modelled	D49 χ^2
			Optical				
3760	[Fe VII]	...	...	...	0.21	0.12	0.80
3868	[Ne III]	...	...	...	0.32	0.32	0.00
3868	H I, He I	...	...	...	0.43	0.36	0.49
3970	Hϵ, [N III]	...	...	...	0.24	0.45	4.40
4029	He I, He II	0.01	0.05	0.12	0.16	0.05	1.21
4103	Hδ	0.14	0.20	0.34	0.51	0.31	3.99
4233	Fe II, [Ni XII]	0.02	0.17	2.02	0.14	0.07	0.42
4341	Hγ	0.38	0.40	0.04	0.50	0.55	0.25
4415	[Fe II]	0.02	0.10	0.65	0.07	0.07	0.00
4472	He I	0.05	0.12	0.56	0.11	0.10	0.01
4523	Fe II	0.04	0.10	0.46	0.08	0.06	0.04
4549	Fe II	0.04	0.11	0.47	0.08	0.06	0.04
4590	Fe II	0.04	0.11	0.45	0.08	0.04	0.16
4666	He II	0.35	0.57	4.60	0.73	0.79	0.36
4863	Hβ	1.00	1.00	0.00	1.00	1.00	0.00
4923	He II, Fe II	0.07	0.11	0.18	0.15	0.07	0.64
5017	[O III], He I, Fe II	0.23	0.46	5.29	0.43	0.29	1.96
5158	[Fe II], [Fe VII]	0.08	0.18	0.92	0.16	0.28	1.44
5235	Fe II	0.03	0.04	0.01	...	...	...
5276	Fe II	0.04	0.15	1.12	...	...	...
5317	Fe II	0.01	0.05	0.14	...	...	...
5411	He II	0.01	0.10	0.25	0.08	0.10	0.03
5535	[Ar X]	0.05	0.08	0.11	0.14	0.6	0.64
5755	[N II]	...	...	...	0.12	0.16	0.16
5876	He I	...	...	...	0.42	0.43	0.01
6374	[Fe X]	...	...	...	0.33	0.14	3.61
6678	He I	...	...	...	0.23	0.13	1.00
6919	[Ar XI]	...	...	...	0.10	0.04	0.36
7065	He I	...	...	...	0.22	0.40	3.20
7281	He I	...	...	...	0.13	0.09	0.16

continued ...

λ (μm)	Line	D31 Observed	Modelled	χ^2	Observed	D49 Modelled	χ^2
			J-band				
1.0830	He I	4.39	4.70	2.40	11.80	11.45	3.06
1.0938	Paγ	1.02	0.78	1.44	1.79	0.85	9.82
1.1626	He II	0.11	0.10	0.02	0.40	0.26	1.96
1.2818	Paβ	1.00	1.00	0.00	1.00	1.00	0.00
			H-band				
1.5184	Br 20	0.57	0.50	0.49	0.33	0.29	0.16
1.5256	Br 19	0.31	0.24	0.49	0.38	0.25	1.69
1.5341	Br 18	0.45	0.37	0.64	0.47	0.38	0.81
1.5439	Br 17	0.45	0.31	1.96	0.60	0.38	4.84
1.5570	Br 16	0.71	0.63	0.64	0.91	0.73	3.24
1.5685	Br 15	0.66	0.53	1.69	0.60	0.60	0.00
1.5881	Br 14	0.76	0.69	0.49	0.77	0.70	0.49
1.6109	Br 13	0.82	0.55	1.82	0.69	0.59	1.00
1.6407	Br 12	1.00	1.00	0.00	1.00	1.00	0.00
1.6806	Br 11	1.81	1.82	0.01	1.34	1.20	1.96
1.6872	Fe II	1.01	0.91	0.99	0.91	0.78	1.69
1.7002	He I	0.69	0.79	1.00	0.74	0.90	2.56
1.7362	Br 10	2.18	2.26	0.64	2.10	2.26	2.56
1.7406	Fe II	0.34	0.28	0.36	0.69	0.58	1.21
			K-band				
1.9446	Br 8	...	...	...	0.8	0.86	0.36
1.9621	[Si VI]	0.46	0.29	2.28	1.3	1.80	0.64
2.0444	[Al IX]	0.04	0.08	0.13	0.13	0.10	0.09
2.0581	He I	0.71	0.44	1.80	0.87	0.40	5.50
2.1120	He I	0.14	0.08	0.36	0.13	0.12	0.04
2.1655	Brγ	1.00	1.00	0.00	1.00	1.00	0.00
Total				37.99			69.06

Line fluxes are taken relative to Hβ in optical, Paβ in J band, Br 12 in H band and Brγ in K band.

interaction. The He I line is suppressed due to a high optical depth, which is not well accounted for in the model. The He II line at 4686 Å in the modelled spectrum was weak on February 21 and 24. This is possibly because the temperature of the source on those two epochs ($10^{4.45}$ & $10^{4.5}$ K respectively) was low. Higher temperature $> 10^{4.7}$ K is required to generate the He II line (ionization potential ~ 54.4 eV) prominently, as seen in the spectra of March 12 onwards, when the central source temperature was $> 10^5$ K. Further, the He II 4686 line was very weak in the observed spectra on those two epochs, and it was difficult to measure the flux correctly. Therefore, the He II feature was not included in the calculation of the total χ^2 for those epochs.

In spite of the discrepancies, these fits do minimize the total χ^2 values. During the nebular phases, the highest contributions to the total χ^2 is due to the blending of [O III], Fe II and He I lines at 5007 Å. Also, the abundances for Fe, He and O were set after matching the other Fe, He and O lines, which leads to a high (about 30 - 40%) χ^2 contribution. In addition, there are some problems in modelling. CLOUDY was unable to adequately reproduce the observed emission, e.g., Si II (5041, 5056 Å), Fe II (5235, 5276, 5317 Å), [Fe XIV] (5303 Å), N III (4640 Å), Raman emission band (6830 Å), He I (1.1969, 1.2527, 2.1120 μm), N I (1.2074, 1.2096, 1.2470 μm), O I (7774, 8446 Å, 1.1287, 1.3164 μm), O VI (6106 Å), Ca II (8668, 8548 Å), and [Mn XIV] (2.0894 μm). So, I have excluded these lines from the analysis while calculating the values of χ^2. This is possibly due to the reason that even a two-component model can not properly represent the complex density structure of the nova ejecta. The problem of reproducing the NIR O I emission lines (1.1287 μm and 1.3164 μm) and He I (2.0581 μm) has also been reported by Helton et al. (2010). They attributed these difficulties to related excitation mechanisms which are not properly included in the present CLOUDY code.

Table 3.7: Observed and best-fit CLOUDY model line fluxes during early phase.

λ		Feb. 21			Feb. 24			Mar. 12			Apr. 3			May. 26		
(Å)	Line	Obs.	Mod.	χ^2	Obs.	Mod.	χ^2	Obs.	Mod.	χ^2	Obs.	Mod.	χ^2	Obs.	Mod.	χ^2
3750	H12	0.04	0.04	0.00	0.02	0.05	0.09	...	...	...	...	...	...	...	...	...
3760	[Fe VII]	...	...	...	...	...	...	...	...	...	0.07	0.19	1.62	0.31	0.14	2.85
3771	H11	0.06	0.01	0.22	0.03	0.04	0.00	...	...	...	...	...	...	0.03	0.05	0.06
3798	H10	0.10	0.06	0.18	0.06	0.06	0.00	0.03	0.07	0.17	0.07	0.06	0.02	0.08	0.10	0.08
3835	Hη	0.18	0.07	1.17	0.14	0.17	0.08	0.04	0.12	0.61	0.10	0.14	0.21	0.13	0.13	0.0
3868	[Ne III]	...	...	...	...	...	...	...	...	...	0.20	0.14	0.42	0.62	0.49	1.67
3889	Hζ, He I	0.27	0.14	1.82	0.22	0.20	0.06	0.12	0.15	0.10	0.26	0.29	0.10	0.38	0.29	0.7
3970	Hϵ, [Ne III]	0.26	0.21	0.29	0.18	0.13	0.26	0.12	0.16	0.30	0.26	0.19	0.46	0.36	0.21	2.22
4026	He I, He II	0.05	0.03	0.04	0.05	0.03	0.06	0.04	0.06	0.04	0.05	0.06	0.02	0.05	0.06	1.83
4070	[S II]	...	...	...	...	...	...	...	...	...	...	...	...	0.10	0.03	0.55
4101	Hδ	0.34	0.32	0.02	0.28	0.29	0.02	0.22	0.19	0.09	0.33	0.33	0.0	0.05	0.28	0.48
4144	He I	...	...	...	...	...	...	...	...	...	...	...	...	0.03	0.02	0.02
4180	Fe II, [Fe II]	...	...	...	...	...	...	...	...	...	0.05	0.02	0.10	0.06	0.03	0.09
4233	Fe II, [Ni XII]	0.05	0.06	0.00	0.03	0.04	0.00	0.03	0.03	0.00	0.06	0.04	0.03	0.07	0.05	0.04
4242	N II	...	...	...	...	...	...	...	...	...	0.02	0.04	0.05	0.09	0.07	0.05
4340	Hγ	0.45	0.22	5.33	0.39	0.33	0.29	0.30	0.34	0.19	0.34	0.29	0.22	0.52	0.40	1.38
4415	[Fe II]	...	...	...	...	...	...	...	...	...	0.04	0.04	0.00	0.06	0.07	0.00
4471	He I	0.11	0.07	0.12	0.09	0.06	0.10	0.05	0.11	0.44	0.06	0.09	0.14	0.11	0.12	0.00
4584	Fe II	...	...	...	...	...	...	0.03	0.03	0.00	0.04	0.05	0.02	...	...	...
4686	He II	...	...	...	...	...	...	0.34	0.19	2.22	0.52	0.37	1.9	0.65	0.52	1.82
4713	He I, [Ar IV]	...	...	...	0.04	0.03	0.00	0.02	0.01	0.03	0.21	0.07	1.9	...	...	...
4863	Hβ	1.00	1.00	0.00	1.00	1.00	0.00	1.00	1.00	0.00	1.00	1.00	0.00	1.00	1.00	0.00
4922	Fe II, He I	0.09	0.05	0.19	0.09	0.06	0.06	0.07	0.06	0.01	0.06	0.04	0.05	0.09	0.11	0.04
4959	[O III]	...	...	...	...	...	...	...	...	...	0.06	0.05	0.00	0.46	0.31	2.15

continued ...

λ		Feb. 21			Feb. 24			Mar. 12			Apr. 3			May. 26		
(Å)	Line	Obs.	Mod.	χ^2	Obs.	Mod.	χ^2	Obs.	Mod.	χ^2	Obs.	Mod.	χ^2	Obs.	Mod.	χ^2
5007	[O III]	...	...	...	...	...	...	...	...	...	0.23	0.14	0.84	1.06	0.01	0.23
5016	Fe II, He I	0.15	0.08	0.43	0.18	0.07	1.16	...	...	...	...	...	...	...	...	...
5169	Fe II	0.08	0.13	0.28	0.09	0.08	0.01	...	...	...	...	...	...	...	...	...
5235	Fe II	0.02	0.18	2.57	0.02	0.01	0.01	...	...	...	...	...	...	...	...	...
5276	Fe II	0.03	0.08	0.29	0.03	0.06	0.08	...	...	...	...	...	...	...	...	...
5303	[Fe XIV]	...	...	...	...	...	...	...	...	...	0.10	0.09	0.02	...	...	...
5317	Fe II	0.05	0.04	0.02	0.04	0.03	0.00	...	...	...	...	...	...	...	...	...
5412	He II	...	...	...	...	...	...	...	...	...	0.06	0.10	0.19	0.09	0.09	0.00
5535	N II, [Ar X]	...	...	...	...	...	...	0.02	0.02	0.00	0.09	0.02	0.47	0.08	0.04	0.15
5755	[N II]	...	...	...	...	...	...	...	...	...	0.07	0.04	0.12	0.43	0.32	1.26
5876	He I	0.31	0.30	0.00	0.44	0.24	3.98	0.50	0.46	0.16	0.29	0.34	0.28	0.29	0.43	.89
6086	[Fe VII], [Ca V]	...	...	...	...	...	...	...	...	...	...	...	...	0.20	0.32	1.55
6101	O IV	...	...	...	...	...	...	0.03	0.03	0.00	...	...	...	...	...	...
6300	[O I]	...	...	...	...	...	...	...	...	...	...	...	...	0.12	0.18	0.37
6374	[Fe X]	...	...	...	...	...	...	...	...	...	0.32	0.07	6.27	0.33	0.29	0.16
6563	Hα	4.74	4.45	8.26	6.12	5.76	12.53	9.60	9.24	12.72	5.81	6.15	12.08	4.46	4.75	8.83
6678	He I	0.09	0.08	0.02	0.14	0.06	0.64	0.17	0.12	0.23	0.08	0.1	4.62	0.12	0.12	0.00
6830	Raman	...	...	...	...	...	...	0.03	0.01	0.03	...	...	...	...	...	...
7065	He I	0.14	0.16	0.02	0.24	0.16	0.63	0.37	0.35	0.03	0.19	0.27	0.65	0.21	0.37	0.67
7280	He I	0.03	0.08	0.23	0.07	0.06	0.00	0.03	0.04	0.01	0.02	0.04	0.05	0.02	0.05	0.13
7890	[Fe XI]	...	...	...	...	...	...	...	...	...	0.15	0.02	1.65	0.16	0.06	0.96
8598	Pa 14	0.03	0.04	0.00	0.04	0.03	0.00	0.05	0.03	0.05	0.02	0.02	0.0	0.02	0.03	0.02
8750	Pa 12	0.04	0.03	0.00	0.06	0.06	0.00	0.07	0.04	0.07	0.03	0.03	0.0	0.02	0.03	0.02
8862	Pa 11	0.06	0.04	0.03	0.08	0.04	0.13	0.09	0.06	0.09	0.03	0.03	0.0	0.02	0.03	0.03
9015	Pa 10	0.09	0.10	0.02	0.09	0.11	0.03	0.12	0.09	0.09	0.03	0.06	0.09	0.01	0.07	0.42
Total		...	...	21.60	...	...	20.28	...	...	17.71	...	...	30.49	...	...	32.94

Table 3.8: Observed and best-fit CLOUDY model line fluxes during nebular phase.

λ		Jul. 19			Aug. 18			Oct. 17		
(Å)	Line	Obs.	Mod.	χ^2	Obs.	Mod.	χ^2	Obs.	Mod.	χ^2
3868	[Ne III]	0.80	0.65	1.00	0.44	0.51	0.22	0.30	0.54	2.56
3889	Hζ, He I	0.38	0.29	0.36	0.26	0.18	0.28	0.28	0.20	028
3970	Hϵ, [Ne III]	0.43	0.31	0.64	0.37	0.19	1.44	0.30	0.18	0.64
4026	He I, He II	0.09	0.04	0.11	0.08	0.02	0.16	0.08	0.02	0.16
4101	Hδ	0.38	0.28	0.44	0.43	0.28	1.0 0	0.31	0.27	0.07
4180	Fe II, [Fe II]	0.06	0.02	0.07	0.09	0.01	0.28	...	...	...
4244	[Fe II]	0.12	0.10	0.02	0.16	0.02	0.87	0.23	0.02	1.96
4340	Hγ	0.56	0.46	0.44	0.49	0.49	0.00	0.34	0.43	0.36
4363	[O III]	0.72	0.54	1.44	0.31	0.32	0.00	0.09	0.05	0.07
4415	[Fe II]	0.09	0.08	0.00	0.08	0.01	0.22	0.14	0.02	0.64
4471	He I	0.08	0.09	0.00	0.11	0.08	0.04	0.14	0.04	0.44
4686	He II	0.65	0.66	0.00	0.62	0.60	0.02	0.29	0.50	1.96
4863	Hβ	1.00	1.00	0.00	1.00	1.00	0.00	1.00	1.00	0.00
4922	Fe II, He I	0.10	0.0	0.28	0.14	0.02	0.64	0.13	0.01	0.64
4959	[O III]	0.94	0.89	3.00	0.45	0.37	0.28	0.19	0.22	0.04
5007	[O III], Fe II, He I	2.00	1.62	6.42	1.18	0.82	5.76	0.89	0.67	2.15
5156	[Fe II], [Fe VII]	0.13	0.08	0.11	0.13	0.02	0.54	0.12	0.02	0.44
5755	[N II]	0.35	0.41	0.16	0.12	0.15	0.04	0.38	0.40	0.02
5876	He I	0.28	0.30	0.02	0.25	0.15	0.44	0.43	0.23	0.54
6086	[Fe VII], [Ca V]	0.13	0.30	1.28	...	...	...	...	...	...
6300	[O I], [S III]	0.26	0.48	2.15	...	...	...	0.15	0.04	0.54
6374	[Fe X]	0.17	0.02	1.0	0.21	0.04	1.28	...	...	...
6563	Hα	5.12	5.21	0.36	3.61	3.73	0.64	4.03	4.06	0.04
6678	He I	0.11	0.07	0.07	0.13	0.03	0.44	0.13	0.03	0.4
7065	He I	0.16	0.18	0.02	0.14	0.10	0.07	...	...	...
7155	[Fe II]	0.05	0.02	0.02	0.03	0.02	0.00	...	...	...
Total		...	...	19.44	...	...	14.69	...	...	15.24

An overall abundance values for RS Oph were calculated from the mean of these modelled results. The derived values show that helium, nitrogen, neon, iron and argon abundances are all enhanced relative to solar, while the oxygen and aluminium abundances are solar with respect to hydrogen, and silicon abundances are subsolar with respect to hydrogen. We note that calculation of abundance of silicon, argon and aluminium is based on one or two observed lines only. So, calculated abundance values may incorporate a significant error.

3.6 Summary

This is the first outburst of RS Oph which has revealed the complexity of emission mechanisms. This has been possible due to the wide spectral and temporal coverage of the observations. The evolution of the optical spectrum is very similar to previous outbursts. The emission line velocity evolution indicates that the remnant was in the adiabatic phase for a very brief period and quickly moved to the radiative cooling phase by $t \sim 5$ days. The nova remnant probably reached the edge of the red giant wind by ~ 80 days, as indicated by the marginal increase in the emission line velocity. These findings are consistent with those based on X-ray observations (Bode et al. 2006). The nebular lines originate in a region closer to the WD while the recombination lines originate in the decelerating material. The observed spectra and published data are modelled using the photoionization code CLOUDY for 11 epochs. Based on the modelling, the elemental abundances and other parameters such as the temperature and density of the ejecta, and the luminosity of the WD at the various epochs are estimated.

Chapter 4

Photoionization model grid of novae: estimation of physical parameters

4.1 Introduction

In this chapter, I will be discussing about the model grid of novae, which is generated using photoionization code CLOUDY to estimate the parameter values of the system. It is now well-known that all aspects of the nova outburst are manifested at various stages in the evolution of nova spectra. At the early stage (fireball phase), when the ionization levels are low, the spectrum is generally dominated by permitted, recombination lines of H I, He I, C I, O I, Fe I and N I. As the ejecta expands with time, density of the ejecta decreases and layers closer to the central ionizing source are revealed and degrees of excitation and ionization increase with time. Forbidden and high ionization emission lines are seen at this stage. For example, prominent lines of [Fe VI], [Fe VII], [Ca V], [Mn XIV] and [Si VI] are seen in coronal phase, whereas, lines of [Ne III], [O I], [Fe X], [Fe XIV], [Ca XV], [Ni XII] etc. are observed in nebular phase. As the nova approaches its post-outburst quiescence phase, the ionization levels decrease once again. Thus, study of observational properties of novae spectra may help to understand the properties of the system.

In a few previous studies, attempts have been made to explain observational properties in

different ways. For example, several authors have developed various models to generate observed characteristics such as light curves, characteristic times etc. Prialnik & Kovetz (1995) showed that the different characteristics of nova outbursts can be reproduced by varying the values of basic and independent parameters, e.g., the white dwarf mass (M_{WD}), the temperature of its isothermal core (T_{WD}), and the mass transfer rate ($\dot{M}$), and concluded that change of M_{WD} depends only on the mass transfer rate $\dot{M}$. They concluded that M_{WD} increases if $\dot{M} > 10^{-7}\ M_{\odot}\ \mathrm{yr}^{-1}$ and decreses if $\dot{M} < 10^{-9}\ M_{\odot}\ \mathrm{yr}^{-1}$, independently of the WD mass and temperature. The Chandrashekhar limit may be reached only at accretion rates in excess of $10^{-8}\ M_{\odot}\ \mathrm{yr}^{-1}$. Yaron et al. (2005) extended the parameter space and found the critical value for $\dot{M}$ to be $10^{-12.3}\ M_{\odot}\ \mathrm{yr}^{-1}$, below which TNR could not be triggered. Shara et al. (2010) used similar grid model for very luminous red novae considering CO WD with $M_{WD} = 0.5\ M_{\odot}$ and $T_{WD} = 2 - 4 \times 10^{6}$ K and showed how the nuclear luminosity vary over time. Hachisu & Kato (2006) calculated light curves of novae based on free-free emission from optically thin ejecta that dominates the continuum flux. They also calculated the luminosity which was obtained from the density structures outside the photosphere, using the optically thick wind model and successfully applied those results to well-observed novae. They derived an universal law of declination of light curve for classical novae, where the slope of flux (F) declines as $F \propto t^{-1.75}$ in the middle part ($\sim 2-6$ mag below the optical maximum) and as $F \propto t^{-3.5}$ in the later part ($\sim 6 - 10$ mag) (t is the time from the outburst in units of days). They showed that this break occurs due to a quick decrease in the wind mass-loss rate. Diaz (2001) used 3D shell models (RAINY 3D), built on the basis of photoionization code CLOUDY 94, to study the structure of inhomogeneous nova shells. Mass density distribution and the condensation effect were taken into account in order to calculate the thermal and photoionization equilibrium, radiation field and emitted spectrum from the inhomogeneous shell, and those model generated spectra were fitted with the observed line fluxes to calculate the thermal and photoionization equilibrium.

Hauschildt et al. (1995, 1996, 1997) generated synthetic spectra using stellar atmosphere code PHOENIX considering the basic parameters, e.g., effective temperature (T_{eff}), luminosity (L), density exponent (N), elemental abundances and used primary transitions to study the formation of spectral lines. The presence of optical and NIR molecular lines that form in the cooler region ($T_{eff} \sim 5000$ K) and multiple ionization stages of elements that form due to the presence of hotter region ($T_{eff} \sim 25000$ K), were explained theoretically. They further included transitions of Fe II to improve the fit to observed spectra. Later they modified the code to solve 3D NLTE problems, using the same physics as 1D modelling, for complex ions (Hauschildt & Baron 2014). In contrast, CLOUDY is an astrophysical plasma code that is designed to take an input SED (e.g., stars, AGN, etc.) and then calculate the resulting physical processes and spectrum as the radiation interacts with gas of known composition and geometry. Both CLOUDY and PHOENIX can be used to simulate 1D and 3D non-LTE models of Novae spectra. However, the photoionization code CLOUDY has a wider range of applicability with a larger atomic, molecular and chemical database. Therefore, CLOUDY has a potential to provide better results for novae system, where photoionization plays the most important role in generating the emission line spectra.

I have calculated simple grid models of novae using the photoionization code CLOUDY (version c17.00 rc1) (Ferland et al. 2017). Our aim is to investigate how the spectral emission line intensities change under different physical conditions and if the line ratios can be used to estimate the physical parameters from the observed spectra of novae. I would like to stress here that it is very difficult to get clues about these parameters directly from observations. In order to do so, a grid of 1792 models have been constructed for different set of parameters associated with novae systems, *viz.*, inner radius (R_{in}) of the ejected shell, thickness of ejected shell (ΔR), source temperature (T_{BB}), source luminosity (L) & H-density (n_H). For each set of parameters, spectra are generated over a wide range of wavelength, from ultraviolet to infrared. Next, the ratios of hydrogen

and helium line fluxes (relative to Hβ) which are prominently seen in novae spectra, have been calculated and a database has been generated. How these line ratios can be used to estimate the parameters associated with the system, e.g., T_{BB}, L, and n_H using information derived from observed spectra is explained. The modelling procedure is discussed in details in Section 4.2, results are discussed in Section 4.3 and summary and conclusions are given in Section 4.4.

4.2 Novae Grid Calculation

The grid model has been constructed using basic assumptions. I have considered here dust-free novae as most of the novae do not form dust. For the dust-forming novae, also, dust form after few weeks, when the temperatures of silicate and graphite grain go below their respective sublimation temperatures. Here I am primarily interested in novae characteristics in their early phase, where more observations are available. So, I have considered dust-free novae for the calculation. Further, to limit computational time and to set a basic abundances, I have restricted myself to solar metallicity as an average metallicity. It is possible that the model has limitations, as it is based on simple assumptions, yet I show that the method greatly aids in a reliable estimation of the novae parameters.

I have used the photoionization code, CLOUDY (version c17.00 rc1) (Ferland et al. 2017) (discussed in detail in Chapter 2), to generate synthetic spectra of several novae. CLOUDY is based on a self-consistent *ab-initio* calculation of the thermal, ionization, and chemical balance. It uses a minimum number of input parameters and generates output spectra or vice-versa (discussed in detail in Chapter 2). Previously, CLOUDY was used in determining elemental abundances and physical characteristics of few individual novae, such as LMC 1991 (Schwarz et al. 2001), QU Vul (Schwarz 2002), V1974Cyg

(Vanlandingham et al. 2005), V838 Her & V4160 Sgr (Schwarz et al. 2007a), V1186 Sco (Schwarz et al. 2007b), V1065 Cen (Helton et al. 2010) and RS Oph (Mondal et al. 2018, Das & Mondal 2015). Following a similar strategy, I plan to generate a grid of novae models to predict physical parameters constrained by observed hydrogen and helium line intensity ratios. For these novae grid models, I consider a spherically expanding ejecta illuminated by central WD. I assume the central source engine to be a blackbody with surface temperature T_{BB} (in K) and luminosity L (in erg s^{-1}). The calculations include the effects of important ionization (photo, Auger, collisional, charge transfer) and recombination processes (radiative, dielectronic, three-body recombination, charge transfer).

In addition to this, we assume that half of the radiation field emitted by the central object actually strikes the gas. Dimensions of spherical ejecta are defined by inner and outer radii (R_{in}, R_{out}), and the density of the ejecta is set by total hydrogen density given by

$$n(H) = n(H^0) + n(H^+) + 2n(H_2) + \sum_{other} n(H_{other}) cm^{-3},$$

where $n(H_{other})$ represents H in all other hydrogen-bearing molecules. Following Bath & Shaviv (1976), I assume a radius dependent power-law density profile with exponent α, ($n(R) \propto R^{\alpha}$), $n(R)$ being the density of the ejecta. Starrfield (1989) had argued that, for novae photospheres, the value of this exponent can only be -2 or -3. A constant mass loss rate and a constant velocity for the ejecta gives rise to a value of -2. However, I assume a constant mass loss rate together with a velocity proportional to the radius from the source. This gives rise to a value of -3 for the exponent, and I use this value in all my models calculated here.

Table 4.1: List of the parameters and range of their values considered for the grid model.

Parameters	Unit	Range	Step size
Inner Radius (R_{in})	cm	$13.5 \leq \log(R_{in}) \leq 15.0$	0.5
Thickness (ΔR)	cm	$13.5 \leq \log(\Delta R) \leq 15.0$	0.5
Temperature (T_{BB})	K	$4.5 \leq \log(T_{BB}) \leq 6.0$	0.5
Luminosity (L)	erg s^{-1}	$36.0 \leq \log(L) \leq 39.0$	1.0
H-density (n_H)	cm^{-3}	$6.0 \leq \log(n_H) \leq 12.0$	1.0

$$n(R) = n(R_{in}) \left(\frac{R}{R_{in}} \right)^{\alpha}.$$

Here, $n(R_{in})$ is the density at the illuminated face of the cloud at R_{in}. In previous calculations by various authors (e.g., Schwarz et al. 1997; Schwarz et al. 2007b; Helton et al. 2010; Schwarz 2002, etc.) the value of α was also chosen as -3. I consider a clumpy medium with the filling factor 0.1 and vary inner radius of the ejecta (R_{in}), thickness of ejecta (ΔR), temperature of the central source (T_{BB}), luminosity of the central source (L), and hydrogen density (n_H). All the models are calculated using solar metallicity.

A wide range of values for each of these above mentioned parameters are considered and the limiting values are chosen on the basis of the available observational results of various classical and recurrent novae in order to construct the grid model. For example, inner and outer radii are calculated by multiplying velocities (which can be calculated from the line-widths) with time and the thickness can be calculated by subtracting the inner radius from outer one. I have surveyed published works on novae to find limiting values of the parameters. Accordingly, the upper and lower limits of radii are determined considering high velocity of novae ejecta of 10,000 km/s (e.g., U Sco, Banerjee et al. 2010) and lower expanding value of 300 km/s (e.g., V723 Cas, Iijima 2006b). Since emission lines generally start to get resolved about a week after

outburst, in the present calculation we consider time from day 5 and calculate upto day 120 after outburst. On the basis of above values, the limiting values of $\log(R_{in})$ (in cm) and $\log(\Delta R)$ (in cm) are chosen as 13.5 and 15.0 with step-size 0.5. Similarly, I determine the limiting values of other parameters, namely, temperature, luminosity, and hydrogen density on the basis of available observational results. For temperature (T_{BB}) (in K) and luminosity (L) (in erg s^{-1}) of the ionizing source, I have considered $\log(T_{BB}) \in [4.5, 6.0]$ with step-size 0.5 and $\log(L) \in [36.0, 39.0]$ with step-size 1.0, respectively. Finally, I have taken $\log(n_H)$ (in cm^{-3}) $\in [6.0, 12.0]$ with step-size 1.0. Details of the parameter values are presented in tabular form in Table 4.1. The calculations stop at the thickness (ΔR) taken for a particular model. Thus a total of 1792 models were constructed by varying each of these parameters. The results i.e. ratio of line fluxes are arranged in 256 tables. These 256 tables of dataset are available at the website *https://aninditamondal1001.wixsite.com/researchworks* under the button "Novae Grid Data" on the page *Research/List-of-Documents*. Structure of the tables are briefly shown in Fig. 4.1.

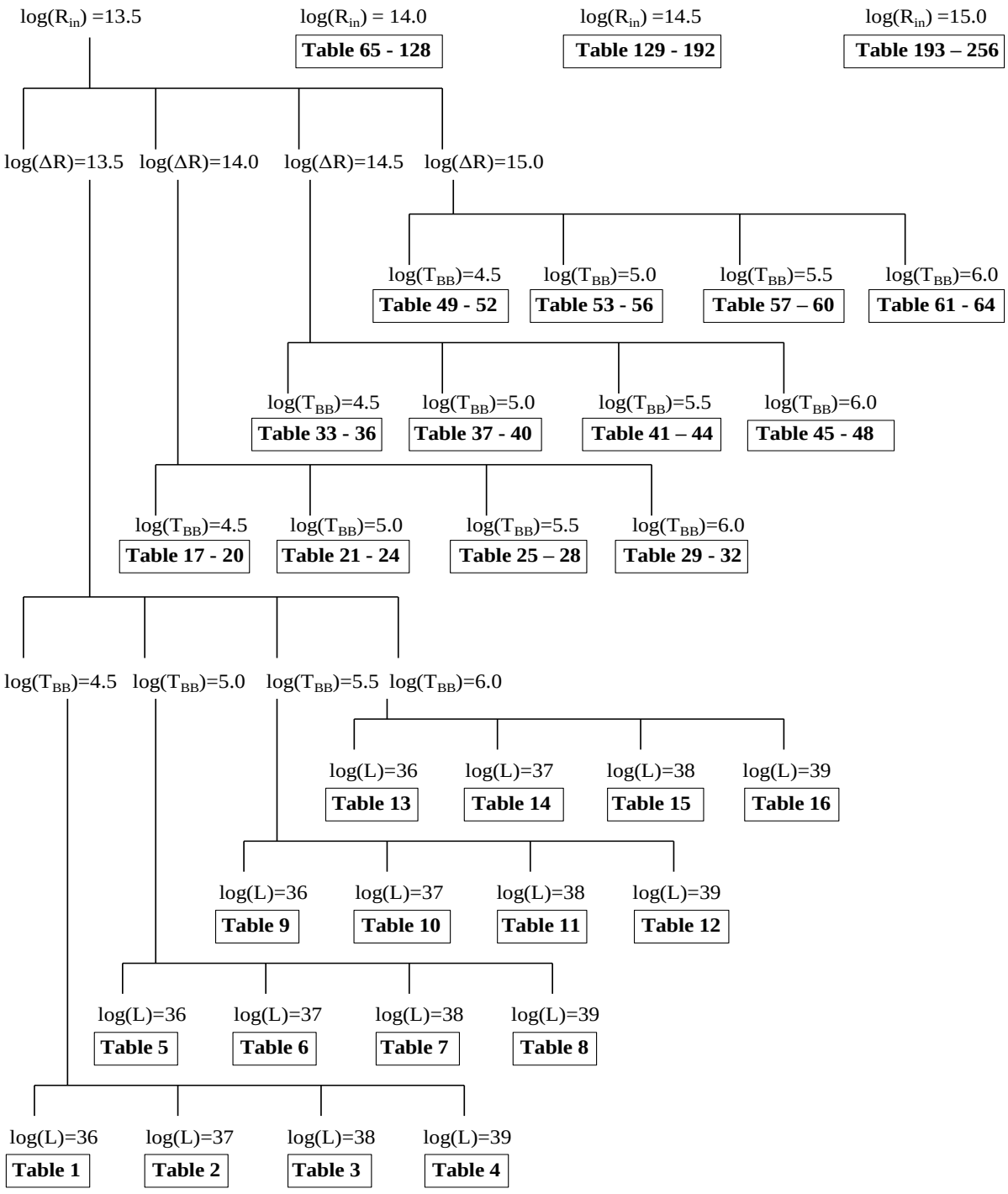

Figure 4.1: Schematic diagram of the structure of datasets of novae grid models. Each table contains data for $\log(n_H)$ = 6 - 12 [in cm^{-3}] with step size = 1. See section 4.2 & 4.3 for details.

Table 4.2: Normalized fluxes of hydrogen and helium emission lines w.r.t. Hβ for $\log(R_{in}) = 15.0$ (in cm), $\log(\Delta R) = 14.0$ (in cm), $\log(T_{BB}) = 5.5$ (in K), $\log(L) = 36$ (in erg s^{-1}), with $\log(n_H) = 6$ - 12 (in cm^{-3}) with step size = 1, corresponding to Table 217 of the database (see Fig. 4.1).

Line ID	Wavelength	$\log(n_H)$ [cm^{-3}]						
	λ (μm)	6	7	8	9	10	11	12
Ly C	0.0912	2.9190E+01	3.8110E+00	1.1920E-04	0.0000E+00	0.0000E+00	0.0000E+00	1.0110E-12
Ly 6	0.0938	4.2240E-01	1.0540E-02	8.6260E-04	8.2940E-04	9.0570E-04	9.0190E-04	9.8810E-04
Ly δ	0.0950	5.8950E-01	1.2230E-02	1.0530E-03	9.0530E-04	9.2350E-04	8.0760E-04	8.3480E-04
Ly γ	0.0973	7.2740E-01	1.2930E-02	1.6130E-03	1.2480E-03	1.1170E-03	8.8430E-04	7.7610E-04
Ly β	0.1026	1.0550E+00	1.7060E-02	3.5310E-03	3.0670E-03	2.5570E-03	1.8120E-03	1.3320E-03
Ly α	0.1216	6.7540E+01	6.1440E+01	1.1850E+02	1.2060E+02	1.0100E+02	7.6470E+01	5.3090E+01
H C	0.3646	1.6910E+00	1.4870E+00	1.3630E+00	1.3360E+00	1.2080E+00	9.4060E-01	6.7300E-01
H 7	0.3970	1.4510E-01	1.6930E-01	2.0370E-01	2.3040E-01	2.5220E-01	2.3080E-01	2.8630E-01
H δ	0.4102	2.4260E-01	2.6100E-01	3.0420E-01	3.3240E-01	3.5400E-01	3.8010E-01	4.0200E-01
H γ	0.4340	4.5850E-01	4.6670E-01	4.9190E-01	5.1650E-01	5.3250E-01	5.5070E-01	5.7270E-01
He I	0.4388	3.2860E-05	3.8380E-04	6.3160E-03	1.2510E-02	1.7170E-02	1.7270E-02	1.3040E-02
He I	0.4471	3.1270E-04	3.3640E-03	5.0270E-02	9.4240E-02	1.1710E-01	1.0480E-01	7.2410E-02
He II	0.4686	6.8820E-01	6.7630E-01	3.7720E-01	1.7450E-01	5.6540E-02	1.3110E-02	2.0670E-03
H β	0.4861	1.0000E+00	1.0000E+00	1.0000E+00	1.0000E+00	1.0000E+00	1.0000E+00	1.0000E+00
He I	0.5016	1.2640E-05	6.6130E-04	3.1700E-02	6.1880E-02	7.8150E-02	7.0440E-02	4.9750E-02
H α	0.6563	3.0620E+00	2.9570E+00	4.1380E+00	4.9410E+00	5.5690E+00	5.8580E+00	5.8720E+00
He I	0.6678	2.3330E-04	2.6540E-03	4.1060E-02	7.8710E-02	9.7380E-02	8.4280E-02	5.5030E-02
He I	0.7065	5.3470E-04	5.5940E-03	6.7980E-02	1.2850E-01	1.3610E-01	9.7780E-02	4.9230E-02
Pa C	0.8204	3.5220E-01	2.9580E-01	2.5590E-01	2.4380E-01	2.1670E-01	1.6840E-01	1.2060E-01

continued ...

Line ID	Wavelength	$\log(n_H)$ [cm^{-3}]						
	λ (μm)	6	7	8	9	10	11	12
Pa 9	0.9229	2.3490E-02	2.6460E-02	3.5670E-02	4.5440E-02	5.4750E-02	5.7910E-02	5.6870E-02
Pa 8	0.9546	3.2700E-02	3.6490E-02	4.7920E-02	5.8920E-02	7.0910E-02	7.7140E-02	7.7890E-02
Pa δ	1.0049	4.8790E-02	5.3080E-02	6.9660E-02	8.2540E-02	9.6060E-02	1.0620E-01	1.0710E-01
He I	1.0830	1.5530E-02	1.7610E-01	1.9340E+00	4.5530E+00	6.1130E+00	5.4110E+00	3.3060E+00
Pa γ	1.0938	8.1120E-02	8.3250E-02	1.1070E-01	1.2920E-01	1.4340E-01	1.4940E-01	1.5040E-01
He II	1.1627	3.4190E-02	3.3190E-02	1.5790E-02	7.1870E-03	2.4220E-03	5.9830E-04	1.0090E-04
He I	1.1969	1.3500E-05	1.5040E-04	2.3670E-03	4.5540E-03	6.0650E-03	6.1390E-03	5.0290E-03
He I	1.2527	1.1200E-05	1.2490E-04	2.3650E-03	4.1690E-03	4.1850E-03	2.9790E-03	1.6330E-03
Pa β	1.2818	1.3940E-01	1.4170E-01	1.9280E-01	2.2880E-01	2.5230E-01	2.5150E-01	2.4210E-01
Br 20	1.5192	1.4960E-03	2.1150E-03	3.4490E-03	4.5010E-03	4.9900E-03	4.7170E-03	3.7980E-03
Br 19	1.5260	1.7180E-03	2.3770E-03	3.9180E-03	5.1640E-03	5.7750E-03	5.4910E-03	4.4410E-03
Br 18	1.5342	1.9930E-03	2.6890E-03	4.4630E-03	5.9460E-03	6.7180E-03	6.4340E-03	5.2330E-03
Br 17	1.5439	2.3350E-03	3.0680E-03	5.0950E-03	6.8670E-03	7.8520E-03	7.5870E-03	6.2150E-03
Br 16	1.5556	2.7680E-03	3.5450E-03	5.8320E-03	7.9500E-03	9.2170E-03	9.0030E-03	7.4390E-03
Br 15	1.5701	3.3260E-03	4.1590E-03	6.7000E-03	9.2230E-03	1.0860E-02	1.0740E-02	8.9730E-03
Br 14	1.5880	4.0580E-03	4.9650E-03	7.7390E-03	1.0730E-02	1.2830E-02	1.2890E-02	1.0890E-02
Br 13	1.6109	5.0410E-03	6.0400E-03	9.0360E-03	1.2540E-02	1.5190E-02	1.5520E-02	1.3280E-02
Br 12	1.6407	6.3920E-03	7.5050E-03	1.0760E-02	1.4790E-02	1.8010E-02	1.8700E-02	1.6190E-02
Br 11	1.6806	8.3030E-03	9.5620E-03	1.3180E-02	1.7700E-02	2.1390E-02	2.2520E-02	1.9680E-02

continued ...

Line ID	Wavelength	$\log(n_H)$ $[\mathrm{cm}^{-3}]$						
	λ (μm)	6	7	8	9	10	11	12
He I	1.7003	2.2110E-05	2.3790E-04	3.5560E-03	6.6670E-03	8.2830E-03	7.4150E-03	5.3760E-03
Br 10	1.7362	7.6950E-03	8.7790E-03	1.2330E-02	1.5620E-02	1.8300E-02	1.8710E-02	1.8320E-02
Br 9	1.8174	1.0450E-02	1.1330E-02	1.5200E-02	1.9340E-02	2.3300E-02	2.4640E-02	2.4920E-02
Pa α	1.8751	2.8440E-01	2.7860E-01	4.1780E-01	5.1640E-01	5.7850E-01	5.7250E-01	5.3670E-01
Br δ	1.9446	1.4910E-02	1.5680E-02	2.0380E-02	2.4990E-02	3.0050E-02	3.2680E-02	3.3900E-02
He I	2.0581	7.0750E-07	1.7650E-04	4.1300E-02	1.2850E-01	2.3440E-01	2.6670E-01	1.9320E-01
He I	2.1130	2.7780E-06	2.9060E-05	3.8350E-04	6.8760E-04	7.6670E-04	5.8670E-04	3.4470E-04
Br γ	2.1655	2.2750E-02	2.3090E-02	2.9590E-02	3.4830E-02	4.0430E-02	4.4670E-02	4.6070E-02
Br β	2.6252	3.8300E-02	3.6890E-02	4.6910E-02	5.3890E-02	5.9490E-02	6.1790E-02	6.3500E-02
Pf 10	3.0384	4.0130E-03	4.5100E-03	6.3250E-03	8.0140E-03	9.3860E-03	9.5950E-03	9.3460E-03
Pf 9	3.2961	5.5080E-03	5.8080E-03	7.7740E-03	9.8810E-03	1.1900E-02	1.2580E-02	1.2640E-02
Pf γ	3.7400	7.9990E-03	8.0270E-03	1.0360E-02	1.2680E-02	1.5240E-02	1.6560E-02	1.7150E-02
Br α	4.0512	6.3160E-02	5.9880E-02	7.7720E-02	9.0410E-02	9.8890E-02	9.8270E-02	9.6580E-02
Pf β	4.6525	1.2430E-02	1.1780E-02	1.4840E-02	1.7390E-02	2.0160E-02	2.2250E-02	2.3070E-02
Hu γ	5.9066	3.2200E-03	3.3250E-03	4.4410E-03	5.6420E-03	6.7920E-03	7.1820E-03	7.2460E-03
Pf α	7.4578	2.1030E-02	1.8280E-02	2.2390E-02	2.5420E-02	2.7950E-02	2.8990E-02	3.0160E-02
Hu β	7.5004	4.7050E-03	4.5330E-03	5.8230E-03	7.1170E-03	8.5480E-03	9.2910E-03	9.6840E-03
Hu α	12.3685	7.2340E-03	6.3200E-03	7.8650E-03	9.1900E-03	1.0640E-02	1.1740E-02	1.2300E-02

4.3 Results

From the model generated spectra, I have calculated the fluxes of fifty-six hydrogen and helium recombination lines which are generally seen prominently in novae emission spectra, covering a wide wavelength region. As an example, I present the results of such a model for $\log(R_{in}) = 15.0$ (in cm), $\log(\Delta R) = 14.0$ (in cm), $\log(T_{BB}) = 5.5$ (in K) and $\log(L) = 36$ (in erg s^{-1}) in Table 4.2 (corresponding to Table 217 of database). Line fluxes have been calculated for 7 different values of $\log(n_H)$ (in cm^{-3}) (i.e. for $n_H = 10^6, 10^7, 10^8, 10^9, 10^{10}, 10^{11}$ and 10^{12}). Contours of line flux ratios (along z-axis) can be plotted against any two parameters (among T_{BB}, L and n_H) along x and y-axes, keeping the other one fixed. A typical contour plot of Hα line flux ratio is shown in Fig. 4.2, with $\log(L)$ along the x-axis and $\log(n_H)$ along the y-axis, for $\log(R_{in}) = 15.0$ (in cm), $\log(\Delta R) = 14.0$ (in cm), and $\log(T_{BB}) = 5.5$ (in K), corresponding to the Tables 217 - 220 of the database (see Fig. 4.1 and Table 4.2). The values of line flux ratios of Hα w.r.t. Hβ are mentioned on the contours.

As mentioned earlier in section 4.2, R_{in} and ΔR could be calculated from line-widths and time elapsed after outburst; T_{BB} could be obtained by blackbody fitting with the continuum of the observed spectra and line fluxes could be measured from the observed spectra. Once, the values of R_{in}, ΔR, and T_{BB} are found, we can choose the corresponding dataset from the database and make contour plots for different lines, e.g., Hα, Hγ, Hδ etc. Now, from these contour plots we can extract (e.g., Fig. 4.2) the contours for the corresponding values of the line ratios and plot them together (e.g., Fig. 4.3). From the intersection of the contours of different lines, we can determine the values of the parameters *viz.*, L and n_H (in case of Fig. 4.3). In this way, by knowing the value of any one of L, n_H, and T_{BB}, values of the other two could be determined.

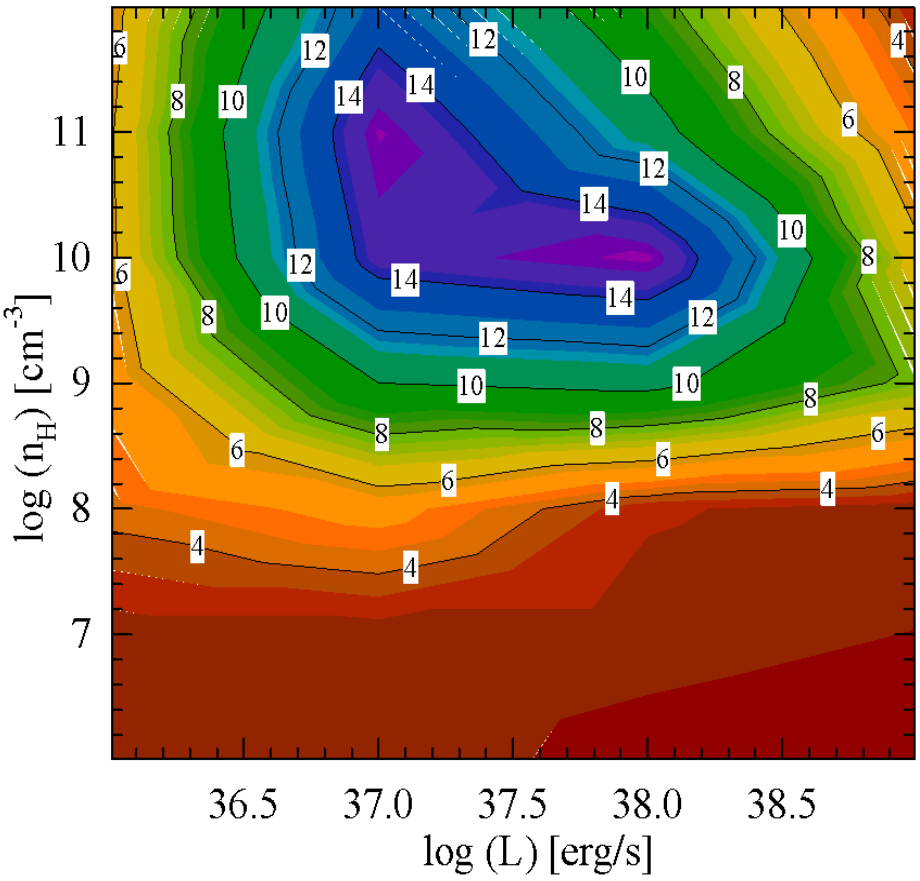

Figure 4.2: Contour plot of Hα line flux ratio w.r.t. Hβ for $\log(R_{in})$ = 15.0 (in cm), $\log(\Delta R)$ = 14.0 (in cm), and $\log(T_{BB})$ = 5.5 (in K); $\log(L)$ (in erg s^{-1}) and $\log(n_H)$ (in cm^{-3}) are plotted along x and y-axes respectively, corresponding to the Tables 217 - 220 of database (see Fig. 4.1). The values of Hα/Hβ are mentioned on each contour. See section 4.3 for more details.

Table 4.3: Comparison of estimated parameter values of few novae obtained from grid model with previously calculated results (shown in paranthesis).

Novae (Outburst)	Line flux ratio from literature	Ref.	Estimated values (previously calculated values)				
			$\log(R_{in})$ [in cm]	$\log(\Delta R)$ [in cm]	$\log(T_{BB})$ [in K]	$\log(L)$ [in erg s^{-1}]	$\log(n_H)$ [in cm^{-3}]
RS Oph (2006)	Hα/Hβ = 6.12, Hγ/Hβ = 0.39, Hδ/Hβ = 0.28, Hϵ/Hβ = 0.29	1	14.0 (14.0[1])	14.0 (14.05[1])	4.5 (4.5[1])	36.65 (36.8[1])	10.2 (10.5[1])
V1065 Cen (2007)	Hα/Hβ = 3.89, Hγ/Hβ = 0.48, Paγ/Paβ = 0.61	2	15.0 (15.16[2])	15.0 (15.02[2])	5.0 (4.77[2])	38.0 (38.05[2])	7.5 (7.52[2])
V1186 Sco (2004)	Hγ/Hβ = 0.38, Hδ/Hβ = 0.24, Paγ/Paβ = 0.57, Huγ/Huα = 0.65, He I (1.083 μm)/Paβ = 12.14	3	15.0 (15.04[3])	15.0 (15.15[3])	4.5 (4.7[3])	36.8 (36.8[3])	7.5 (7.5[3])
V1974 Cyg (1992)	Hα/Hβ = 2.93, Hγ/Hβ = 0.42	4	15.0 (15.3[4])	15.0 (15.4[4])	5.5 (5.52[4])	38.0 (38.06[4])	8.0 (7.8[4])
PW Vul (1984)	Hα/Hβ = 4.4, Hγ/Hβ = 0.37, He II (4686 $\AA$)/Hβ = 0.34	5	15.0 (15.25[5])	15.0 (15.5[5])	5.5 (5.4[5])	37.7 (37.8[5])	7.1 (7.04[5])

[1]Mondal et al. 2018, Das & Mondal 2015; [2]Helton et al. 2010; [3]Schwarz et al. 2007b; [4]Vanlandingham et al. 2005; [5]Schwarz et al. 1997.

To check if this method works well, I apply this method to few novae. First, I consider the example of RS Ophiuchi (RS Oph), which is a well-known recurrent nova (recurrence period $\sim$ 20 years). From the optical spectra taken 12 days after outburst (2006) with 2m Himalayan Chandra Telescope (HCT), I have calculated the temperature as $10^{4.5}$ K and the line flux ratio of Hα, Hγ, Hδ & Hϵ w.r.t. Hβ as 6.12, 0.39, 0.28 & 0.29 respectively (Mondal et al. 2018). From the expansion velocities of the ejecta (see section 3.1.2) I have calculated R_{in} and ΔR. For this particular set of R_{in}, ΔR, and T_{BB} I have plotted contours for the hydrogen lines with L and n_H along x and y-axes. I have extracted the contours for the corresponding values of the line ratios and have plotted them together (Fig. 4.3). From the figure, I find that all lines intersect at log(L) = 36.65 (in erg s^{-1}) and log(n_H) = 10.2 (in cm^{-3}). These values are consistent with previous results of RS Oph (see Table 4.3).

I also run a seperate CLOUDY model for RS Oph considering the derived parameter values and have generated synthetic spectrum keeping the abundances as solar. The simulated spectra was then compared with the observed one taken in 2m HCT, in the optical region. In Fig. 4.4, the observed spectra is shown in solid black line and the simulated spectra is shown in dashed red line. It is clearly seen that the observed hydrogen features are matching well with the modelled hydrogen lines. This, alternatively, validate the method of estimating parameters.

In a similar way, we have also tested the grid model for other galactic classical novae, e.g., V1065 Cen, V1186 Sco, V1974 Cyg and PW Vul to determine the physical parameters. For novae RS Oph, V1065 Cen, and V1974 Cyg, I could estimate the parameter values using only hydrogen lines. But, in case of novae V1186 Sco and PW Vul, contours of hydrogen lines (optical, NIR and FIR) intersected at multiple points. So, I use the He I 1.083 μm line (for V1186 Sco) and He II 4686 $\AA$ line (for PW Vul) which are strong in the spectra, along with other hydrogen lines to estimate the parameters.

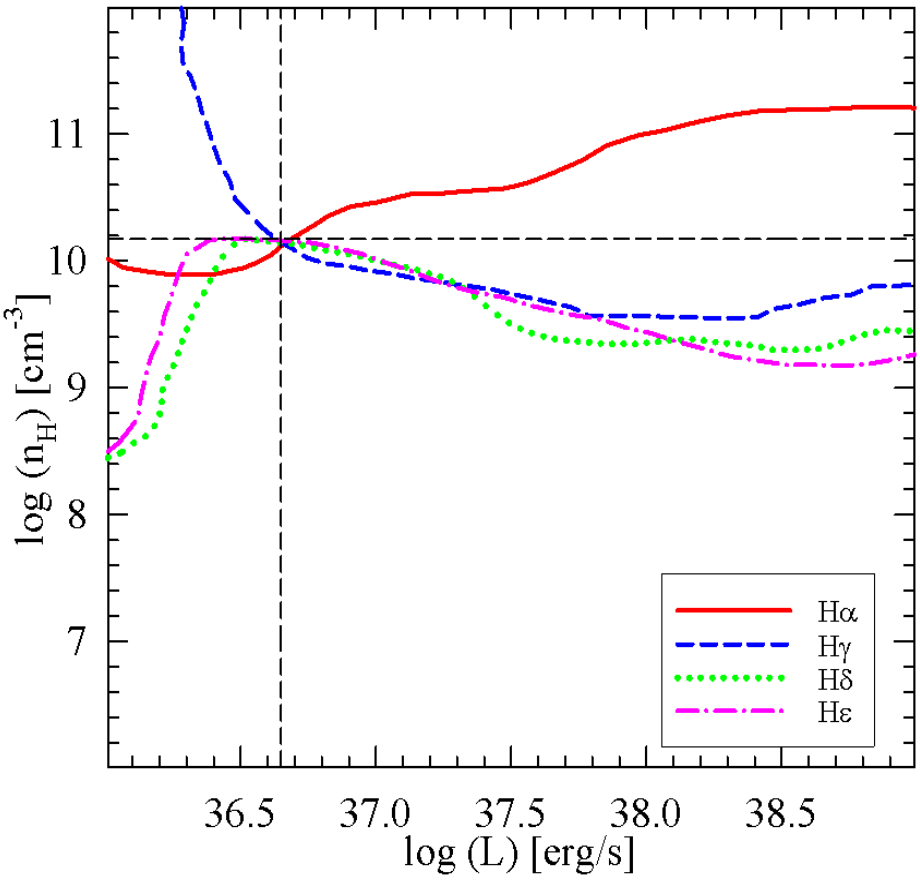

Figure 4.3: Plots of different extracted contour lines for nova RS Oph, 12 days after outburst. The red solid, blue short dashed, green dotted, and pink dotted dashed lines represent the extracted plots of line flux ratios of Hα, Hγ, Hδ & Hϵ respectively w.r.t. Hβ. The lines intersect at $\log(L) = 36.65$ (in erg s^{-1}) and $\log(n_H) = 10.2$ (in cm^{-3}). See section 4.3 for more details.

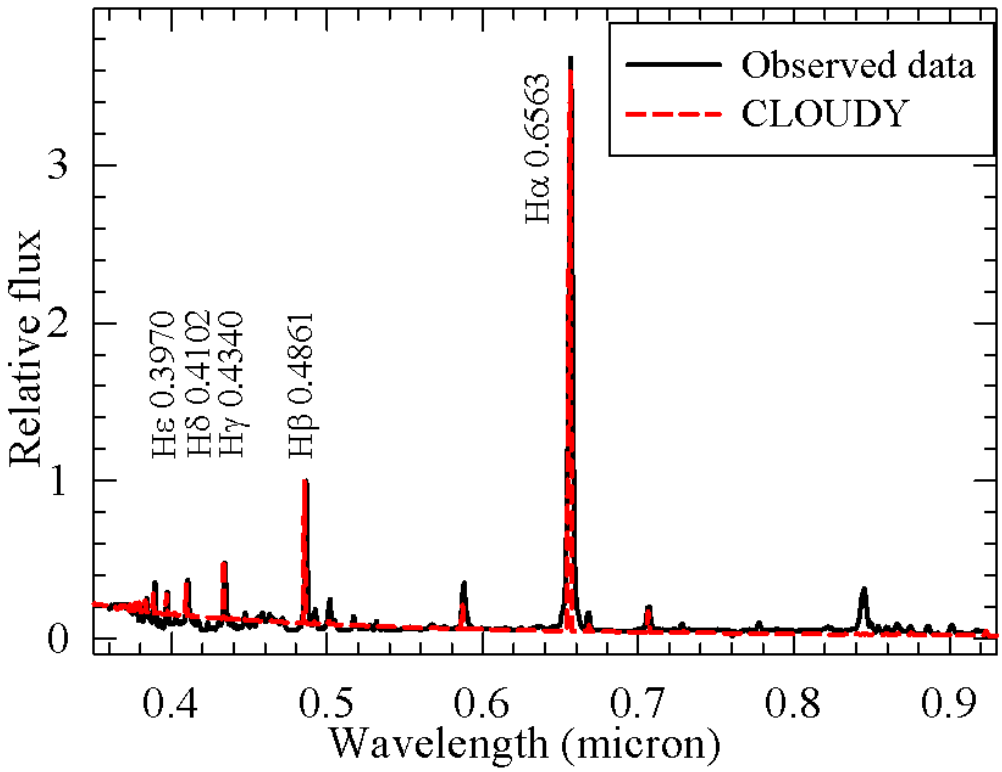

Figure 4.4: Comparison of observed (solid black) and CLOUDY generated (dashed red) spectra of nova RS Oph. Prominent hydrogen features are marked. See section 4.3 for more details.

It may be mentioned here that from previous studies, we find the He abundances w.r.t. solar as 1.1 ± 0.3 in case of V1186 Sco (Schwarz et al. 2007b) and 1.0 ± 0.4 in case of PW Vul (Schwarz et al. 1997), which are near to solar values. So, there are no significant changes in the intensities of He lines and use of these lines are quite safe to estimate the parameters. The results match well with the previously calculated results; the results are shown in Table 4.3. These results validate the method and motivate me to apply this to few other novae and estimate the physical parameter values.

(i) **Nova KT Eridin (KT Eri)**: this is a well known galactic classical nova, discovered by K. Itagaki on 2009 November 25.5 UT (Yamaoka et al. 2009). The maximum and minimum velocities of the ejecta are determined as V_{max} = 3600 km/s, V_{min} = 1900 km/s respectively, from the broad Balmer emission features (Maehara, Arai & Isogai 2009). From the SMARTS spectroscopic data (Walter et al. 2012), taken 12 days after outburst, I have calculated $T_{BB} = 10^5$ K. The line flux ratio of Hα and Hγ w.r.t. Hβ are measured as 2.87 and 0.78 respectively. Using the values in the database, I have plotted the contours for the hydrogen lines for the particular set of R_{in}, ΔR, and T_{BB}. Then I have extracted contours for the observed line fluxes together (Fig. 4.5) and from the intersection of the lines, I have estimated $\log(L)$ = 38.5 (in erg s^{-1}) & $\log(n_H)$ = 9.2 (in cm^{-3}).

(ii) **V5558 Sagittarii (V5558 Sgr)**: this nova was discovered on 2007 April 14.77 UT. The R_{in} and ΔR on 24 days after outburst are calculated using the minimum (V_{min} = 250 km/s) and maximum (V_{max} = 540 km/s) expansion velocities of the ejecta (Iijima 2007a, 2007b). From the continuum of the optical spectra, I have measured the temperature to be 10^6 K. I have calculated the line flux ratio of Hγ and Hδ w.r.t. Hβ and Paβ w.r.t. Paγ from the spectra taken in the optical (Tanaka et al. 2011) and

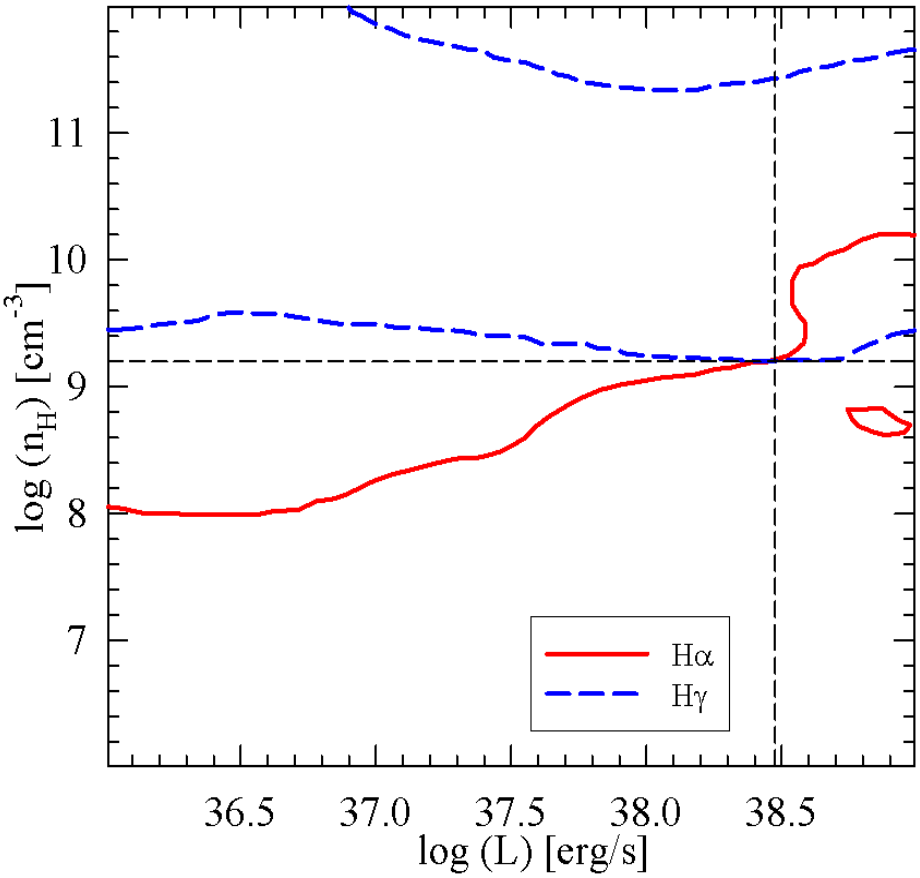

Figure 4.5: Plots of different extracted contour lines of nova KT Eri, 12 days after outburst. The red solid and blue dashed lines represent the extraccted plots of line flux ratios of Hα and Hγ respectively w.r.t. Hβ. The lines intersect at $\log(L) = 38.5$ (in erg s^{-1}) and $\log(n_H) = 9.2$ (in cm^{-3}). See section 4.3 for more details.

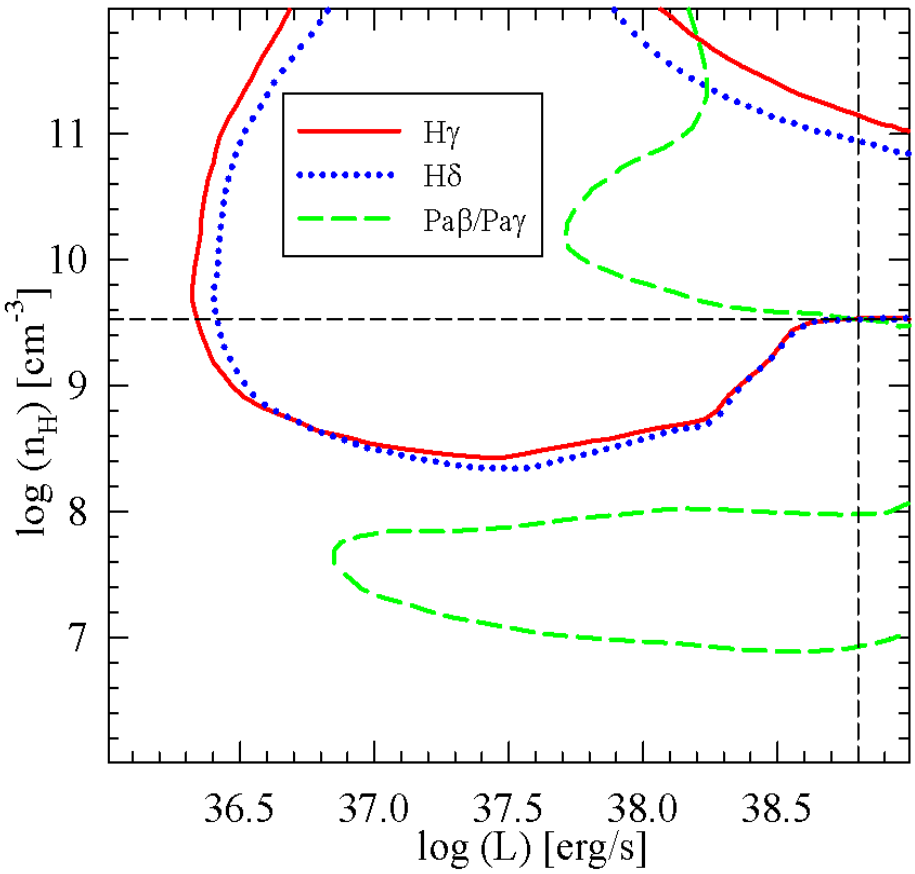

Figure 4.6: Plots of different extracted contour lines of nova V5558 Sgr, 24 days after outburst. The red solid and blue dotted lines represent the extracted plots of line flux ratios of Hγ and Hδ respectively w.r.t. Hβ and the green dashed line represents the extracted plots of line flux ratios of Paβ w.r.t. Paγ. The lines intersect at $\log(L) = 38.8$ (in erg s^{-1}) and $\log(n_H) = 9.5$ (in cm^{-3}). See section 4.3 for more details.

near-infrared region (Das et al. 2015) respectively. I have then plotted the corresponding contours from the database. Then I have extracted the contours for the observed line ratios and have plotted them together (Fig. 4.6). From the intersection of the extracted contours for the observed line ratios, I estimate $L = 6.4 \times 10^{38}$ erg s^{-1} and $n_H = 3.4 \times 10^9$ cm^{-3}. This example also shows that lines at other wavelength region may help sometimes to determine the values more precisely. A more detailed study of this nova using CLOUDY is under progress and will appear in a seperate paper in future.

(iii) **U Scorpii (U Sco)**: the recurrent nova U Sco explodes at intervals of 10 $\pm$ 2 years; it's recent outburst occured on Jan 28, 2010 (Schaefer et al. 2010). From the optical spectra taken on about 6 days after outburst, maximun velocity was calculated from the He I 7065 Åline as $\sim$ 9900 km/s whereas minimun velocity was calculated as $\sim$ 3786 km/s from the hydrogen lines (Anupama et al. 2013). During the early phase, effective tempertaure was measured as 2×10^4 K and electron density as $10^{7.8}$ cm^{-3} (Anupama et al. 2013). Line fluxes of Hα, Hγ, and Hδ w.r.t. Hβ are measured as 2.45, 0.72 and 0.38. Then following the similar method, from extracted contour plots (Fig. 4.7), I have estimated $n_H = 10^8$ cm^{-3} and $L = 10^{37.8}$ erg s^{-1}, which match well with the previously obtained results (see Table 4.4).

(iv) **V339 Delphini (V339 Del)**: On 14.584 August, 2013, Koichi Itagaki discovered classical nova Delphini 2013 (V339 Del) at 6.8 optical magnitude (Nakamo et al. 2013). Burlak et al. (2015) calculated the luminosity of the system as $10^{38.39}$ erg s^{-1} from the early phase spectrum and the expansion velocity was calculated in the range of 1000 - 1800 km/s from the Hα emission lines. I have measured the Balmer line flux ratios from the spectra taken on 21 days after the outburst as Hα/Hβ = 6.34 and Hγ/Hβ = 0.34. Here, I have drawn the contour plots of hydrogen line flux ratios with T_{BB} and n_H along

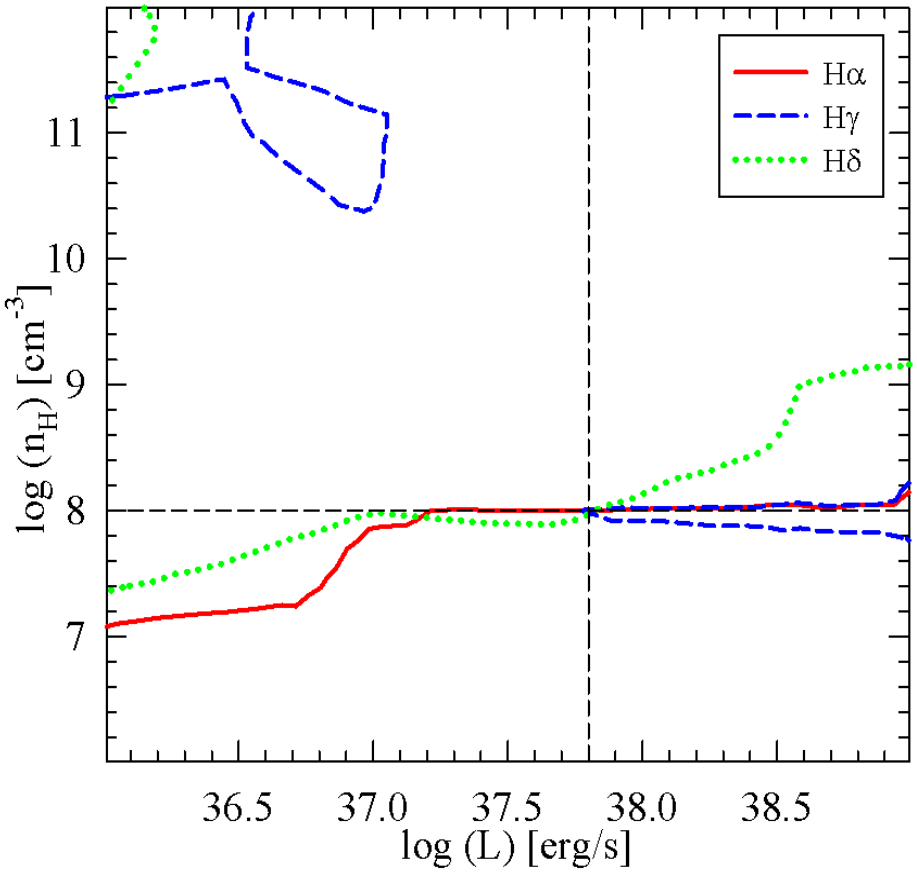

Figure 4.7: Plots of different extracted contour lines of nova U Sco, 5.81 days after outburst. The red solid, blue short dashed, and green dotted lines represent the extracted plots of line flux ratios of Hα, Hγ, & Hδ respectively w.r.t. Hβ. The lines intersect at $\log(L) = 37.8$ (in erg s^{-1}) and $\log(n_H) = 8.0$ (in cm^{-3}). See section 4.3 for more details.

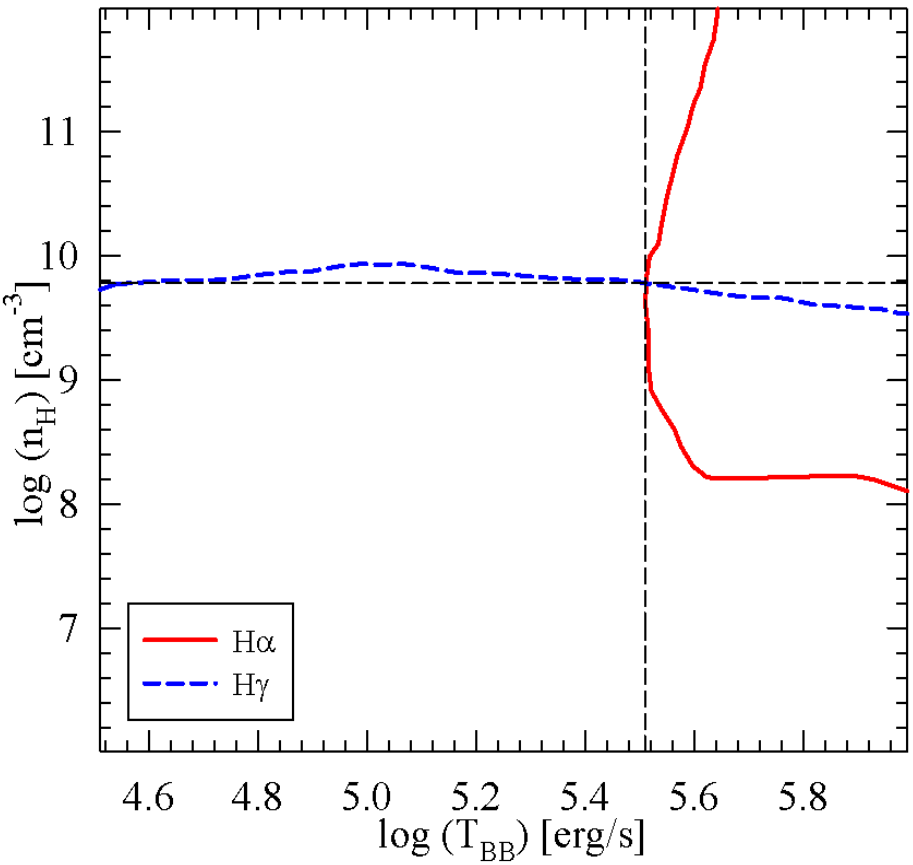

Figure 4.8: Plots of different extracted contour lines of nova V339 Del, 21 days after outburst. The red solid and blue dashed lines represent the contour plots of line flux ratio of Hα and Hγ respectively w.r.t. Hβ. The lines intersect at $\log(T_{BB}) = 5.51$ (in K) and $\log(n_H) = 9.78$ (in cm^{-3}). See section 4.3 for more details.

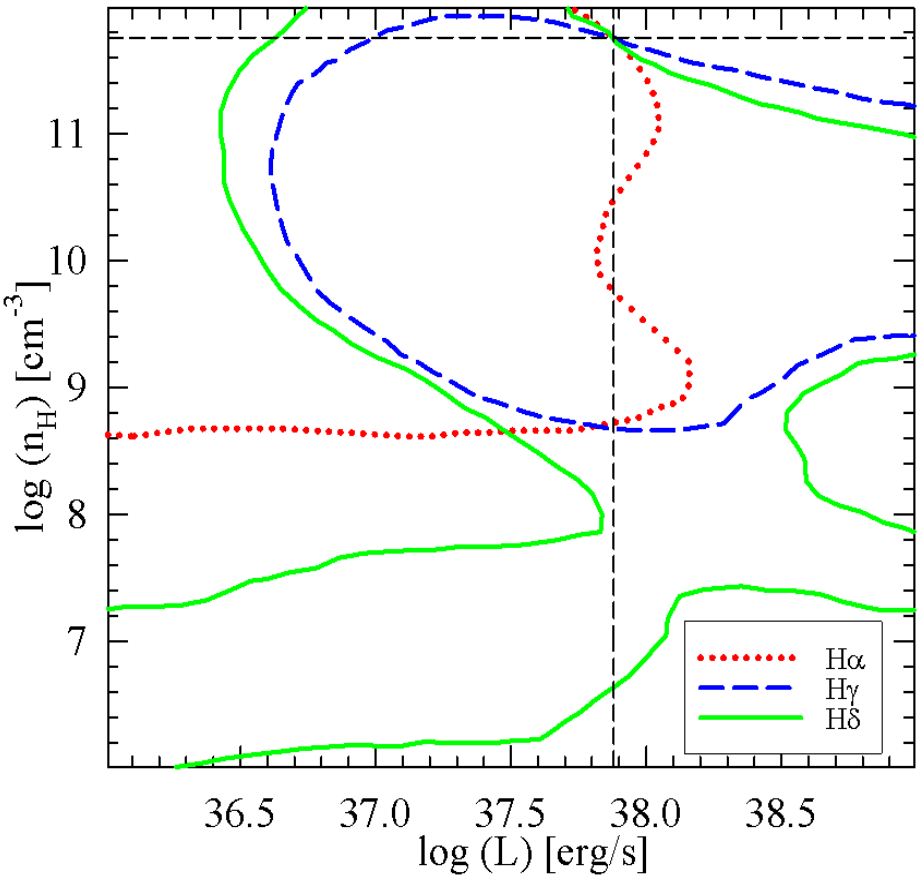

Figure 4.9: Plots of different extracted contour lines of nova 2015 of dwarf galaxy IC1613. 26 days after ouburst. The red dotted, blue dashed, and green solid lines represent the extracted plots of line flux ratios of Hα, Hγ, & Hδ respectively w.r.t. Hβ. The results are $\log(L) = 37.9$ (in erg s^{-1}) and $\log(n_H) = 8.7$ (in cm^{-3}). See section 4.3 for more details.

x and y-axes respectively (Fig. 4.8). The lines intersect at $\log(T_{BB}) = 5.51$ (in K) and $\log(n_H) = 9.78$ (in cm^{-3}), which give the values of T_{BB} and n_H respectively.

Table 4.4: Estimated parameter values of few novae obtained from CLOUDY grid model.

Novae	Outburst	Line Flux Ratios	References	$\log(R_{in})$ [in cm]	$\log(\Delta R)$ [in cm]	$\log(T_{BB})$ [in K]	$\log(L)$ [in erg s^{-1}]	$\log(n_H)$ [in cm^{-3}]
KT Eri	2009	Hα/Hβ = 2.87, Hγ/Hβ = 0.78	1	14.0	14.0	5.0	38.5	9.2
V5558 Sgr	2007	Hγ/Hβ = 0.52, Hδ/Hβ = 0.20, Paβ/Paγ = 1.14	2	14.5	14.5	6.0	38.8	9.53
U Sco	2010	Hα/Hβ = 2.45, Hγ/Hβ = 0.72, Hδ/Hβ = 0.38	3	14.5	14.5	4.5	37.8	8.0
V339 Del	2013	Hα/Hβ = 6.34, Hγ/Hβ = 0.34	4	14.5	14.0	5.51	38.0	9.78
Nova IC1613 2015	2015	Hα/Hβ = 7.47, Hγ/Hβ = 0.40, Hδ/Hβ = 0.35	5	14.5	14.0	6.0	37.9	11.7

[1]Walter et al. 2012; [2]Tanaka et al. 2011, Das et al. 2015; [3]Anupama et al. 2013 ; [4]Gherase et al. 2015, Burlak et al. 2015; [5]Williams et al. 2017.

(v) **IC 1613 #2015**: this is an extra-galactic classical nova in dwarf galaxy IC 1613 discovered on 2015 September 10. The V_{max} and V_{min} were calculated from Hα emission line and Hγ absorption line as $\sim$ 1750 km/s and 1200 km/s respectively (Williams et al. 2017). From the *Swift* X-rays studies, temperature and luminosity of the source were determined to be $T_{BB} = 10^{5.76}$ K and $L = 10^{37.7}$ erg s^{-1} (Williams et al. 2017). I have used the line flux ratio of Hα, Hγ and Hδ w.r.t. Hβ measured 26 days after outburst to find the values of other observables. The extracted contours of the line flux ratios from the grid database gives $\log(L) = 37.9$ (in erg s^{-1}), which matches well with $L = 10^{37.7}$ erg s^{-1} from the X-ray study, and $\log(n_H) = 11.7$ (in cn^{-3}). The plot is shown in Fig. 4.9 and the parameter values are shown in Table 4.4 in more detail.

4.4 Summary & Discussions

I have computed grid models of novae using photoionization code CLOUDY (Ferland et al. 2017). The aim of this paper has been to generate an extended five-dimensional parameter space for dust-free novae by varying hydrogen density, inner radius and thickness of the novae ejecta, temperature, and luminosity of the ionizing source in commensurate with an observed range. From the model generated synthetic spectra I have calculated line intensities of 56 hydrogen and helium lines which are generally observed prominently in novae spectra, spanning over a wide range of wavelengths: from ultraviolet to infrared.

Simulated hydrogen and helium line intensities from the model grid can be compared with observations and physical parameters like T_{BB}, L, and n_H can be inferred. To test the robustness of the calculations, I have cross-checked predictions from the grid results for few novae e.g., RS Oph, V1065 Cen, V1974 Cyg, V1186 Sco and PW Vul with published data and they matched well. I also have estimated density and lumi-

nosity of 5 other novae, one of which is an extragalactic nova. I have demonstrated that these grid models work fine. This gives me confidence that this will work successfully. However, there are few scopes to improve them and I discuss those in the following.

I have considered here dust-free environment because from observations, it has been found that most of the novae do not form dust. Measurements of fluxes of spectral lines in post dust formation phase may not yield proper results. So, cautions should be taken while measuring the line fluxes. I plan to incorporate dust in this model and check the effect of dust on the line intensities. Also, in the present calculation, I used solar abundance to limit the computational time. If abundances of other elements are increased or decreased, hydrogen line intensities may get changed. To check this, I have constructed a few models with higher metallicity (2, 2.5 and 3 times solar metallicity) and found that variation in hydrogen line intensities are less than 15%. I am in a process to extend the database with results for different metallicities in future.

In the present calculation, I have not incorporated errors associated with the measurements of the values of observables to keep this model simple. To check how the errors affect the results, I have considered $\pm 5\%$ error associated with observed line fluxes for nova V5558 Sgr and shown the result in linear scale in Fig. 4.10. I have also checked in log scale that the curves do not intersect at any other points even after inclusion of the error margins. From Fig. 4.10, I find the modified results as $L = (6.1 - 6.8) \times 10^{38}$ erg s^{-1} and $n_H = (3.2 - 3.4) \times 10^9$ cm^{-3}. These are in-line with the previous results of $L = (6.4 \pm 0.4) \times 10^{38} ergs^{-1}$ and $n_H = (3.4 \pm 0.2) \times 10^9 cm^{-3}$. Thus the uncertainties are less ($\sim 6.25\%$ in case of L and $\sim 5.8\%$ in case of n_H), which ensures the applicability of the method. If uncertainties in the observables increase, the results will also become more uncertain. So, cautions should be taken while choosing the emission lines. It is suggested to consider strong emission lines (e.g., Hα, Hβ, Hγ, Paα, Paβ, Paγ, Brγ etc.) to reduce the error during measurements.

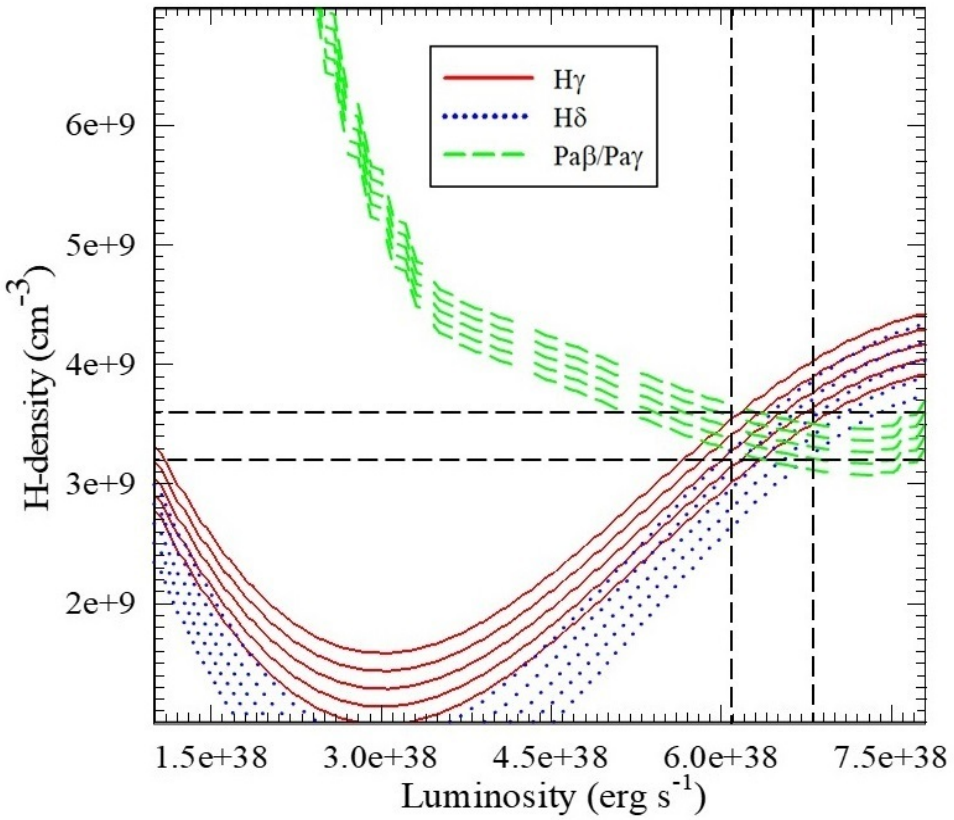

Figure 4.10: Plot of different extracted contour lines of nova V5558 Sgr, 24 days after outburst, incorporating 5% error for observed flux values. The red solid and blue dotted lines represent the extracted plots of line flux ratios of Hγ and Hδ respectively w.r.t. Hβ and the green dashed line represents the extracted plots of line flux ratios of Paβ w.r.t. Paγ. The lines intersect between $L = (6.1-6.8)\times10^{38}$ erg s^{-1} and $n_H = (3.2-3.4)\times10^9$ cm^{-3}. See section 4.4 for more details.

The nature of the contours depend on the line ratios, and line intensity vary from novae to novae. In few cases, degeneracy may appear i.e. more than one countours may follow the same locus or have multiple intersections. For example in Fig. 4.6, the curves nearly intersect around $\log(L) = 38.2$ [in erg s^{-1}] and $\log(n_H) = 11.5$ [in cm^{-3}] in addition to intersection at $\log(L) = 38.8$ [in erg s^{-1}] and $\log(n_H) = 9.5$ [in cm^{-3}]. In such cases, results obtained from other calculations may help to estimate the parameter values. Also, more emission lines/observables available, may be used to ensure that we do not get any other intersections. It is suggested to consider strong emission lines (Hα, Hβ, Hγ, Paα, Paβ, Paγ, Brγ etc.) with higher flux ratios as they include less instrumentation errors during measurements. Generally the degeneracy do not increase while considering more observables. In such case, we should take emission lines of other elements (e.g., He line for nova V1186 Sco) also.

If we take the line ratios w.r.t. other lines instead of Hβ, shapes of the contours will be different and degeneracy may not occur. As we understand from the plots, strong lines like the lower members of the hydrogen series have a less tendency to be degenerate. So, multi-wavelength observations would be useful in such cases. If there are multiple intersections, results obtained from other calculations may help to estimate the parameter values. We should use as many emission lines/observables available to make sure that multiple intersections do not occur. If no intersection is found, a range of the values could be estimated.

All of the models presented here are one-dimensional and radiation from central source has been approximated by a black body radiation. It would be interesting to study how the advanced stellar atmospheres instead of the simple black body radiation could affect results. In future, I would like to include wind in the models and extend it to 3-D using an advanced version of pyCloudy. Further more, a finer mesh can be utilized

to determine more precise values of the physical parameters. In addition to optical and infrared, X-ray spectra have been observed in many novae (e.g., V2491 Cyg, Ness et al. 2011; V4743 Sgr, Ness et al. 2003 etc.) and similar grid models can also be computed for X-ray spectra. CLOUDY can be used to model all these lines.

For the benefit of all the astronomical community, I have kept the database online at *https://aninditamondal1001.wixsite.com/researchworks* under "Novae Grid Data" on the page *Research/List-of-Documents*. Also a *"Read Me"* file has been kept which describes the structure of the datafiles. Data can be obtained individually in *.xls format (16.4 KB each). The whole grid (256 tables) has a total size of 4.1 MB.

Chapter 5

Study of Quiescence Phase Spectra of Novae

5.1 Introduction

In this chapter, I present the study of the quiescence phase spectra of novae. During the outburst phase, the spectra show strong emission lines of hydrogen and other elements. Higher ionization lines of several elements e.g., helium, oxygen, nitrogen, carbon, iron, nickel, calcium, silicon, argon etc. are seen in the nebular and coronal phase (Bode & Evans 2008). On the other hand, quiescence phase spectra are dominated by the absorption features of the secondary along with the emission lines originating from the cooler, outer part of the disk (Williams 1980), also known as chromospheric emission. The thermal continuum is produced by the hot WD combined with the inner and hotter portion of the disk. The emission lines are generated by photoionization mechanism as the gas in the disk is ionized by the energetic photons emitted from the central continuum source and heated up by the residual kinetic energy of the photoelectrons (Ferland 2003). Thus the spectral characteristics during the quiescence phase reveal the nature of the secondary; the accretion disk; WD; elemental abundances; type of the object etc. Thus, such studies are crucial to understand many aspects of the nova outburst and its evolution.

However, in comparison to outbursting novae, quiescent novae have not been studied in adequate details due to several causes. First, the identification of the quiescent nova is often not unambiguous as novae in the quiescent state are very faint. Sometimes, based on their blue colours and Hα brightness, they can be identified (Anupama & Kamath 2012). Second. as the systems are faint in quiescence phase, magnitude limits of telescopes restrict us to observe them. Third, because of their low brightness, long hours of observation are needed and sometimes signal to noise ratio is low which affects the quality of the spectra. To study and understand the quiescence phase property of novae, I have monitored a handful of classical, recurrent, dwarf and symbiotic novae. In this chapter, I present the results of T CrB, GK Per, RS Oph, V3890 Sgr, V745 Sco and the symbiotic nova BX Mon that show similar behaviour as that of the quiescence phase of novae. I have observed optical spectra and modelled those using photo-ionization code CLOUDY (version c17.00 rc1, Ferland et al. 2017) (discussed in detail in Chapter 2). From the best-fit models, I have estimated the physical parameters e.g., temperature & luminosity of the WD and composition & geometry of the disk, and the type of secondaries.

5.2 Dataset

For the present study, I have taken observations using 2m Himalaya Chandra Telescope (HCT), situated in Hanle, Ladakh, operated by Indian Institute of Astrophysics (IIA). The observing nights are achieved through the submission of observation proposal of "Optical and NIR observations of Classical, Recurrent and Symbiotic Novae". During this time period, I have observed and taken spectra of a handful of old novae, new novae and novae-like variables in optical (3400 - 9200 Å) and near-infrared (1.00 - 2.50 μm) region. Telescope details and the data reducing procedure have been discussed in detail in Chapter 2. Among the observed objects, I present here, results of optical studies of T

Table 5.1: Log of HCT observations.

Date	Julian Date	Object Name	V Magnitude	Exposer Time (s)
April 28, 2015	2457140	T CrB	10	360
May 25, 2015	2457167	RS Oph	12	900
July 23, 2015	2457226	RS Oph	12	900
January 31, 2016	2457418	GK Per	13.5	1800
		RS Oph	12	900
March 17, 2016	2457464	T CrB	10	360
April 28, 2016	2457506	T CrB	10	360
		RS Oph	12	900
May 13, 2016	2457521	BX Mon	12	480
		T CrB	10	360
June 9, 2016	2457548	BX Mon	12	480
September 5, 2016	2457636	T CrB	10	360
		GK Per	13.5	1800
November 1, 2016	2457693	BX Mon	12	480
December 31, 2016	2457753	BX Mon	12	480
		GK Per	13.5	1800
		T CrB	10	360

CrB, GK Per, RS Oph & BX Mon. The log of observations is presented in Table 5.1. I have also used the quiescence phase data of RS Oph which was taken at 2m HCT earlier on April 26, 2007 (around $\sim$ 440 days after the 2006 outburst) (by G. C. Anupama & U. S. Kamath, Mondal et al. 2018).

Table 5.2: Brief description of the objects for quiescence study.

Object	Type	Spectra Taken	$E(B-V)^{ref.}$	Year of Outburst	Reference
T CrB	Recurrent nova	March 17, 2016	0.15 [1]	1866, 1946	Campbell 1948
GK Per	Classical nova*	January 31, 2016	0.30 [2]	1901	Williams 1901
RS Oph	Recurrent nova	April 26, 2007	0.75 [3]	1898, 1907, 1933,	Starrfield et al. 1985;
		January 31, 2016		1945, 1958, 1967,	Kato & Hachisu 2012
				1985, 2006	
BX Mon	Symbiotic nova	May 13, 2016	0.20 [4]	-	Mayall 1940
V3890 Sgr	Recurrent nova	March 21, 1998	-	1962, 1990	Dinerstein 1973;
					Kilmartin & Gilmore 1990
V745 Sco	Recurrent nova	March 20, 1998	-	1937, 1989, 2014	Duerbeck 1989; Waagen 2014

* Classical nova GK Per experienced a nova ouburst on 1901 February 21 and after a long period of irregular fluctuations, it began to act like a dwarf nova (DN) since 1948. These DN outbursts generally last upto 2 months with an amplitude variation $\sim$ 1 - 3 mag (Sabbadin & Bianchini, 1983).

[1] Selvelli et al. 1992; [2] Bianchini & Sabbadin 1985; [3] Viotti et al. 1986; [4] Mondal et al. 2018.

In addition to these objects, I have also modelled published spectra of two other novae, V3890 Sgr and V745 Sco (Anupama & Mikolajewska 1999). These data (CCD spectra) were obtained from the Vainu Bappu Observatory (VBO), IIA, using the 1.02m and 2.3m telescopes. A brief description of these six objects is presented in Table 5.2. All the spectra are normalized with respect to Hβ line for convenience.

5.3 Results

5.3.1 Description of Observed data

The observed spectra are presented in Fig. 5.1 - 5.4. Dates of observations are mentioned in the captions. The observed spectra show prominent emission features generated from the illuminated accretion disk surrounding the WD, which is also the source of the strong blue continuum. Generally, the strong, broad emission lines of hydrogen, helium, oxygen, and iron are seen in the spectra. The emission lines seen in these observed quiescence spectra are broad due to expanded disks. Strong optical Fe II emission lines come from an illuminated (photoionized) high density inner region of the disk. As the disk accumulates more matter, the lines weaken. The spectra also show prominent absorption features in the continuum due to the cool secondaries and they reveal the properties of the secondaries.

The strong emission features observed in the spectrum of T CrB are due to H I (Balmer emissions) lines along with He I 5016, 5876, 6678 Å , He II 4686 Å , Fe II 5016 Å and O I 8444 Å lines. The absence of higher ionization lines can be accounted for by the absorption and softening by reradiation of all direct photons from the accretion disk. Presence of N III 4640 Å and Ca II 3933 Å along with He II 4686 Å indicate the super active phase that took place in October 2015. The strong TiO absorption features at

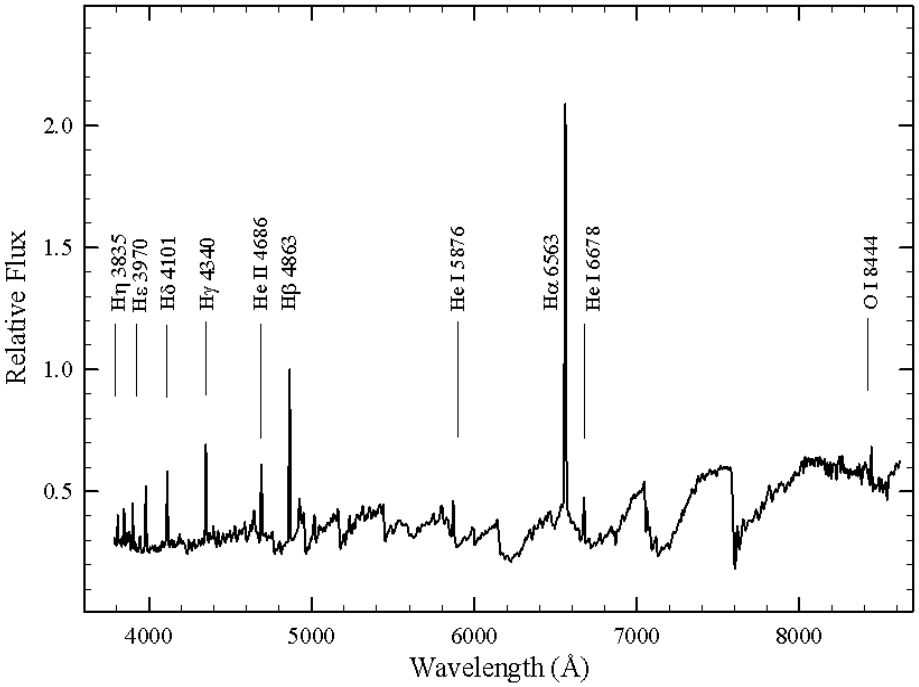

Figure 5.1: Quiscence phase spectrum of nova T CrB, observed on March 17, 2016. The spectrum is normalised w.r.t. $H\beta$ line. Some of the prominent emission lines are marked in the figure. For more details see section 5.3.1.

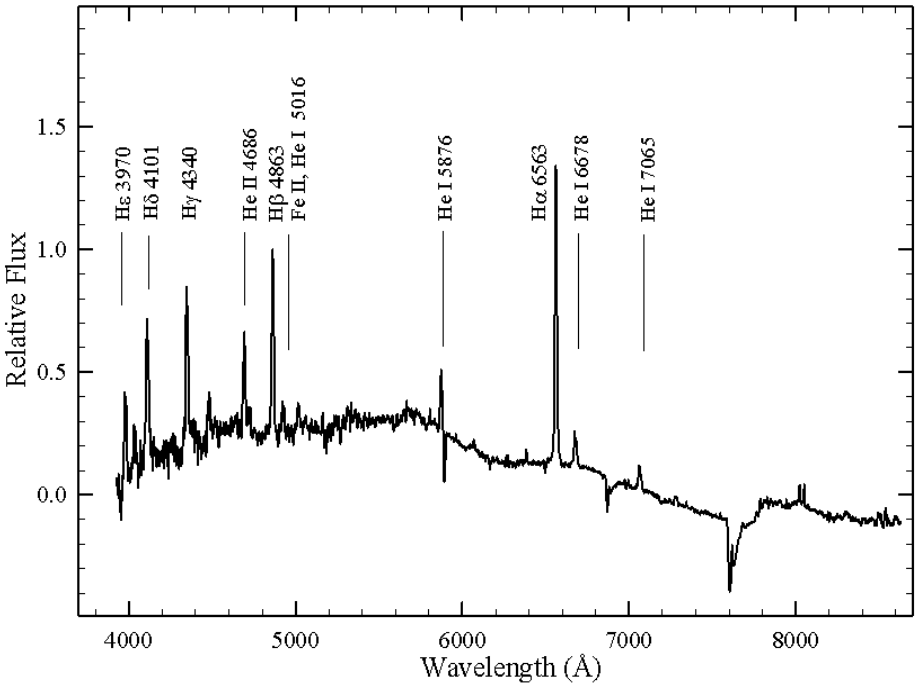

Figure 5.2: Quiscence phase spectrum of nova GK Per, observed on January 31, 2016. The spectrum is normalised w.r.t. $H\beta$ line. Some of the prominent emission lines are marked in the figure. For more details see section 5.3.1.

6180 and 7100 Å are due to the secondary. The observed spectrum of T CrB is presented in Fig. 5.1.

The spectrum of GK Per was observed on January 31, 2016 (Fig. 5.2), about ten months after its recent dwarf nova (DN) outburst on March 2015 (Wilber et al. 2015), which lasted for 2 months. Presence of strong He I 5876, 6678 & 7065 Å , and He II 4686 Å lines and Fe II features along with strong Balmer emission lines indicate towards this active phase and the bluer continuum indicates towards the higher temperature of the accretion disk. TiO absorption features due to the cool component are relatively weak.

For RS Oph, both the quiescence spectra taken on April 26, 2007 and January 31, 2016 were derredened using $E(B-V) = 0.75$ (Mondal et al. 2018) (Fig. 5.3). The spectrum taken on April 26, 2007, shows a red continuum with clear TiO absorption bands at 4762, 5448, 5598, 5629 and 6159 Å. The absorption band strength indicate the secondary spectral type to be M2 - M3. In the spectrum taken on 2007, nebular line strengths have already decreased and the Fe II permitted lines can be observed prominently. The continuum is bluer compared to its nebular spectrum (see Chapter 3 for details), indicating the presence of an accretion disk. Both the quiescense-phase spectra show prominent emission lines of H (Balmer emissions) and He I 4471, 5016, 5876, 6678 & 7065 Å together with strong TiO absorption features at 5448 and 6180 Å contributed by the secondary. With respect to 2007 spectrum, Fe II lines are weaker in 2016 spectrum, which indicate that the accretion disk has been formed. This is in line with the fact that the mass accretion rate is high in the case of RS Oph (Yaron et al. 2005).

The spectrum of BX Mon is shown in Fig. 5.4. The symbiotic nova BX Mon was discovered by Mayall (1940) and its classification is based on the combination spectra in the optical region showing simultaneously very high excitation emission lines and low

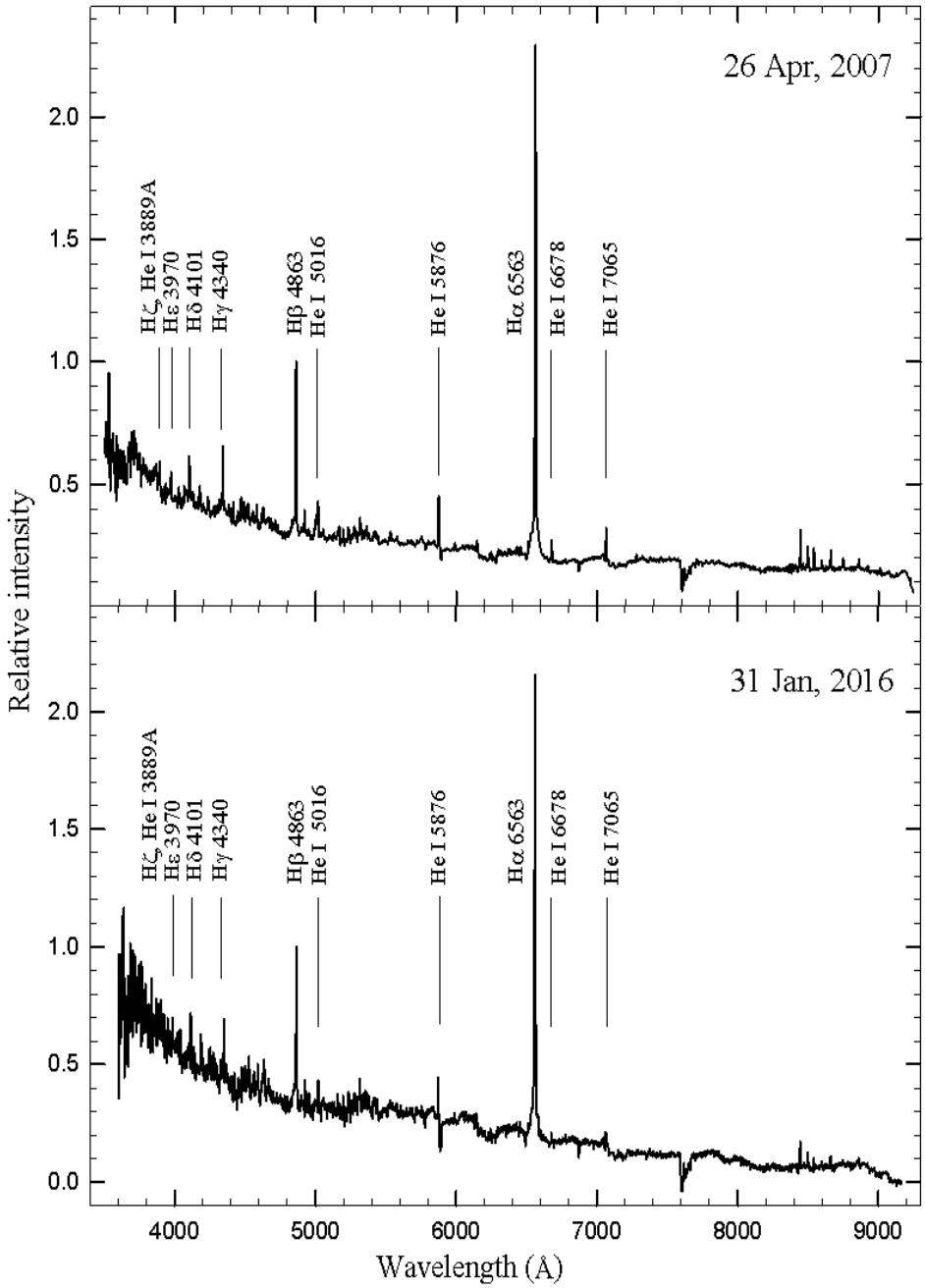

Figure 5.3: Quiscence phase spectra of nova RS Oph, observed on April 26, 2007 and January 31, 2016. The spectrum is normalised w.r.t. $H\beta$ line. Some of the prominent emission lines are marked in the figure. For more details see section 5.3.1.

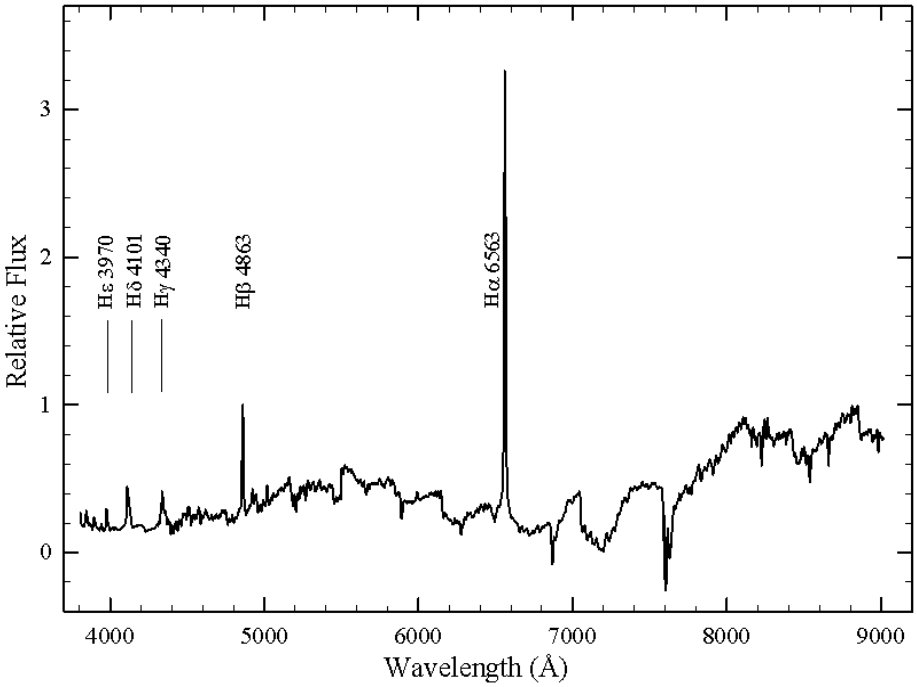

Figure 5.4: Quiscence phase spectrum of symbiotic nova BX Mon observed on May 13, 2016. The spectrum is normalised w.r.t. $H\beta$ line. Some of the prominent emission lines are marked in the figure. For more details see section 5.3.1.

temperature absorption features (Kenyon 1986). No nova-like eruption has ever been recorded for this system. However, the eclipsing binary system shows variability with a periodicity of 1401 days and an amplitude of ~ 3 magnitudes (Dumm et al. 1998). The observed spectrum is dominated by the strong TiO absorption features at 5448 and 7100 Å contributed by the cool component. Balmer emission lines are seen superimposed on the spectrum of the cool red continuum. No other strong emission lines are seen in the observed spectrum. This is possibly due to the low temperature of the disk.

Table 5.3: Observed and best-fit CLOUDY model line fluxes.

Wavelength		T CrB			GK Per			RS Oph					
λ		(Mar 17, 2016)			(Jan 31, 2016)			(Apr 26, 2007)			(Jan 31, 2016)		
(Å)	Line ID	Obs.	Mod.	χ^2	Obs.	Mod.	χ^2	Obs.	Mod.	χ^2	Obs.	Mod.	χ^2
3889	Hζ, He I	0.21	0.15	0.36	...	...	...	...	...	...	0.23	0.18	0.25
3970	Hϵ,	0.34	0.31	0.09	0.41	0.34	0.49	...	...	...	0.20	0.24	0.16
4101	Hδ	0.52	0.45	0.49	0.63	0.52	0.56	0.37	0.39	0.04	0.38	0.32	0.36
4340	Hγ	0.61	0.52	0.81	0.80	0.65	0.25	0.43	0.51	0.64	0.34	0.38	0.13
4471	He I	...	...	...	...	...	...	0.08	0.09	0.01	...	...	...
4686	He II	0.37	0.42	0.25	0.62	0.57	0.25	...	...	...	...	...	...
4863	Hβ	1.00	1.00	0.00	1.00	1.00	0.00	1.00	1.00	0.00	1.00	1.00	0.00
5016	Fe II, He I	0.45	0.53	0.64	...	...	...	0.12	0.22	1.00	0.27	0.22	0.25
5876	He I	0.11	0.19	0.64	0.31	0.30	0.01	0.20	0.29	0.81	0.45	0.39	0.36
6563	Hα	3.06	3.21	2.25	1.92	2.59	2.45	3.30	3.41	1.21	3.60	3.42	3.24
6678	He I	0.13	0.19	0.36	0.09	0.12	0.09	0.07	0.09	0.04	0.13	0.19	0.36
7065	He I	...	...	...	0.07	0.08	0.01	0.08	0.15	0.49	0.18	0.22	0.16
8444	O I	0.09	0.18	0.81	...	...	...	...	...	...	...	...	...
Total		...	...	5.89	...	...	6.65	...	...	4.24	...	...	5.27

Table 5.4: Observed and best-fit CLOUDY model line fluxes.

Wavelength λ (Å)	Line ID	BX Mon (May 13, 2016) Obs.	Mod.	χ^2	V3890 Sgr (Mar 21, 1998) Obs.	Mod.	χ^2	V745 Sco (March 20, 1998) Obs.	Mod.	χ^2
3970	Hϵ,	0.21	0.26	0.25	...	...	...	...	...	...
4101	Hδ	0.39	0.37	0.04	...	...	...	...	...	...
4340	Hγ	0.32	0.41	0.81	0.25	0.29	0.16	...	...	...
4471	He I	...	...	...	...	...	...	...	...	...
4686	He II	...	...	...	...	...	...	...	...	...
4863	Hβ	1.00	1.00	0.00	1.00	1.00	0.00	1.00	1.00	0.00
5016	Fe II, He I	...	...	...	0.38	0.40	0.04	0.17	0.21	0.16
5169	Fe II	...	...	...	0.49	0.45	0.16	0.18	0.19	0.01
5317	Fe II	...	...	...	0.18	0.20	0.04	...	...	...
5876	He I	...	...	...	0.40	0.42	0.04	0.61	0.51	1.00
6563	Hα	3.95	4.10	2.25	8.25	7.34	9.20	6.83	6.75	0.64
6678	He I	...	...	...	0.18	0.21	0.09	0.24	0.31	0.49
7065	He I	...	...	...	0.15	0.17	0.04	0.18	0.21	0.09
Total		...	...	3.35	...	...	9.77	...	...	2.39

5.3.2 Modelling of spectra

For modelling of the spectra, I have considered a three component model consisting of the radiation from the central WD, photoionization emission from the accretion disk formed around the WD and the cool continuum coming from giant secondary. To reduce the number of free parameters as not so many emission lines are present in the quiescence spectra, I kept the R_{in} and R_{out} values fixed for all the objects. Camenzind (2007) gave the value for WD radius of about 10^{8-9} cm. So, I have adapted $R_{in} = 10^9$ cm. For a close binary system consisting of a mass of primary = 1 $M_{\odot}$, mass of secondary = 0.5 $M_{\odot}$ and the orbital period of 3 - 10 hr, outer radius of the accretion disk can reach up to 3×10^{11} cm (Paczynski 1977, He et al. 2013). Following this, I have considered $R_{out} = 10^{11} cm$, which are standard values for the inner and outer radii of an accretion disk with a central WD of $\sim$ 1 $M_{\odot}$. Also, the semi-height of the cylindrical disk has been kept fixed as $10^8 cm$ for the same reason. A constant mass per unit volume throughout the model shell gives the value of α = - 2. From the Hα/Hβ line flux ratio, Hydrogen density of the disk is estimated. The rest of the elements are kept at solar abundance except for those which show strong presence of elemental lines in spectra. By matching the elemental emission lines of observed and modelled spectra, elemental abundances are determined. The spectra for giants are taken from the archival data of 1.5m SMARTS (Small & Moderate Aperture Research Telescope System) telescope (*http://www.ctio.noao.edu/noao/node/148*) (Riedel et al. 2007).

These three components (black-body radiation of the WD, model generated emission line spectra and absorption spectra of giants) are then added up in various ratios to get the final best-fit model spectra using the χ^2 minimization technique. Both the observed and model generated spectra are normalized with respect to Hβ line. Observed (black solid) and modelled spectra (red dashed) are shown in Fig. 5.1-5.4. The relative fluxes of the best-fit model predicted lines, observed lines and corresponding χ^2 values are

presented in Table 5.4; and the best-fit model parameters are presented in Table 5.5. From the best-fit model spectra, contribution of the components are also determined. In the following subsections, details of the parameters for individual nova are discussed.

T Coronae Borealis (T CrB): For T CrB, I have considered a hot WD ($T = 10^{4.1}$ K) surrounded by a cylindrical accretion disk of thick H-rich material ($n_H = 10^{11}$ cm^{-3}). Presence of higher ionization lines (e.g., N III, He II, Ca II) indicate the presence of some hot centres in the accretion disk. Thus, for the modelling, I considered two shells with different temperatures ($T = 10^5$ K for higher ionization lines and $T = 10^{4.1}$ K for lower ionization lines) and added them to match the emission features. The absorption features seen in the observed spectrum is due to the secondary. Previously, Kleinmann & Hall (1986) suggested a spectral type of M2 - M5 III and Mürset & Schmid (1999) suggested a spectral type of M4.5 III for the secondary of T CrB. Anupama & Mikolajewska (1999) determined a spectral type of M3 - 4 III. I added the spectrum of M4 type giant with the modelled spectrum and found that it fits well with the absorption features. As the properties of M4 type giant ($T \sim 3500$ K, $L \sim 7\ L_\odot$) does not contribute any emission lines in the spectra, all the emission features for the T CrB spectrum are generated from the accretion disk. So only the model spectrum generated from the disk added with the black-body radiation from the WD was sufficient to produce the emission lines. By fitting the emission lines of different elements with varying abundances, I estimate the elemental abundances using χ^2 values. Elemental abundances of He, Fe and O are estimated using the prominent emission features. The strong Fe II 5016 Å line is blended with He I. But as He abundance is estimated from other strong He I lines, I consider the blended Fe II line to estimate the Fe II abundance.

GK Persei (GK Per): To model the complex spectrum of GK Per, higher effective

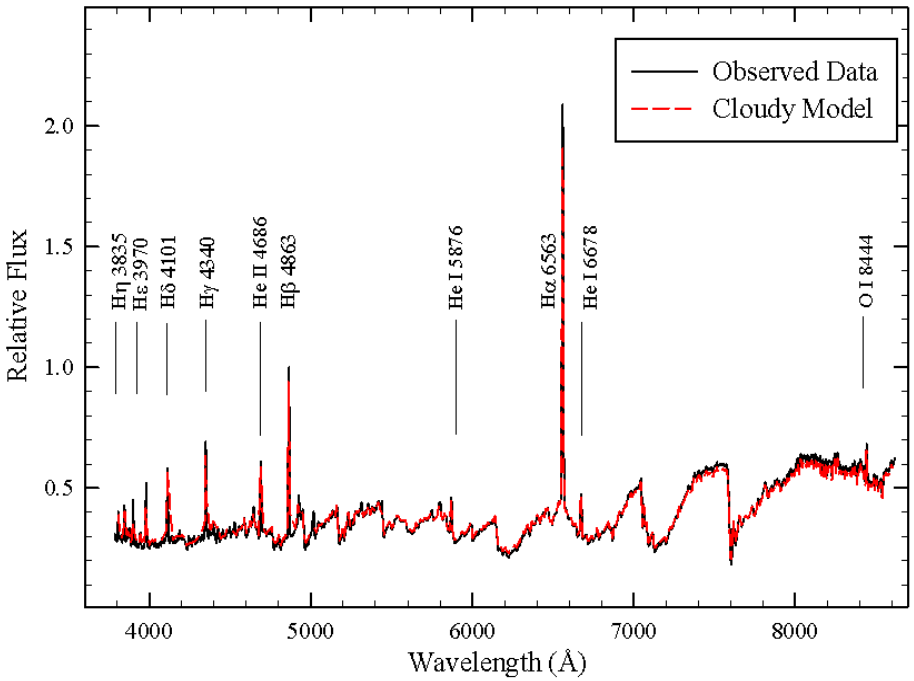

Figure 5.5: Best-fit CLOUDY modelled spectrum (red dashed line) matched with the quiscence phase spectrum of T CrB (black line), observed on March 17, 2016. All the spectra are normalized w.r.t Hβ line. Some of the prominent emission lines are marked in the figure. For more details see section 5.3.2.

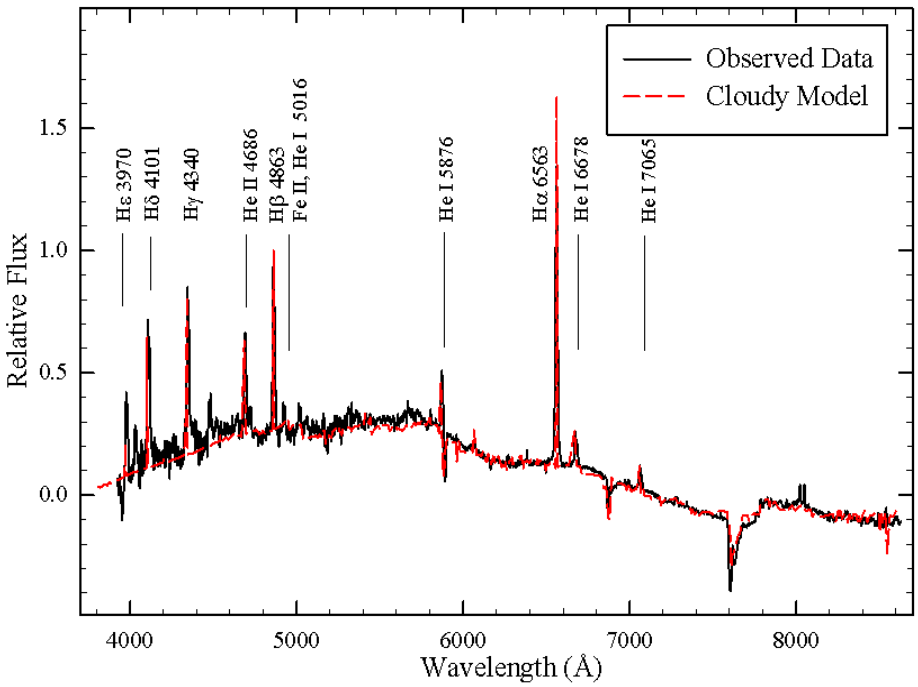

Figure 5.6: Best-fit CLOUDY modelled spectrum (red dashed line) matched with the quiscence phase spectrum of GK Per (black line), observed on January 31, 2016. All the spectra are normalized w.r.t Hβ line. Some of the prominent emission lines are marked in the figure. For more details see section 5.3.2.

temperature for the source has to be considered which is surrounded by a cylindrical accretion disk of H-rich matter. The best-fit model reveals $T = 10^{4.5}$ K, $L = 10^{35.2}$ erg/s and $n_H = 10^{11.1}$ cm^{-3}. The high temperature and luminosity indicate towards the active phase of the dwarf outburst in March 2015. From the He I and He II lines, abundance of helium is estimated as 0.7 with respect to solar abundances, which is subsolar. Abundances of other elements could not be estimated due to the absence of prominent lines. Absence of Fe II features can be accounted for a thick disk as the Fe II lines are softened by the optically thick, cooler outer region of the disk. Earlier, Gallagher & Oinas (1974) determined the type of secondary as K2 V - IV and Morales-Reuda et al. (2002) found the donor star type as K1 IV. In this case, I observed that the spectrum of K5 V giant fits well with the absorption features seen in the observed spectrum. So, a spectrum of K5 V giant was added with the CLOUDY modelled spectrum to get the final spectrum.

RS Ophiuchi (RS Oph): RS Oph system is composed of a massive WD ($\sim 1.35\ M_{\odot}$, Kato et al. 2008) primary accompanied by a red giant secondary. To generate the model spectra for both dates, three components were considered: a WD as an ionising source, a cylindrical accretion disk surrounding the source and the secondary red giant. The final spectrum was obtained by adding the fluxes generated by these three components. From the best-fit model, I obtain that the hot and luminous WD ($T = 10^{4.2}$ K and $L = 10^{33.0}$ erg/s) is surrounded by a cylindrical accretion disk of H-rich material ($n_H = 10^{11.0}$ cm^{-3}). A spectral type of M2 III fits the TiO absorption features of the secondary well. Worters et al. (2007) and Anupama & Mikolajewska (1999) also estimated a M2 III type secondary for RS Oph. These two spectra are added with the black-body radiation continuum from the WD ($T = 10^{4.2}$ K) to get the final model generated spectrum. Helium abundance is estimated as 0.8 with respect to solar abundances, which is also subsolar. Only one prominent Fe II line is present but that too is blended, so, abundance of Fe cannot be estimated accurately. Since there were no prominent lines of other elements, the abundances of other elements could not be estimated.

BX Monocerotis (BX Mon): Symbiotic nova BX Mon shows similar observational behaviour as the quiescence phase nova. For the modelling of the spectrum of BX Mon, I have considered a similar approach of three component model consisting of WD, accretion disk and the giant and added the spectra to match with the observed one. From the best-fit model, I got the hot WD ($T = 10^{4.1}$ K, $L = 10^{32}$ erg/s) is surrounded by thick H-rich ($n_H = 10^{11.4}$ cm^{-3}) cylindrical accretion disk. Elemental abundance cannot be estimated as the prominent emission lines of other elements except Balmer lines are absent. Previously Mürset & Schmid (1999) determined a spectral type of the secondary as M4-5.5 III. I added a spectrum of M4.5 III type with the modelled spectrum and found that it fits the absorption features seen in the observed spectrum properly. Thus, it confirms that the secondary type for BX Mon is M4.5 III.

V3890 Sagittarii (V3890 Sgr): I used the published optical spectroscopic data of V3890 Sgr observed at VBO on March 21, 1998 (Anupama & Mikelojewska, 1999). The spectrum shows prominent Balmer emission lines along with strong Fe II lines, indicating the accretion disk is not fully formed. Absence of higher ionization lines marks the quiescence phase of the system. The absorption features are due to the giant secondary. From the best-fit CLOUDY model, I concluded that the system consists of an ionizing source of low temperature ($T = 10^{4.01}$ K) and luminosity ($10^{28.2}$ ergs s^{-1}) surrounded by a cylindrical accretion disk of H-rich material ($n_H = 10^{11.1}$ cm^{-3}). Using the prominent He I (5016, 5876, 6678 & 7065 Å) and Fe II (5016, 5159 & 5317 Å) lines, elemental abundances of helium and iron are estimated as 1.5 and 10 respectively with respect to solar abundances. Also, a spectral type M5 III added to the model generated spectrum to match the absorption features and I found that the spectrum fits properly. Anupama & Mikelojewska (1999) determined the type of the secondary as M5 III. Harrison et al. (1993) also indicated a spectral type M5 III based on the infrared

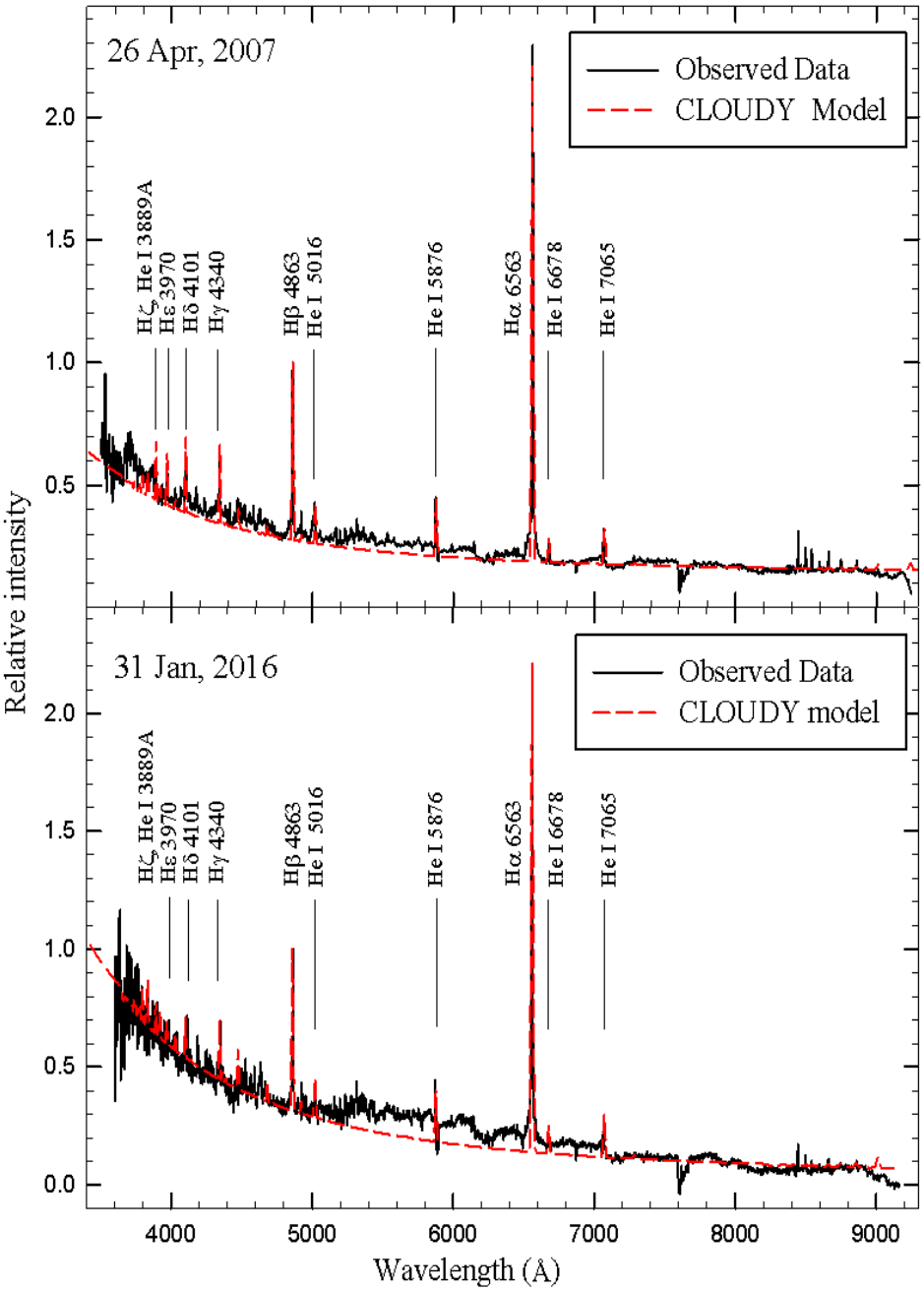

Figure 5.7: Best-fit CLOUDY modelled spectra (red dashed line) matched with the quiscence phase spectra of RS Oph (black line), observed on April 26, 2007 and January 31, 2016. All the spectra are normalized w.r.t Hβ line. Some of the prominent emission lines are marked in the figure. For more details see section 5.3.2.

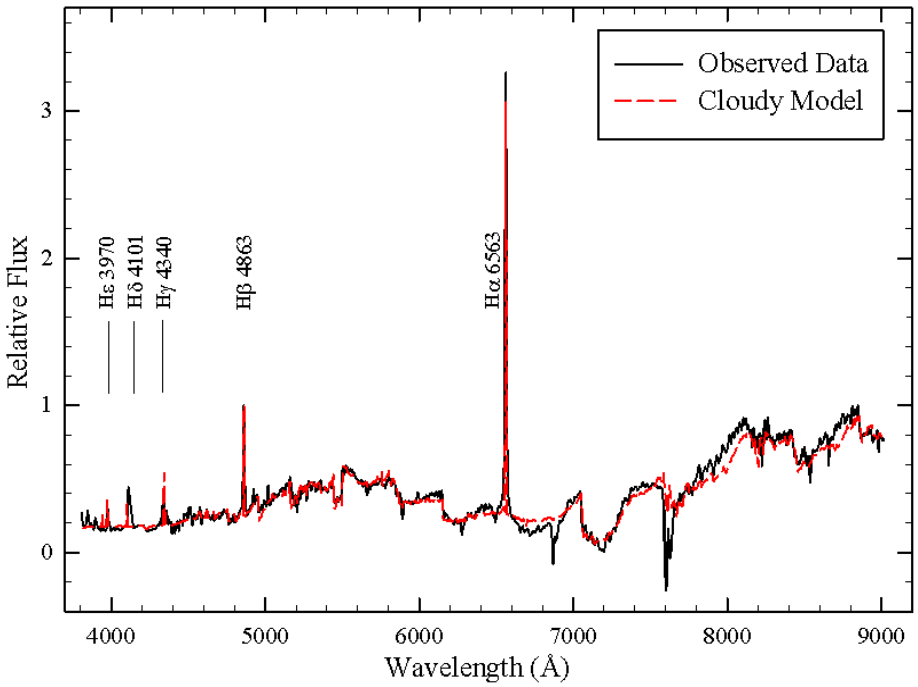

Figure 5.8: Best-fit CLOUDY modelled spectrum (red dashed line) matched with the quiscence phase spectrum of BX Mon (black line), observed on May 13, 2016. All the spectra are normalized w.r.t Hβ line. Some of the prominent emission lines are marked in the figure. For more details see section 5.3.2.

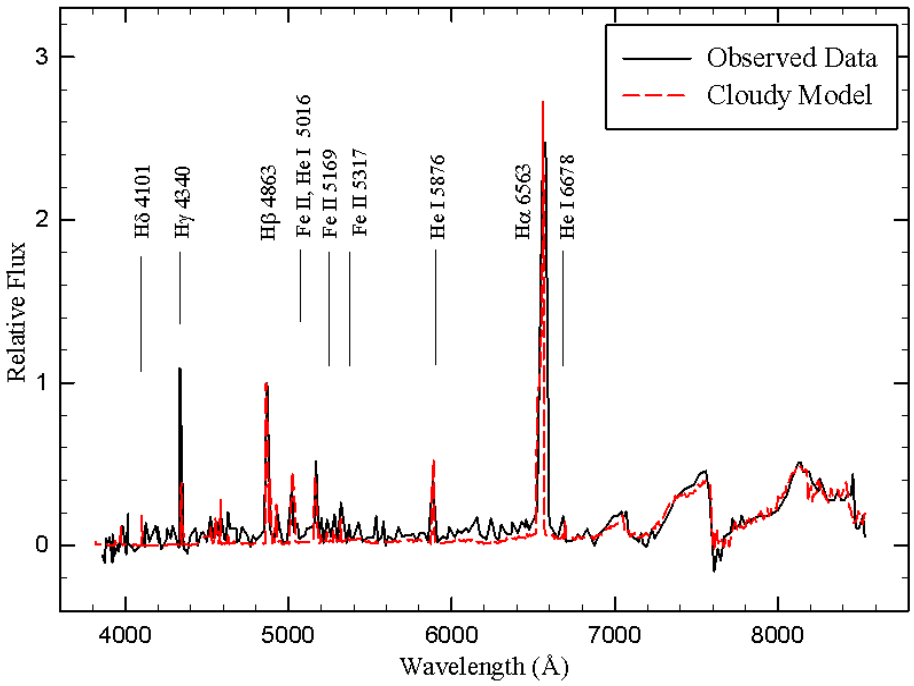

Figure 5.9: Best-fit CLOUDY modelled spectrum (red dashed line) matched with the quiscence phase spectrum of V3890 Sgr (black line), observed on March 21, 1988. All the spectra are normalized w.r.t Hβ line. Some of the prominent emission lines are marked in the figure. For more details see section 5.3.2.

photometric data during 1990 outburst. The result matches with the previous results. In general, I use IRAF software to measure the flux of emission lines, but in case of the observed spectrum of V3890 Sgr, Hα line is truncated. So, I have used line fluxes measured by Anupama & Mikelojewska (1999). Probably due to the difference in method for the measurement and presence of fewer emission lines, I obtained a higher χ^2_{red} value.

V745 Scorpii (V745 Sco): To study the quiescence phase spectrum of V745 Sco, I have modelled the published optical spectroscopic data taken on March 20, 1998 (Anupama & Mikelojewska, 1999) using CLOUDY photoionization code. The spectrum shows prominent Balmer emission lines although the blue region is not well resolved.

Prominent Fe II and He I lines can also be easily identified. The strong TiO absorption features are due to the secondary companion. The best-fit model results a hot central source with relatively lower temperature ($T = 10^{4.0}$ K) and luminosity ($L = 10^{28.0}$ ergs s^{-1}), is surrounded by thick H-rich ($n_H = 10^{11.0}$ cm^{-3}) cylindrical accretion disk. From the prominent He I 5016, 5876, 6678 & 7065 Å lines and Fe II 5016 & 5169 Å lines, elemental abundances of helium and iron are estimated as 1.1 and 10 respectively with respect to solar abundances. Williams et al. (1991) suggested the red giant companion of V745 Sco as M6 - 8 III type, Duerbeck (1989) classified it as M6 III and Harrison et al. (1993), based on the infrared spectra inferred a spectral type of M4 III. Based on the TiO and VO indices of the optical spectra, Anupama & Mikelojewska (1999) suggested a spectral type of M4 - 5 III, while the Na I index indicated towards a M6 III type. From the study, I have observed that the spectrum of a 5.5M III type giant fits the absorption features properly. So, a spectrum of 5.5M III type giant is added to get the final spectrum.

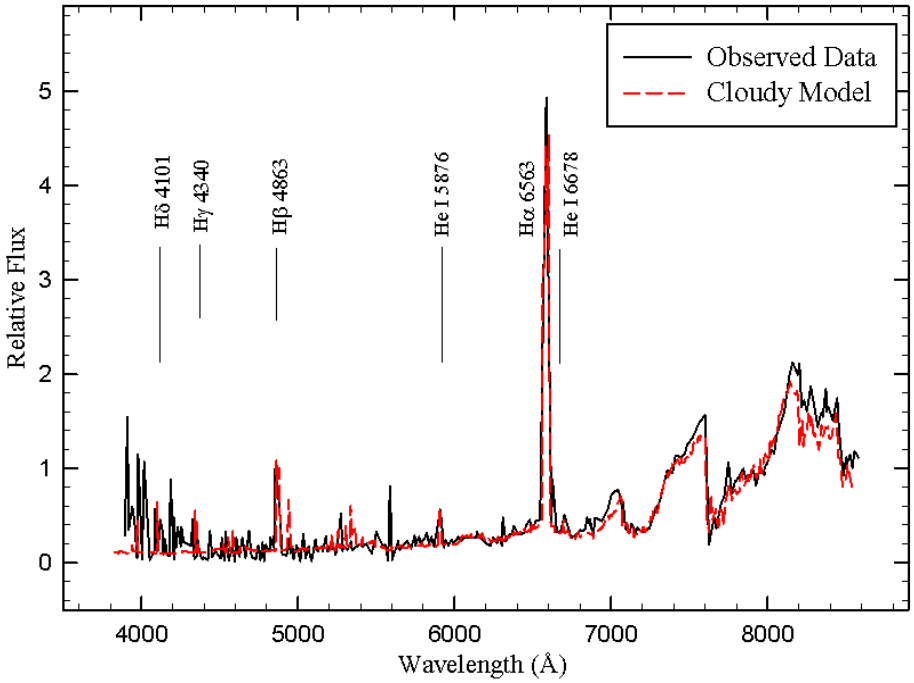

Figure 5.10: Best-fit CLOUDY modelled spectrum (red dashed line) matched with the quiscence phase spectrum of V745 Sco (black line), observed on March 20, 1988. All the spectra are normalized w.r.t Hβ line. Some of the prominent emission lines are marked in the figure. For more details see section 5.3.2.

Table 5.5: Best-fit CLOUDY model parameters.

Parameters	T CrB	GK Per	RS Oph		BX Mon	V3890 Sgr	V745 Sco
	Mar 17	Jan 31	Apr 26	Jan 31	May 13	Mar 21	Mar 20
	2016	2016	2007	2016	2016	1998	1998
Log(T_{BB}) (K)	4.1/5.0	4.5	4.2	4.2	4.1	4.01	4.0
Log(L) (erg s^{-1})	34.0	35.2	33.0	33.0	32.0	28.2	28.0
Log(n_H) (cm^{-3})	11.2	11.1	11.0	11.0	11.4	11.1	11.0
α[a]	-2	-2	-2	-2	-2	-2	-2
Log(R_{in}) (cm)	9	9	9	9	9	9	9
Log(R_{out}) (cm)	11	11	11	11	11	11	11
Log($semi-height$) (cm)	8	8	8	8	8	8	8
Filling factor	0.1	0.1	0.1	0.1	0.1	0.1	0.1
β[b]	0.0	0.0	0.0	0.0	0.0	0.0	0.0
He/He$_\odot$[c]	0.3(6)	0.7(4)	0.8(4)	0.8(5)	–	1.5(4)	1.1(4)
Fe/Fe$_\odot$[c]	8.0(1)	–	8.0(1)	5.0 (1)	–	10.0(3)	10.0(2)
O/O$_\odot$[c]	3.0(1)	–	–	–	–	–	–
Number of observed lines (n)	11	9	10	9	5	9	7
Number of free parameters (n_p)	6	4	5	5	3	5	5
Degrees of freedom (ν)	5	5	5	4	8	4	2
Total χ^2	5.89	6.65	5.27	4.24	3.35	9.77	2.39
χ^2_{red}	1.18	1.33	1.05	1.06	1.67	2.44	1.20
Type of secondary	M4 III	K5 V	M2 III	M2 III	M4.5 III	M5 III	M5.5 III
Contribution of secondary	40%	30%	65%	35%	55%	75%	70%

[a] Radial dependence of the density r^α

[b] Radial dependence of filling factor r^β

[c] Abundances are given in logarithmic scale, relative to solar abundance. All other elements which are not listed in the table were set to their solar values. The number in the parentheses represents number of lines used in determining each abundance.

5.4 Summary & Discussions

I have studied spectroscopic behaviour of five novae (T CrB, GK Per, RS Oph, V3890 Sgr, V745 Sco) and one symbiotic nova (BX Mon). I have used observed and published data, and modelled these quiescence phase spectra using photoionization code CLOUDY. The models were generated for $R_{in} = 10^9$ cm, $R_{out} = 10^{11}$ cm and $semi - height = 10^8$ cm. I have generated spectra emitted from the accretion disk; and added the model generated spectrum with black-body continuum corresponding to the WD temperature and secondary spectrum to get the final spectra. Generally single shell model has been sufficient but in case of T CrB, I had to consider two different shells corresponding to higher and lower temperatures to match the higher (N III, Ca II) and lower (He I, Fe II, O I) ionization lines. From the best-fit models, the physical parameters, e.g., temperature of the WD; temperature, luminosity, H-density of the disk etc. related to the system have been estimated. In general the WD temperature and luminosity are in the range of $T = 10^{4.0-4.5}$ K and $L = 10^{28.0-35.2}$ erg/s; density of the disk is $n_H = 10^{11.0-114}$ cm^{-3}. For GK Per, the temperature is high ($T = 10^{4.5}$ K) and presence of strong He II line indicates that the system is still in its active phase. Weak presence of Fe II lines in the observed spectra indicates that for GK Per & RS Oph the disk is thick, whereas, strong Fe II lines in the spectra of V3890 Sgr & V745 Sco indicate that the disk is not fully formed. Lower luminosity values for V3890 Sgr & V745 Sco may be interpreted on this ground. I also have estimated abundances for few elements e.g., He, Fe, & O for the objects where emission lines of those elements were prominent. A higher He and Fe abundance for these novae indicates towards a metal rich atmosphere. By fitting the spectra of various secondaries and matching the strength of TiO absorption bands, I estimated the type of secondaries and percentage of their contributions for these objects. For T CrB, RS Oph, BX Mon, V3890 Sgr & V745 Sco the secondaries are in the range of M2 III - M5.5 III types and for GK Per the secondary is K5 V type. For all the novae, except V3890 Sgr, reduced χ^2 values lie in between 1 & 2 which indicates that

the model generated spectra matched the observed spectra satisfactorily. For V3890 Sgr, the reduced χ^2 value is relatively higher, 2.44. This is probably due to the difference in method for the measurement of Hα line, which is the highest contributor to the χ^2 value.

I am presently working on the remaining observed data and trying to understand their properties through modelling of spectra which will be published in a future work.

Chapter 6

Summary and Scope for Future Work

In this chapter, I summarize the work contained in this thesis with a discussion on the results obtained and the possibilities for future work related to the studies is also discussed.

In this dissertation, the primary goal was to understand the nature of novae spectra through study of multi-wavelength spectroscopic data. I have modelled the spectra using photoionization code to study the physical properties and other characteristics of the system. The summary of the works is as follows.

Study of the Recurrent Nova RS Ophiuchi

The observation and modelling of multi-wavelength spectroscopic data of recurrent nova RS Ophiuchi during its 2006 outburst is discussed. The optical data were taken at 2m HCT, IIA, as well as published data are also used. The evolution of the optical spectra of RS Oph is studied since the outburst till the end of coronal phase in details. Temporal evolution of the line profiles for important elements are studied thoroughly and it reveals how the physical characteristics of the system changes as it journeys through its various phases. Photoionization models are generated to match the observed spectra to get a deep insight of the nature of the system. From the best-fit models, the properties of the central hot source as well as the geometry and structure of the ejecta are

resolved. The results show that a hot ($T_{BB} \sim 10^5$ K), luminous ($L \sim 10^{36}$ erg s^{-1}), hight mass ($M_{WD} \sim 1.35\ M_\odot$) WD is surrounded by a spherical ejecta of thick H-rich ($n_H \sim 10^{10}$ cm^{-3}) material. An overall abundance values of the ejecta are calculated from the mean of these modelled results. The derived values show that helium, nitrogen, neon, iron and argon abundances are all enhanced relative to solar, while the oxygen and aluminium abundances are solar with respect to hydrogen, and silicon abundances are subsolar with respect to hydrogen. An estimation of ejecta mass is also calculated as $3.4 - 4.9 \times 10^{-6}\ M_\odot$.

Results show that small recurrence period of RS Oph is due to a high mass central WD. Using the similar modelling techniques, physical characteristics of such RNe and other CVs can also be resolved. We can also apply similar methods to study various slow and fast novae during their outbursts and recieve a detail understanding on how the systems evolve differently. Work is in progress to study several similar objects during their outburst phases using the observed as well as published and archival data to get a better insight into the novae phenomenon.

Photoionization model grid of novae: estimation of physical parameters

I have computed grid models of novae and the aim was to generate an extended five dimensional parameter space for dust-free novae by varying hydrogen density, inner radius and thickness of the novae ejecta, temperature, and luminosity of the ionizing source in commensurate with an observed range. From the model generated synthetic spectra I have calculated line intensities of 56 hydrogen and helium lines which are generally observed prominently in novae spectra, spanning over a wide range of wave-lengths: from ultraviolet to infrared. Simulated hydrogen and helium line intensities from the model grid can be compared with observations and physical parameters like T_{BB}, L, and n_H can be inferred. To test the robustness of the calculations, I have cross-checked predictions from the grid results for few novae, e.g., RS Oph, V1065 Cen, V1974 Cyg, V1186

Sco and PW Vul with published data and they matched well. I also have estimated density and luminosity of five other galactic novae (KT Eri, V5558 Sgr, U Sco, V3339 Del), as well as an extragalactic nova (Nova IC1613 2015).

I have considered here dust-free environment because from observations, it has been found that most of the novae do not form dust. I plan to incorporate dust in this model and check the effect of dust on the line intensities. Also, in the present calculation, I used solar abundance to limit the computational time. If abundances of other elements are increased or decreased, hydrogen line intensities may get changed. To check this, I have constructed a few models with higher metallicity (2, 2.5 and 3 times solar metallicity) and found that variation in hydrogen line intensities are less than 15%. I am in a process to extend the database by constructing grid models incorporating dust and higher metallicity which will be presented in a future work. Further more, a finer mesh can be utilized to determine more precise values of the physical parameters. Also, I would like to include wind in these models and extend it to 3-D using an advanced version of pyCloudy in future.

Study of Quiescence Phase Spectra of Novae

Observation and modelling of quiescence phase spectra of various novae have been described in details. The observational data are taken at 2m HCT, IIA, and then reduced and modelled. Optical spectrum is dominated by giant secondary, with emission lines due to H I and He I superposed, Fe II and O I lines are also present. Higher ionization lines, e.g., He II lines are extremely weak or absent. Presence of those indicates that the system is still in the active phase. The continuum are bluer compared to the outburst spectrum, indicating the presence of an accretion disk. I have modelled the spectra using photoionization code CLOUDY and from the best-fit models, I have estimated the physical parameters, e.g., temperature of the WD; temperature, luminosity, H-density of the disk, associated with the system. I have also estimated elemental abundances

for some systems where prominent emission lines of other elements were present. Using archival data of various giants and comparing them with the absorption features of the continuum and from the best-fit, I have determined the type of secondaries (K - M type giants) and also their percentage of contribution to the spectra.

In this work, due to time constrain, I have used data of only four of the forteen observed novae. In future, I will complete the analysis of the remaining optical & NIR spectroscopic data of other observed novae and do a detail comparative study of novae in quiescence phase. Also I plan to model the NIR region of the observed data of these novae and publish the results.

The main aim of this work was to get further insight into the topic and the study was done in hope that it will add significant value to our understanding of the nova phenomenon. Progress in this direction has already commenced and I hope to complete the remaining works as discussed above in the near future.

Bibliography

[1] Adams W. S. & Joy A. H., 1933, PASP, 45, 301.

[2] Anupama G. C. & Prabhu T. P., 1989, JApA 10, 237.

[3] Anupama G. C. & Mikolajewska J., 1999, A&A, 344, 177.

[4] Anupama G. C. & Kamath U. S., 2012, BASI, 40, 161.

[5] Anupama G. C., Kamath U. S., Ramaprakash A. N. et al., 2013, A&A, 559, A121.

[6] Ashok N. M. & Banerjee D. P. K., 2003, A&A, 409, 1007.

[7] Banerjee D. P. K., Das R. K., & Ashok N. M., 2009, MNRAS, 399, 357.

[8] Banerjee D. P. K., Das R. K., Ashok N. M. et al., 2010, MNRAS, 408, L71.

[9] Bath G. T. & Shaviv G., 1976, MNRAS, 175, 305.

[10] Bianchini A. & Sabbadin F., 1985, in *Multifrequency Behaviour of Galactic Accreting Sources*, ed. F. Giovannelli (Rome: Italian astronomical Society), p. 73.

[11] Bode M. F. & Kahn F. D., 1985, MNRAS, 217, 205.

[12] Bode M. F., O' Brien T. J., Osborne J. P. et al., 2006, ApJ, 652, 629.

[13] Bode M. F., Harman D. J., O' Brien T. J. et al., 2007, ApJ, 665, L63.

[14] Bode M. F. & Evans A., 2nd eds., 2008, Classical Novae, Cambridge University Press.

[15] Boyarchuk A. A. & Antipova L. I., 1990, Lect. Notes Phys., 369, 97.

[16] Brandi E., Quiroga C., Mikolajewska J. et al., 2009, A&A, 497, 815.

[17] Buil C., 2006, Cent. Bur. Electron. Tel.(CBET), p.403.

[18] Bulletin of Astronomical Society of India (BASI), Special issue on Classical Novae, 2012, Cambridge University Press.

[19] Burlak M. A., Esipov V. F., Komissarova G. V., Shenavrin V. I., Taranova O. G., Tatarnikov A. M., & Tatarnikova A. A., 2015, Baltic Astronomy, 24, 109.

[20] Camenzind M., 2007, Compact Objects in Astrophysics: White Dwarfs, Neutron Stars, and Black Holes (Springer Press)

[21] Campbell L., 1948, Harvard Ann., 116, 191.

[22] Chesneau O., Nardetto N., Millour F. et al., 2007, A&A, 464, 119.

[23] Clayton D. D. & Hoyle F., 1974, ApJ, 187, L101.

[24] Cohen J. G., 1985, ApJ, 292, 90.

[25] Das R. K., Banerjee D. P. K., & Ashok N. M., 2006, ApJ, 653, L141.

[26] Das R. K. & Mondal A., 2015, New Ast., 39, 19.

[27] Das R. K., Banerjee D. P. K., Nandi A., Ashok N. M., & Mondal S., 2015, MNRAS, 447, 806.

[28] de Vaucouleurs G., 1978, ApJ, 223, 351.

[29] Della Valle M., 1991, A&A, 252, L19.

[30] Della Valle M. & Livio M., 1995, ApJ, 452, 704.

[31] Diaz M., 2001, ASP Conf. Ser. 247 (San Francisco: ASP) Spectroscopic Challenges of Photoionized Plasmas, 227.

[32] Dinerstein H., 1973, IBVS, 845.

[33] Downes R. A. & Duerbeck H. W., 2000, AJ, 120, 2007.

[34] Duerbeck H. W., 1989, Msngr, 58, 34.

[35] Dumm T., Mürset U., Nussbaumer H., et al., 1998, A&A, 336, 637.

[36] Evans A., Kerr T., Bin Yang et al., 2007a, MNRAS, 374, L1.

[37] Evans A., Woodward C. E., Helton L. A., et al., 2007b, ApJ, 663, L29.

[38] Eyres S. P. S., O' Brien T. J., Beswick R., et al., 2009, MNRAS, 395, 1533.

[39] Ferland G. J., 2003, ARA&A, 41, 517.

[40] Ferland G. J., Porter R. L., van Hoof P. A. M., et al., 2013, RMxAA, 49, 137.

[41] Ferland G. J., Chatzikos M., Guzman F., et al., 2017, RMxAA, 53, 385.

[42] Fujii M., 2006, VSNET Alert 8869.

[43] Gallagher J. S. & Oinas V., 1974, PASP, 86, 952.

[44] Gehrz R. D., 1988, ARA&A, 26, 377.

[45] Gehrz R. D., Truran J. W., & Williams R. E., 1993, in Protostars and Planets III, eds. E. H. Levy & J. I. Lunine, Tuscon Univ. Arizona Press, p. 75.

[46] Gehrz R.D., Truran J. W., Williams R. E., & Starrfield S., 1998, PASP, 110, 3.

[47] Gehrz R. D., 2002, in Classical Nova Explosions, eds. Hernanz M. & José J., NewYork: American Institute of Physics, p. 198.

[48] Gherase R. M., Sonka A. B., Popescu M., Naiman M., & Micu F., 2015, Romanian Astron. J., Vol. 25, No. 3, p. 241248.

[49] Hachisu I. & Kato M., 2001, ApJ 558, 323.

[50] Hachisu I. & Kato M., 2006, ApJS, 167, 59.

[51] Harrison T. E., Johnson J. J., & Spyromilio J., 1993, AJ, 105, 320.

[52] Hauschildt P. H. & Baron E., 1995, J. Quant. Spectrosc. Radiat. Transfer, 54, 987.

[53] Hauschildt P. H., Baron E., Starrfield S. & Allard F., 1996, ApJ, 462, 386.

[54] Hauschildt P. H., Shore S. N., Schwarz G. J., Baron E., Starrfield S. & Allard F., 1997, ApJ, 490, 803.

[55] Hauschildt P. H. & Baron E., 2014, A&A, 566, A89.

[56] He L., Lü G. L. & Zhao Y. H., 2013, RAA, 13, 1213.

[57] Helton L. A., Woodward C. E., Walter F. M., et al., 2010, AJ, 140, 1347.

[58] Hirosawa K., 2006, IAU Circ. 8671.

[59] Hjellming R. J., van Gorkum J.H., Taylor A.R., et al., 1986, ApJ, 305, L71.

[60] Hjellming R. M. & Wade C. M., 1970, ApJ, 162, L1.

[61] Hubble E. P., 1929, ApJ, 69, 103.

[62] Iijima T., 2006a, IAU Circ., 8675, 1.

[63] Iijima T., 2006b, A&A, 451, 563.

[64] Iijima T., 2007a, CBET, 934.

[65] Iijima T., Correia A. P., Hornoch K., & Carvajal J., 2007b, CBET, 1006.

[66] Iijima T., 2009, A&A, 505, 287.

[67] Josafatson K. & Snow T. P., 1987, ApJ, 319, 436.

[68] José J. & Hernanz M., 1998, ApJ, 494, 680.

[69] Joy A. H. & Swings P., 1945, ApJ, 102, 353J.

[70] Kamath U. S., Anupama G. C., Ashok N. M., Mayya Y. D., & Sahu D. K., 2005, MNRAS, 361, 1165.

[71] Kantharia N. G., Anupama G. C., Prabhu T. P., Ramya S., Bode M. F., Eyres S. P. S., O' Brien T. J., 2007, ApJ, 667, L171.

[72] Kato M., Hachisu I., & Luna G. J. M., 2008, in RS Ophiuchi (2006) and the Recurrent Nova Phenomenon, Astronomical Society of the Pacific Conference Series, eds. Evans A., Bode M. F., O' Brien T. J. & Darnley M. J., vol. 401, 308.

[73] Kato M. & Hachisu I., 2012, BASI, 40, 393.

[74] Kenyon S. J., 1986, The Symbiotic Stars, Cambridge Univ. Press, Cambridge.

[75] Kilmartin P. & Gilmore A., 1990, IAU Circ. 5002.

[76] Kleinmann S. G. & Hall D. N. B., 1986, ApJS, 62, 501.

[77] Kraft R. P., 1964, ApJ., 139, 457.

[78] Krautter J., 2008, in Classical Novae, Second Edition, eds. Bode M. F. & Evans A., Cambridge University Press.

[79] Leising M. D. & Clayton D. D., 1987, ApJ, 323, 159.

[80] Liller W., 1989, IAU Circ. 4820.

[81] Livio M., 1992, ApJ, 393, 516.

[82] Livio M. & Truran J. W., 1992, ApJ, 389, 695.

[83] Mayall M.W., 1940, Bull. Harvard College Obs., 913, 8.

[84] McLaughlin D. B., 1939, Pop. Astr., 47, 410, 481, 538.

[85] McLaughlin D. B., 1945, PASP, 57, 69.

[86] McLaughlin D. B., 1960, in Stellar Atmospheres, ed. J. L. Greenstein, University of Chicago Press.

[87] Mondal A., Anupama G. C., Kamath U. S., Das R. K., Selvakumar G., & Mondal S., 2018, MNRAS, 474, 4211.

[88] Mondal A., Das R. K., Shaw G., & Mondal S., 2019, MNRAS, 483, 4884.

[89] Monnier J. D., Barry R. K., Traubet W. A. et al., 2006, ApJ, 647, L127.

[90] Morales-Rueda L., Still M. D., Roche P., Wood J. H., & Lockley J. J., 2002, MNRAS, 329, 597.

[91] Munari U., Siviero A., Sostero G., et al., 2007, Baltic Astron., 16, 46.

[92] Mürset U., & Schmid H. M., 1999, A&AS, 137, 473.

[93] Nakamo S., Itagaki K., Denisenko D. et al., 2013, Central Bureau for Astronomical Telegrams (CBET), 3628, edited by Green D. W. E.

[94] Narumi H., Hirosawa K., Kanai K., Renz W., Pereira A., Nakano S., Nakamura Y., Pojmanski G., 2006, IAUC 8671.

[95] Nelson T., Orio M., Cassinelli J. P., et al., 2008, ApJ 673, 1079.

[96] Ness J. U., Starrfield S., Burwitz V. et al., 2003, ApJ, 594, L127.

[97] Ness J. U., Osborne J. P., Dobrotka A. et al., 2011, ApJ, 733, 70.

[98] Ninan J. P., Ojha D. K., Ghosh S. K., et al., 2014, JAI, 03, no. 3 & 4, 1450006.

[99] O' Brien T. J., Bode M. F., & Kahn F. D., 1992, MNRAS, 255, 683.

[100] O' Brien T. J., Bode M. F., & Porcas R. W. et al., 2006, Nature, 442, 279.

[101] Osborne J. P., Page K. L., Beardmore A. P. et al., 2011, ApJ, 727, 124.

[102] Paczynski B., 1977, ApJ, 216, 822.

[103] Payne-Gaposchkin C., 1957, The Galactic Novae, Amsterdam: North-Holland.

[104] Pfau W., 1976, A&A, 50, 113.

[105] Prabhu T. P., 2014, *review article* - Proc Indian Natn Sci Acad, 80, 887.

[106] Prialnik D. & Kovetz A., 1995, ApJ, 445, 789P.

[107] Ribeiro V. A. R. M., Bode M. F., Darnley M. J., et al., 2009, ApJ, 703, 1955.

[108] Riedel A. R., Beaulieu T., Henry T. J., Jao W., Gray R. O., Corbally C. J., & Finch C., 2007, BAAS, 39, 922.

[109] Rosino L., 1987, In: Bode M. F. (Ed.), RS Ophiuchi (1985) and The Recurrent Nova Phenomenon. VNU Science Press, Utrecht, p. 27.

[110] Rupen M. P., Mioduszewski A. J., & Sokolowski J. L., 2008, ApJ, 688, 559.

[111] Sabbadin F. & Bianchini A., 1983, A&AS, 54, 39.

[112] Schaefer B. E., 2010, ApJS, 187, 275.

[113] Schaefer B. E., Harris B. G., Dvorak S., Templeton M., & Linnolt M., 2010, IAU Circ, 9111, 1.

[114] Schmid H. M., 1989, A&A, 211, L31.

[115] Schwarz G. J., Starrfield S., Shore S. N., & Hauschildt P. H., 1997, MNRAS, 290, 75.

[116] Schwarz G. J., Shore S. N., Starrfield S., et al., 2001, MNRAS, 320, 103.

[117] Schwarz G. J., 2002, ApJ, 577, 940.

[118] Schwarz G. J., Shore S. N., Starrfield S., et al., 2007a, ApJ, 657, 453.

[119] Schwarz G. J., Woodward C. E., Bode M. F., et al., 2007b, ApJ, 134, 516.

[120] Seaquist E. R. & Bode M. F., 2008, in Classical Novae, Second Edition, eds. Bode M. F. & Evans A., Cambridge University Press.

[121] Selvelli P. L., Castella A, & Gilmozzi R., 1992, ApJ, 393, 289.

[122] Shara M. M., Yaron O., Prialnik D., Kovetz A. & Zurek D., 2010, astro-ph.SR., arXiv:1009.3864v1.

[123] Shore S. N., 2012, BASI, 40, 185.

[124] Skopal A., Pribulla T., Buil C. et al., 2008, In: Evans, A., Bode, M.F., O' Brien, T.J. & Darnley, M.J. (Eds.), RS Ophiuchi (2006) and the Recurrent Nova Phenomenon, Astronomical Society of the Pacific Conference Series, vol. 401, p. 227.

[125] Snijders M. A. J., 1987, AP&SS 130, 243.

[126] Snijders M. A. J., Batt P. T., Roche P. F., et al., 1987, MNRAS, 228, 329.

[127] Snijders M. A. J., 1990, Lect. Notes Phys., 369, 188.

[128] Sokoloski J. L., Luna G. J. M., Mukai K., et al., 2006, Nature 442, 276.

[129] Starrfield S., Sparks W. M., & Truran J. W., 1985, ApJ, 291, 136.

[130] Starrfield S., 1988, in Multi-wavelength Studies in Astrophysics, ed. F. Cordova. Cambridge: Cambridge University Press, p. 159.

[131] Starrfield S., 1989, in Bode M. F. & Evans A., eds, Classical Novae, 2^{nd} Edition, Cambridge University Press, Cambridge, p. 39.

[132] Starrfield S., Shore S. N., Sparks W. M., et al., 1992, ApJ, 391, L71.

[133] Starrfield S., Timmes F. X., Hix W. R., et al., 2004, ApJ, 612, L53.

[134] Starrfield S., Iliadis C., & Hix W. R., 2008, in Bode M. F. & Evans A., eds, Classical Novae, 2^{nd} Edition, Cambridge University Press, Cambridge, p. 77.

[135] Stickland D. J., Penn C. J., Seaton M. J., Snijders M.A. J., & Storey P. J., 1981, MNRAS, 197, 107.

[136] Tanaka J., Nogami D., Fuji M., Ayani K., Kato T., Maehara H., Kiyota S., & Nakajima K., 2011, PASJ, 63, 911.

[137] Taylor A.R., Davis R.J., Porcas R.W., et al., 1989, MNRAS, 237, 81.

[138] Vanlandingham K. M., Schwarz G. J., Shore S. N., et al., 2005, ApJ, 624, 914.

[139] Viotti R., Altamore A., Ferrari-Toniolo M., Friedjung M., Persi P., Rossi C. & Rossi L., 1986, A&A, 159, 16.

[140] Waagen E. O., 2014, AAVSO Alert Notice, 497.

[141] Walker M. F., 1956, ApJ., 123, 68.

[142] Walter F. M., Battisti A., Towers S. E., Bond H. E., & Stringfellow G. S., 2012, PASP, 124, 1057.

[143] Warner B., 1995, Cataclysmic variables, Cambridge University Press.

[144] Wilber A., Neric M., Starrfield S., Wagner R. M., & Woodward C. E., 2015, Astron. Telegram, 7217.

[145] Williams R. E., 1980, ApJ, 235, 939.

[146] Williams R. E., Hey E. P., Sparks W. M., Starrfield S. G., Wyskoff S. & Truran J. W., 1985, MNRAS, 512, 753.

[147] Williams R. E., 1990, in Physics of Classical Novae, ed. A. Cassatella & R. Viotti, Springer, p. 215.

[148] Williams A. S., 1901, MNRAS, 61, 337.

[149] Williams R. E., Hamuy M., Phillips M. M., Heathcote S. R., Wells L., & Navarrete M., 1991, ApJ, 376, 721.

[150] Williams R. E., 1992, AJ, 104, 725.

[151] Williams S. C., Darnley M. J., & Henze M., 2017, MNRAS, 472, 1300.

[152] Wood-vasey W. M. & Sokoloski J. L., 2006, ApJ, 645, L53.

[153] Worters H. L., Eyres S. P. S., Bromage G. E., et al., 2007, MNRAS, 379, 1557.

[154] Yamaoka H., Itagaki K., Guido E., et al. 2009, IAU Circ., 9098 # 1.

[155] Yaron O., Prialnik D., Shara M. M., & Kovetz A., 2005, ApJ, 623, 398.